TOHOKU UNIVERSITY
Graduate School of Engineering

Study of Numerical Methods toward Realization of Reliable Aerothermodynamic Prediction in High Enthalpy Shock Tunnel

(高エンタルピ衝撃風洞における高信頼性空気熱力学予測実現に向けた数値計算手法の研究)

A dissertation submitted for the degree of Doctor of Philosophy
(Engineering)

Department of Aerospace Engineering

BY
Tomoaki ISHIHARA

JANUARY 12, 2016

Study of Numerical Methods toward Realization of Reliable Aerothermodynamic Prediction in High Enthalpy Shock Tunnel

Tomoaki Ishihara

Abstract

Recently observed discrepancies between CFD and measured data at high enthalpy conditions in high enthalpy shock tunnel HIEST are numerically examined toward realization of reliable aerothermodynamic prediction of space vehicles in this dissertation.

When a space vehicle enters into the planetary atmosphere, strong detached shock wave is formed around the vehicle. The flow temperature behind the detached shock wave becomes so high that the real gas effects such as vibrational excitation, dissociation, or ionization become significant. Accurate simulation such real gas effects using measured data and CFD is very important for reliable aerothermodynamic predictions. The HIEST is the only facility which can generate the higher enthalpy flows corresponding to entry flight conditions. Many improvements so far have been achieved to conduct reliable measurements at high enthalpy conditions in HIEST, and the obtained data are valuable for research and development of various hypersonic vehicles. However, several discrepancies have been observed in the comparison between HIEST data and CFD. In this study, the cause of such discrepancies between the measured data and those calculated results are critically examined, and some correction methods, where possible, are proposed toward realization of further reliable aerothermodynamic prediction using HIEST at high enthalpy conditions.

First unexpected heat flux augmentations over blunt bodies at higher enthalpy conditions and the scaling effect of those augmentations in HIEST are examined. We focused on the effect on turbulence and two radiative heatings. A three-dimensional thermochemical non-equilibrium CFD code including radiation transport calculation in the shock layer is developed to consider the following effects: Radiative heating from high temperature air species in the shock layer and Radiative heating from impurities such as carbon soot and metal particulates believed to be involved in the upstream test gas. Test calculations are performed at the stagnation enthalpy and the stagnation pressure from 7 to 21 MJ/kg and 31 to 55 MPa, respectively. It is confirmed that radiative heat flux from impurities evaluated at the averaged shock layer temperature with an emissivity coefficient is found to reproduce the measured heat flux augmentation fairy well. An emissivity coefficient of is proposed for the correction of surface heat flux over wind tunnel models placed in the test section of HIEST. The scaling effect can be also explained by the radiation from impurities.

Next, a cause of an overestimation of the computed surface pressure over blunted cone in high enthalpy conditions is explored. The sensitivity analysis reveals that a reduction of the upstream translational temperature in the range of 100 to 300 K substantially improves the agreement of the surface pressure with the measured data. As a possible cause of the lower upstream translational temperature, radiative cooling effect is included in the thermochemical nonequilibrium calculation in the nozzle. It is found that the translational temperature at the nozzle exit is reduced about 250 K for the computed case. Using the obtained flow variables as the upstream boundary condition, the computed surface pressure agrees quite well with the experimental data. In order to clarify whether other variables such as translational-vibrational relaxation time, chemical reaction rates, and upstream chemical composition could be the cause of the discrepancy, sensitivity analysis is conducted using method of uncertainty quantification. It is shown that all of these modeling parameters have minor effect on the agreement of surface pressure. It is concluded that the observed discrepancy of the surface pressure is due to radiative cooling effect of high temperature gas in the nozzle region, which is not accounted for in the characterization of upstream flow conditions of HIEST.

Finally, the discrepancy of heat flux on back shell of the HTV-R capsule with diamond roughness between computation and experiment is examined by using a higher order accurate finite volume scheme. For space capsules that enter into the Earth atmosphere from the low-earth orbit, the convective heat flux becomes dominant which can be critically enhanced if the boundary layer becomes turbulent. It is therefore very important to estimate the convective heat flux in the fully turbulent boundary layer for a safe design of TPS. For this reason, aeroheating measurements with roughness on the back shell of a test model for HTV-R manned space capsule are performed in HIEST. It was found that the measured heat flux on the back shell became larger than those by RANS, which was expected to reproduce fully turbulent heat flux in attached flow. In order to identify the possible cause of this discrepancy, a higher order CFD code which could account for unsteady turbulent flow motion in hypersonic flow was developed. The time averaged heat flux behind the roughness agreed fairy well with the experimental data. It was found that the heating mechanism behind the roughness is due, not to turbulence but to the counter-rotating vortex tube.

In this study, we revealed the causes of recently observed discrepancy between CFD and experiments. Following knowledge was obtained. (1) To predict accurate heat flux on heat-shield in high enthalpy conditions of HIEST, the heat flux should be corrected by $0.132\sigma T_{v\mathrm{ave}}^4$ for large test model. (2) It is recommended to account for radiative cooling effect in computing the freestream condition of HIEST at high enthalpy conditions in order to predict the accurate aerodynamic characteristics. (3) The aerothermal measurements on back shell with the diamond roughness might be not enough accurate to predict fully turbulent heat flux. For safe design of TPS on back shell, more improved roughness which can generate more unsteady flow is needed. These knowledge can lead reliable aerothermodynamic predictions in high enthalpy conditions.

Contents

List of Tables

List of Figures

Chapter 1

Introduction

1.1 Background

When a space vehicle enters into the planetary atmosphere, the strong detached shock wave is formed around the vehicle. The flow temperature behind a detached shock wave becomes so high that the real gas effects such as vibrational excitation, dissociation, or ionization become remarkably. Accurately simulating such real gas effects is very important for designs of space vehicles. For example, real gas effects have significant effect on the pitching moment of Space Shuttles. In the first entry flight of the Space Shuttle, an unexpected pitching moment was observed. The pitching moment in the flight was higher than predicted and body-flap deflection angle for pitch trim was set at the vicinity of the maximum value[1, 2]. It was because that aerodynamic characteristics of space shuttles in preflight were determined experimentally using hypersonic wind tunnels [3]. Figure 1.1 shows the mach number and Reynolds number regime of the flight with those tested in wind tunnels. One can find that wind tunnels cannot cover the regime in higher Mach number conditions. The wind tunnels produced a perfect gas with a γ of either 1.4 (air or nitrogen) or 1.66 (helium)[4]. These flows were cold and temperatures did not exceed about 1200 K in most cases. Therefore, the real gas effects did not simulate in these tests. After the flight, computational fluid dynamics (CFD) on simple shuttle shapes was conducted to clarify the cause of the unexpected pitching moment [1, 2]. Figure 1.2 shows the effect of

the several mechanisms on the pitching moment coefficient. In the reference [2], the three effects: the Mach number effect, chemical effect and the viscous effect on the pitching moment were compared. The study concluded that the major portion of the pitching moment was due to the chemical phenomena since chemical reactions at high temperature cause an increase in density and the increase in density causes the thickness and angles of the shock layer around a vehicle. In higher enthalpy conditions, such integrated research between the flight test and CFD which is powerful tool to clarify the flowfield is important to conduct accurate aerothermodynamic predictions. However, the flight test is very high cost and many conditions cannot be tried. The integrated research between CFD and ground tests is needed.

As a facility of ground test which can generate high enthalpy flow comparable to flight conditions, free-piston shock tunnels have been developed. In order to reproduce the real flight conditions, it is necessary to match enthalpy and binary scaling parameter ($\rho \times L$) with the flight conditions. Experimental test models in the ground tests are smaller than real flight vehicles and stagnation pressure must be larger. However, the stagnation pressure exceeds the design limit of hypersonic wind tunnels. In order to overcome such issue, Stalker[5] proposed a concept of the free-piston shock tunnel in the early 1960s. Figure 1.3 shows the operating principle in a free-piston shock tunnel. First, high pressure gas flows into the compression tube and piston moves to the first diaphragm. When the pressure between the piston and the first diaphragm reaches the rupturing pressure, strong shock moves in the shock tube. Shock reflects at the end of shock tube and high pressure and temperature gas are generated. Then, flow expands by the nozzle and high enthalpy gas flows into the test section. Stalker developed such free-piston shock tunnels named T3 and T4[6] in the University of Queensland in the late 1980. Hornung [7] in Caltech developed T5 which is larger than T3 and T4 in the early 1990. Deutsches zentrum für Luft- und Raumfahrt (DLR) also developed High Enthalpy shock tunnel Göttingen (HEG)[8] in 1990s.

Also in Japan, high enthalpy shock tunnel (HIEST) which is a free piston shock tunnel was developed at the JAXA Kakuda space center in 1990s[9]. Figure 1.4 shows

the overview and specifications of HIEST[10]. HIEST was developed to obtain the aerothermodynamic data of HOPE-X. The HOPE-X was an reusable launch vehicle planned by National Aerospace Laboratory of Japan (NAL) and National Space Development Agency of Japan (NASDA). Due to demands of high reliable aerothermodynamic predictions in high enthalpy conditions for payload capacity, many improvements have been achieved to generate higher enthalpy conditions in HIEST[11, 12]. The tuned operation method for the piston motion in HIEST was proposed by Ito et al.[13]. It was known that the reduction of pressure was observed due to outflow of the driver gas from rupturing of the first diaphragm, which indicated the insufficient generation of the test flow. In the tuned operation method, the first diaphragm ruptures while a piston is moving. It significantly suppresses the reduction of pressure. Moreover, the ratio between the length and diameter of shock tube was also optimized by Itoh et al.[11] . The boundary layer develops behind the shock in the shock tube. This causes the decrease of the shock speed, which indicates the decrease of the enthalpy. In order to remedy such decrease of shock speed, the optimized shape and material of the nozzle throat were also explored by Itoh et al.[12]. Since the higher temperature and pressure test gas flow through the nozzle throat over relatively long time in HIEST, an alloy which has high melting point and high strength was needed. A Cr-Zr-Cu alloy was employed in HIEST. However, the melting of the nozzle throat was unpreventable. This caused the strong perturbation of the test flow. Itoh et al. clarified the mechanism of the perturbation of test flow and suppressed the perturbation by exploring the shape of nozzle throat. Due to such improvements, HIEST has been able to generate high enthalpy flow comparable with the flight conditions. Table 1.1 shows the comparison of specification of shock tunnels. One can find that HIEST is the largest shock tunnels and can generate the highest conditions. Therefore, the integrated reserach in higher enthalpy conditions using the HIEST data and CFD is very useful for reliable aerothermodynamic predictions.

1.2 Previous Researches and Description of Problems

Due to these improvements, HIEST has been utilized for the various kinds of investigations in higher enthalpy conditions such as aerodynamic measurement[14], boundary layer transition[15] and catalytic recombination[16]. Also the flow evaluation has been done experimentally[17] and numerically[18, 19]. However, the three following discrepancies have been recently observed at relatively higher enthalpy conditions.

1.2.1 Abnormal heat flux augmentation on blunt bodies

For development of hypersonic re-entry vehicles, thermal protection from severe aerodynamic heating during the re-entry flight is the most critical issues. For the safe design of thermal protection system (TPS), accurate prediction of heat flux especially on heat-shield of space vehicles is important.

However, unexpected heat flux augmentations on heat-shield of blunt bodies at higher enthalpy conditions in HIEST were recently observed. Figure. 1.5 shows measured heat flux data along the centerline of the Apollo command module (CM) 6.4% scale model measured in HIEST [10] with the convective heat flux profile given by a thermochemical non-equilibrium CFD code. [20]. When the heat flux data are scaled by $St \times \sqrt{Re_{\infty,D}}$ where St and $Re_{\infty,D}$ are the Stanton number and the Reynolds number based on the typical model dimension, respectively. It is known that the convective heat flux should fall on a single curve. Although the computed convective heat flux profiles fall on a single curve reasonably well, the experimental data obtained in HIEST show higher heat flux values. Moreover, one can find that the difference between the measured heat flux and the corresponding heat flux given by CFD becomes larger as the stagnation enthalpy of the test flow becomes higher. In addition, other aerodynamic heating measurements on the probes which had small radius were carried out in HIEST [21]. Figure 1.6 shows the ratio between the measured heat flux q_{exp} and the computed convective heat flux $q_{\mathrm{calc.conv.}}$ of three test models. The

Apollo test model has the largest radius of 300 mm. Probe A and B have the radius of 100 mm and 10 mm, respectively. One can find that the abnormal heat flux augmentations are insignificant for small radius probes at the same stagnation enthalpy for which the higher abnormal heat flux augmentation appears for the Apollo CM test model.

Such abnormal heat flux augmentation seems to be observed commonly in other high enthalpy shock tunnels [22–27]. The effect of augmentation caused by the turbulence and surface catalysis was examined. By assuming fully turbulent flow or the super catalytic wall, calculated convective heat flux can reach the experimental values. However, the distribution could not be reproduced. The cause of such higher heat flux has not been clearly determined yet. In the HIEST experiments, the abnormal heat flux augmentation is larger than the one in other facilities since the larger radius test model can be used and the abnormal heat flux become significant for the larger radius model as discussed above. Therefore, the data in the HIEST experiments are useful for examining abnormal heat flux augmentation.

1.2.2 Overestimation of computed surface pressure on blunt nosed cone

For accurate prediction of aerodynamic characteristics of hypersonic re-entry vehicles, the high enthalpy flow over the vehicles are should be examined. For the capsules such as the Apollo CM, the major region which determines the aerodynamic characteristics of the vehicles is the stagnation region in front of the heat-shield. In these high compressive region, many research has investigated and the accurate aerodynamic prediction has conducted[3]. On the other hand, the flow over the blunt nosed cone such as lifting body and winged body becomes complicated. Flow undergoes the stagnation region over the nose, the supersonic expanding region near the shoulder and the weak compressed region over the cone is formed. In order to accurately predict the aerodynamic characteristics, these complicated flow should be examined.

The wall pressure distributions over a blunt nosed cone were measured in

HIEST[28–30]. Figure 1.7 shows a schematic illustration of the test model. The test model was 15-deg sphere-cone model with a nose radius of 50 mm. Four different stagnation enthalpies ($H_0 = 3.8, 8.0, 10.1$ and 15.6 MJ/kg) were chosen. Figure 1.7 also shows the measured pressure distributions in the conical region of the test model with the results computed by the thermochemical non-equilibrium CFD at $H_0 = 15.6$ MJ/kg. One can find that the calculated pressure values are higher than those experimental results. In previous work, the flowfield calculation over the test models using chemical reaction rates by Park[31] and Dunn and Kang[32] were conducted, and the surface wall pressure has been explored[30]. However, the effect of such models on the surface pressure was small. Moreover, flow variables at the nozzle exit of HIEST which are used as the upstream conditions for calculating flowfield over the test models have been examined. Takahashi et al.[19] calculated the flowfield in the nozzle using several thermochemical model such as Park's two temperature model[3] and a four temperature model[19], for which the conservation of the vibrational-electronic excitation energy for N_2, O_2 and NO is calculated individually. Any temperature model could not explain the overestimation of computed surface pressure. The cause of this discrepancy remains to be explained.

1.2.3 Heat flux on back shell of a blunt body with a diamond roughness

When space vehicles that enter into the Earth atmosphere from the low-earth orbit, the convective heat flux becomes dominant which can be critically enhanced if the boundary layer becomes turbulent[33]. Since the laminar-turbulent boundary layer transition will occur by complicated processes such as effects of ablation blowing, laminar-ablated surface roughness and flow chemistry. The mechanism of the transition remains not to be explained[34]. However, TPS design community has taken a conservative approach and designed the heat-shield on the assumption that fully turbulent flow. For a lower velocity return from the ISS, significant ablation is not expected, and boundary layer transition is likely to be induced by distributed

isolated roughness associated with heat-shield step and gap tolerances or surface irregularities[35]. It is very important to estimate the fully turbulent heat flux by the roughness induced transition for the TPS designs.

The measurements of aerothermal heating on heat-shield of capsules with roughness induced transition have been conducted in hypersonic wind tunnels[35, 36] and shock tunnels[37]. Amar et al. measured heat flux on the Orion CEV in the NASA Langley Research Center 20-In Mach 6 Air Tunnel, and compared with the computed heat flux using the Data-Parallel Line Relaxation (DPLR) finite-volume CFD code[38] with Baldwin-Lomax turbulence model[39] assuming fully turbulent flow. The computed heat flux became comparable to the experimental data when flow became fully turbulence. Similar results by the Langley Aerothermodynamic Upwind Relaxation Algorithm (LAURA)[40, 41] with Cebeci-Smith[42] by Berger et al. were found[36]. Algebraic models, such as Baldwin-Lomax and Cebeci-Smith have shown good agreement with perfect-gas experiments for the attached heat-shield of space capsules such as CEV[43]. The measurements of heat flux on 7-inch Apollo-shaped capsule by roughness induced transition in higher enthalpy conditions were conducted in the T5 shock tunnel at GALCIT for stagnation enthalpies between 7 and 20 [MJ/kg] by Eric et al[37]. Reasonable agreement was seen between the turbulent non-equilibrium computations with DPLR and the experimental results in higher enthalpy conditions. Therefore, the fully turbulent heat flux on the heat-shield is enough by RANS for the safe design of TPS.

In the HIEST, the aeroheating measurements on the back shell of the HTV-R test model have conducted[44, 45]. HTV-R is a manned space capsule for returning astronauts from the ISS[46] under consideration in Japan. The measured heat flux data on the center line of the heat-shield surface are shown in Fig. 1.8 with the computed results by RANS. The seven elements of diamond roughness were mounted on the back shell as shown in Fig. 1.8. Diamond roughness has been empirically used for the roughness induced transition. The freestream total enthalpy of $H_0 = 3.6$ [MJ/kg] and the Reynolds number of $Re_\infty = 5.11 \times 10^6$ [1/m]. The angle of

attack is 28 [deg]. One can find that the heat flux became 2−4 times higher behind the roughness. However, RANS underestimates the measured heat flux even though RANS is expected to reproduce attached flow and the heat flux on the heat-shield could obtain good agreement as above discussed. The cause of the discrepancy has not been explained yet. For the safe design of TPS, it is important to accurately predict the heat flux in fully turbulent flow. It is well unknown whether flow becomes fully turbulent on back shell or not, although HIEST can generate relatively higher Reynolds number flow at higher enthalpy conditions in shock tunnels. In order to examine the flowfield around a roughness, higher order code in hypersonic flow is needed.

1.3 Objectives and Outline of the Present Study

In this study, the above discussed discrepancies between HIEST data and CFD were explored.

1. Abnormal heat flux augmentation of blunt bodies
2. Overestimation of computed surface pressure over blunt nosed cone
3. Discrepancy of heat flux on back shell of a blunt body with a diamond roughness between RANS and measured data

Our objective of this study is to critically examine the cause of discrepancies, and explore some correction methods, where possible, toward realization of reliable aerothermodynamic prediction using HIEST at high enthalpy conditions. The content consists of five chapters as below. Chapter 1 is the present introduction.

In Chapter 2, the cause of the abnormal heat flux augmentation over blunt bodies at higher enthalpy conditions in HIEST is examined. We focused on the effect of radiative heating. A three-dimensional thermochemical non-equilibrium CFD code including radiation transport calculation in the shock layer is developed to consider the following effects: 1) Radiative heating from high temperature air species in the

shock layer and 2) Radiative heating from impurities such as carbon soot and metal particulates believed to be involved in the upstream test gas. In addition, an engineering technique is examined for the correction of abnormal heat flux augmentation.

In Chapter 3, the cause of the overestimation of the computed surface pressure over blunted cone in high enthalpy condition is explored. We first focus on nominal upstream conditions which have been determined by the JAXA in-house code. CFD calculations in the test section employ the flow conditions as the upstream boundary conditions. This JAXA in-house nozzle code has been used for wide range of operating conditions and is believed to yield reliable upstream conditions. However, validation of the nozzle code for all the operating conditions is difficult to be accomplished because of lack of experimental data. In this study, therefore, we attempt to vary the upstream flow conditions to find which flow variable has a high sensitivity on the computed surface pressure distribution over the blunt test model. Second, we focus on to examine the relaxation time between translational and vibrational modes, and also the chemical reaction rates in the supersonic expanding region employed in the CFD code. In the present CFD calculation, we choose the Park's two-temperature nonequilibrium thermochemical model.[3, 31] This model employs the Arrhenius form to describe forward chemical reaction rates and the Millikan-White translational-vibrational relaxation time.[47] The parameters of these models were calibrated using the experimental data obtained behind normal shocks in shock tube where strong compression occurs. We examine the effect of such parameters of the thermochemical nonequilibrium models in the supersonic expanding region.

In Chapter 4, we first developed the high order code for the hypersonic flow in order to identify the cause of the discrepancy between the measured heat flux and RANS. Then we calculate the flowfield around a roughness on the back shell of HTV-R and examine the flowfield using our developed code. Computed time averaged heat flux behind the roughness is compared with the measured data.

Lastly, Chapter 5 concludes the present study by summarizing the contents in the previous chapters.

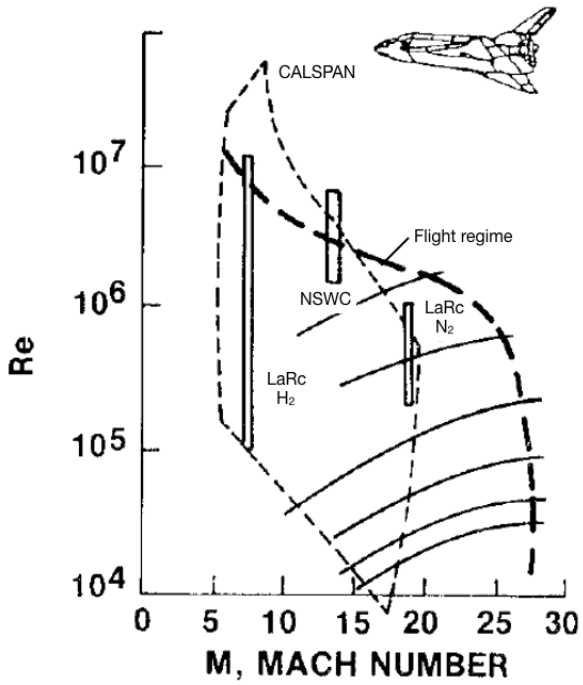

Fig. 1.1 Mach number and Reynolds number regime of the first flight of Space Shuttle with those preflight tested in wind tunnels. [2]

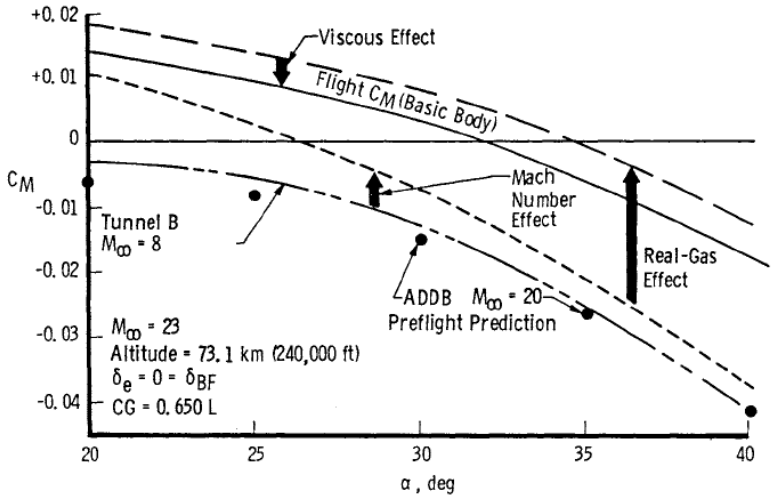

Fig. 1.2 Effects of viscous, Mach and real-gas on pitching moment coefficient.[2]

Table. 1.1 Comparison of free piston shock tunnels

Facility	Compression tube		Shock tube		$H_{0\max}$	$P_{0\max}$
	D [mm]	L [mm]	D [mm]	L [mm]	[MJ/kg]	[MPa]
JAXA HIEST[9]	600	4200	180	1700	25	150
DLR HEG[8]	550	3300	150	1700	23	100
Caltech T5[7]	300	3000	90	1200	15	90
Queesnland T4[6]	229	2600	76	1000	20	90

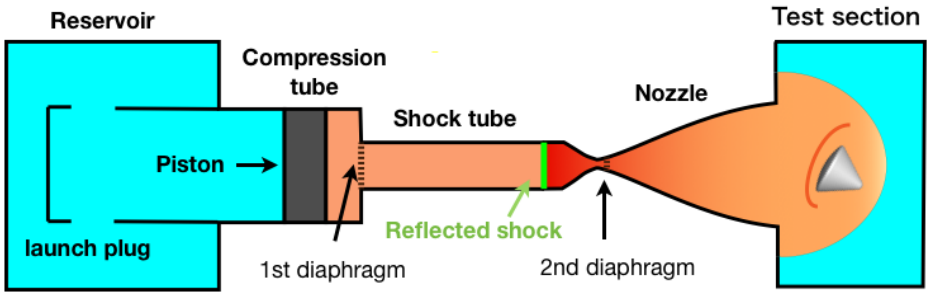

Fig. 1.3 Schematic of operating principle in a free-piston shock tunnel.

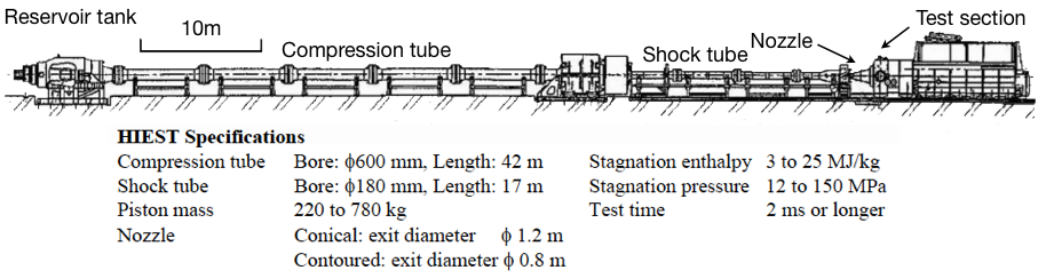

Fig. 1.4 High enthalpy shock tunnel HIEST [10].

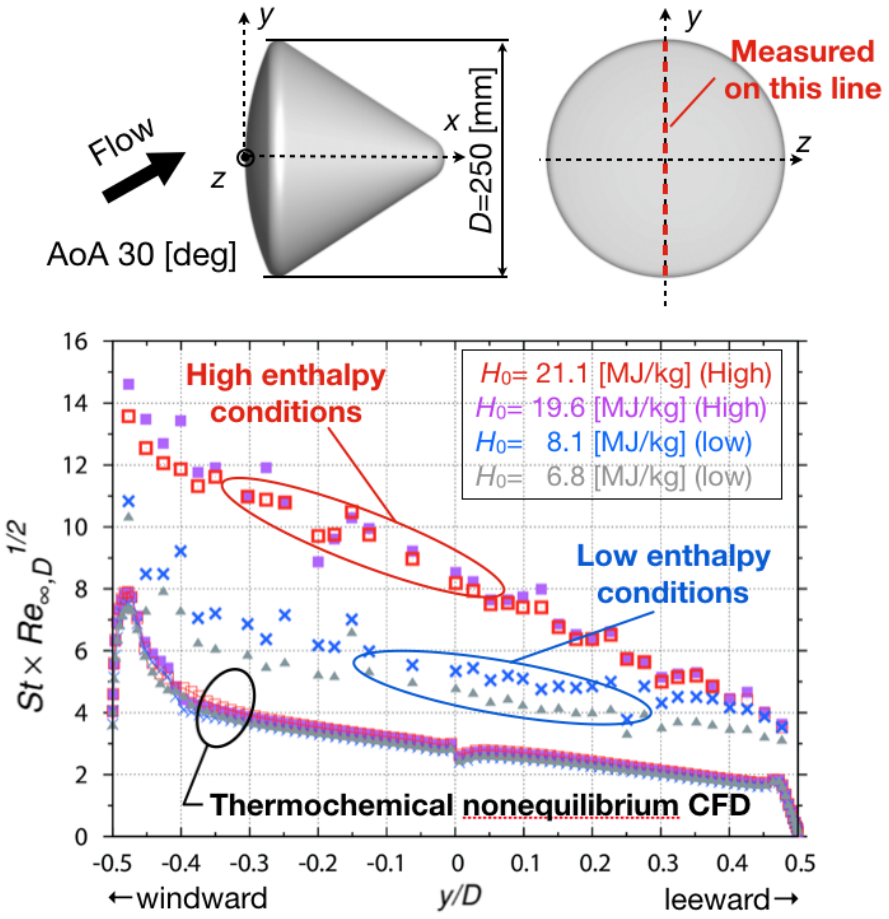

Fig. 1.5 Abnormal heat flux augmentation on heat-shield of 6.4% scaled Apollo CM test model in HIEST.

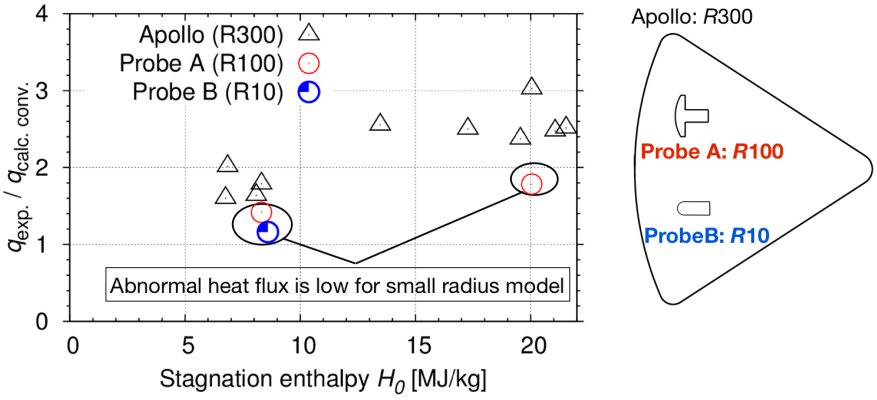

Fig. 1.6 Scaling effect of abnormal heat flux augmentation in HIEST.

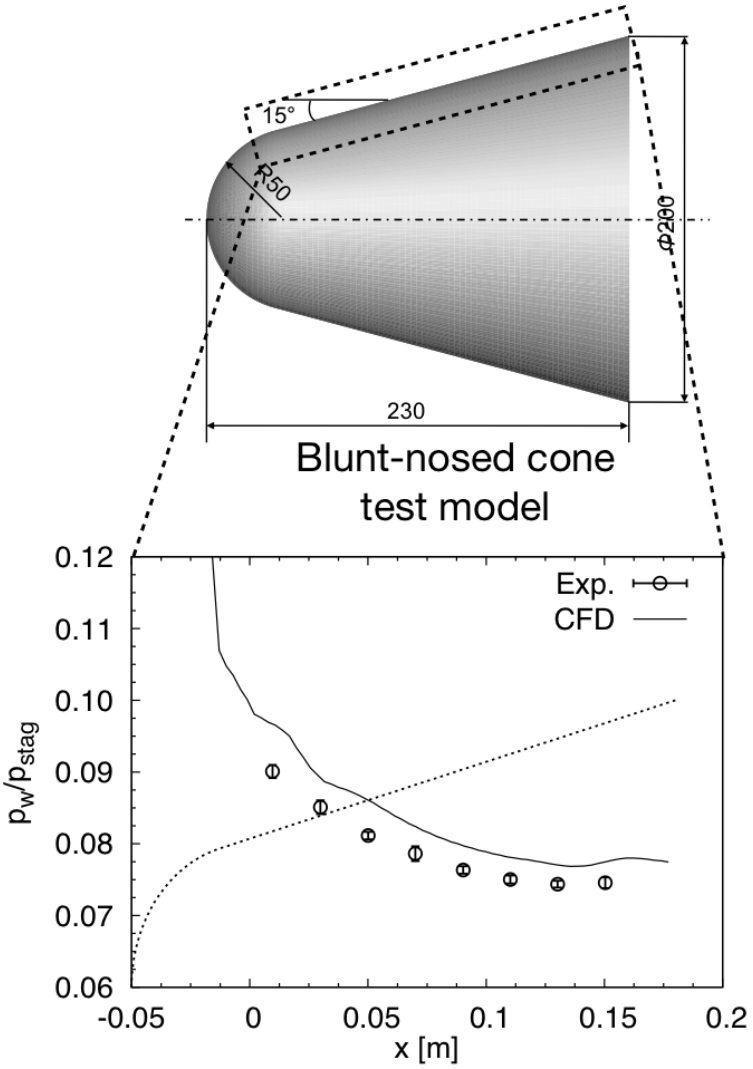

Fig. 1.7 Overestimation of computed surface pressure on conical region of blunt nosed cone test model in HIEST.

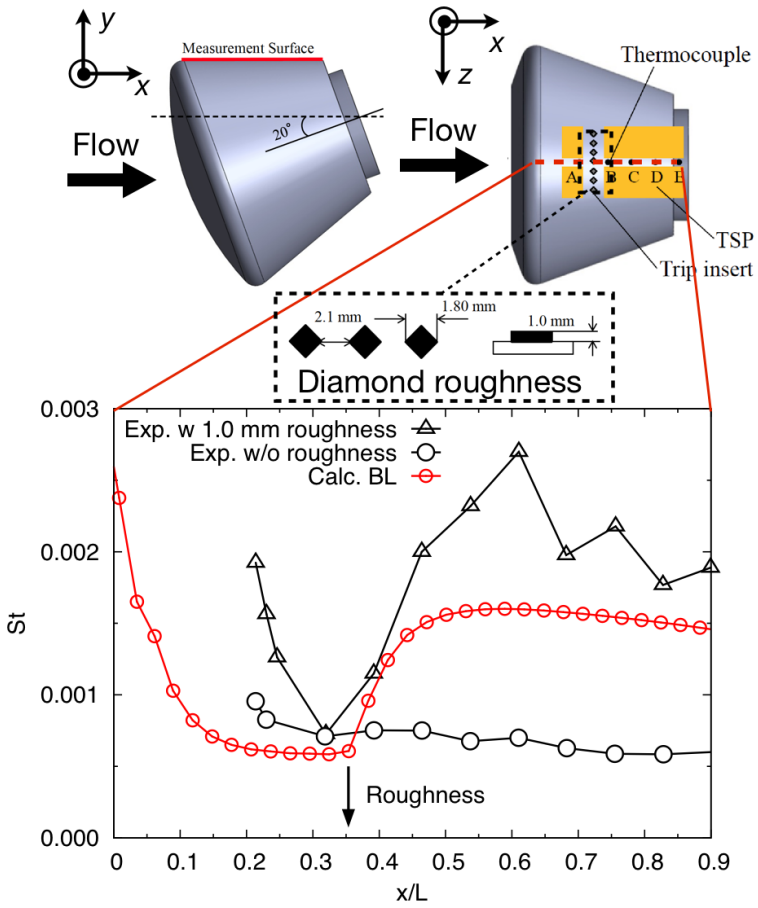

Fig. 1.8 Heat flux on back shell of HTV-R test model with a diamond roughness: upper figure which indicates the position of diamond roughness and TSP is referred to Ref. [44].

Bibliography

[1] Woods, W. C., Arrington, J. P., and Hamilton, H. H., "A Review of Preflight Estimates of Real-Gas Effects on Space Shuttle Aerodynamic Characteristics," Shuttle Performace: Lessons Learned, Part 1 in NASA CP-2283, pp. 309-346, NASA, 1983.

[2] Griffith, B. J., Maus, J. R., and Best, J. T., "Explanation of the Hypersonic Longitudinal Stability Problem- Lessons Learned," Shuttle Performace: Lessons Learned, Part 1 in NASA CP-2283, pp. 347-381, NASA, 1983.

[3] Park, C., *Nonequilibrium Hypersonic Aerothermodynaics*, John Wiley and Sons, Inc., 1989.

[4] Rockwell international, "Aerodynamic Design Data Book vol 1 orbiter vehicle," Technical Paper SD72-SH-0060, Rockwell international, 1980.

[5] Stalker R. J., "A Study of the Free-Piston Shock Tunnel," *AIAA Journal*, Vol. 5, No. 12, 1967, pp. 2160–2165.

[6] Paull, A. and Stalker R. J., "Scramjet Testing in the T3 and T4 Hypersonic Impulse Facilities," *Progress in Astonautics and Aeronautics*, Vol. 189, 2000, pp. 1–43.

[7] Hornung H. G., "Performance data of the New Free-Piston Shock Tunnel at GALCIT," AIAA Paper 92-3943, 1992.

[8] Eitelberg, G., "First results of calibration and use of the HEG," AIAA Paper 1994-2525, 1994.

[9] Itoh, K., Ueda, S., Tanno, H., Komuro, T., and Sato, K., "Hypersonic Aerother-

modynamic and Scramjet Research Using High Enthalpy Shock Tunnel," *Shock Waves*, Vol. 12, 2002, pp. 93–98.

[10] Tanno, H., Kodera, M., Komuro, T., Sato, K., Takahashi, M., and Itoh, K., "Aeroheating Measurements on a Reentry Capsule Model in Free-Piston Shock Tunnel HIEST," AIAA paper 2010-1181, 2010.

[11] 伊藤 勝宏, 植田 修一, 小室 智幸, 佐藤 和雄, 宮島 博, 河内山 治朗, 古賀 寛哉, 野本 秀喜, 戸上 健治, 村本 一, "大型衝撃風洞 HIEST の開発 -その 1 風洞の設計と作動特性-," **日本航空宇宙学会誌**, Vol. 49, 2001, pp. 199–207.

[12] 伊藤 勝宏, 植田 修一, 小室 智幸, 佐藤 和雄, 丹野英幸, 高橋政浩, "大型衝撃風洞 HIEST の開発 -その 2 気流特性-," **日本航空宇宙学会誌**, Vol. 50, 2001, pp. 1–6.

[13] Itoh, K., Ueda, S., Komuro, T., Sato, K., Takahashi, M., Miyajima, H., Tanno, H., and Muramoto, H., "Improvement of Free Piston Driver for High Enthalpy Shock Tunnel," *Shock Waves*, Vol. 8, 1998, pp. 215–223.

[14] Tanno, H., Komuro, T., Sato, K., Fujita, K., and Laurence, J. S., "Free-flight measurement technique in the free-piston high-enthaly shock tunnel," *Review of Scientific Instruments*, Vol. 85, 2014, pp. 1–8.

[15] Tanno, H., Komuro, T., Sato, K., Itoh, K., Takahashi, M., and Fujii, K., "Measurement of hypersonic boundary layer transition on cone models in the free-piston shock tunnel HIEST," AIAA Paper 2009-781, 2009.

[16] Ueda, S., Sato, K., Komuro, T., Tanno, H., Itoh, K., Kurotaki, T., and Ito, T., "Numerical Analysis of Experimental Results on the Surface Catalycity in HIEST," AIAA Paper 2005-3281, 2005.

[17] Tanno, H., Komuro, T., Sato, K., and Itoh, K., "Laser Absorption Spectroscopy for Determination of Flow Characteristics in High Enthalpy Shock Tunnel," AIAA Paper 2006-8002, 2006.

[18] Itoh, K., Komuro, T., Tanno, H., Sato, K., Takahashi, M., Kodera, M. and Hashimoto, T., "Flow Characterization of High Enthalpy Shock Tunnel Based on Schock Stand-off Distance," AIAA Paper 2009-7268, 2009.

[19] Takahashi, M., Kodera, M., Itoh, K., Komuro, T., Sato, K., and Tanno, H., "In-

fluence of Thermal Non-equilibrium on Nozzle Flow Condition of High Enthalpy Shock Tunnel HIEST," AIAA Paper 2009-7267, 2009.

[20] Ishihara, T., Ogino, Y., Sawada, K., and Tanno, H., "Computation of Surface Heat Transfer Rate on Apollo CM Test Model in Free-Piston Shock Tunnel HIEST," AIAA paper 2012-0285, 2012.

[21] Tanno, H., Komuro, T., Sato, K., Itoh, K., Yamada, T., Sato, N., and Nakano, E., "Heat Flux Anomaly in High-enthalpy and High Reynolds Number Flow," AIAA Paper 2012-3104, 2012.

[22] Hollis, B. R. and Prabhu, D. K., "Assessment of Laminar, Convective Aeroheating Prediction Uncertainties for Mars Entry Vehicles," AIAA Paper 2011-3144, 2011.

[23] Stewart, D. A. and Chen, Y. K., "Hypersonic Convective Heat Transfer over 140-deg Blunt Cones in Different Gases," *Journal of Spacecraft and Rockets*, Vol. 31, No. 5, 1994, pp. 735–743.

[24] Marineau, C. E., Laurence, S. J., and Hournung, H. G, "Apollo-Shaped Capsule Boundary Layer Transition at High-Enthalpy in T5," AIAA Paper 2010-446, 2010.

[25] Wright, M. J., Olejniczak, J., Brown, J. L., Hornung, H. G., and Edquist, K. T., "Modeling of Shock Tunnel Aeroheating Data on the Mars Science Laboratory Aeroshell," *Journal of Thermophysics and Heat Transfer*, Vol. 20, No. 4, 2006, pp. 641–651.

[26] Olenjniczak, J., Wright, M. J., Laurence, S., and Hornung, H. G., and Edquist, K. T., "Computational Modeling of T5 Laminar and Turbulent Heating Data on Blunt Cones, Part I: Titan Applications," AIAA Paper 2005-0176, 2005.

[27] Hollis, B. R., Liechty, D. S., Wright, M. J., Holden, M. S., Wadhams, T. P., MacLean, M., and Dyakonov, A., "Transition Onset and Turbulent Heating Measurements for the Mars Science Laboratory Entry Vehicle," AIAA Paper 2005-1437, 2005.

[28] Tanno, H., Sato, K., Komuro, T., Itoh, K., and Takahashi, M., "Aerodynamic

Characteristics of Generic Models under Real-gas Condition in the Free-piston Shock Tunnel HIEST," AIAA paper 2008-2567, 2008.

[29] 伊藤 勝宏, 佐藤　和雄, 小室智幸, 高橋政浩, 丹野英幸, "鈍頭物体まわりの高エンタルピ流れについて," 平成２３年度衝撃波シンポジウム講演論文集, 2012, pp. 447–450.

[30] Takahashi, M., Kodera, M., Sato, K., and Itoh, K., "Study on Aerodynamic Characteristics of a High Enthalpy Flow around a Blunt-nosed Body," AIAA paper 2012-5905, 2012.

[31] Park, C., "Review of Chemical-Kinetic Problems of Future NASA Mission, I:Earth Entries," *Journal of Thermophysics and Heat Transfer*, Vol. 7, No. 3, 1993, pp. 385–298.

[32] Dunn, M. G. and Kang, S. W., "Theoretical and Experimental Studies of Reentry Plasmas," NASA CR-2232, 1973.

[33] Tauber, M. E. and Sutton, K., "Stagnation-point radiative heating relations for earth and Mars entries," *Journal of Spacecraft and Rockets*, Vol. 28, No. 1, 1991, pp. 40–42.

[34] Schneider, S. P., "Laminar-Turbulent Transition on Reentry Capsules and Planetary Probes," *Journal of Spacecraft and Rockets*, Vol. 43, No. 6, 2006, pp. 1153–1173.

[35] Amar, A. J., Horvarth T. J., Hollis, B. R., Berger, K. T., and Berry, S. A., "Protuberance boundary layer transition for project Orion crew entry vehicle," AIAA Paper 2008-1227, 2008.

[36] Berger, K., T., "Aerothermodynamic Testing of the Crew Exploration Vehicle in the LaRC 20-Inch Mach 6 and 31-Inch Mach 10 tunnels," AIAA Paper 2008-1225, 2008.

[37] Marineau, E. C., Laurence, S. J., and Hornung, H. G., "Apollo-shaped capsule boundary layer transition at high-enthalpy in T5," AIAA Paper 2010-446, 2010.

[38] Wright, M. J., Candler, G. V., and Bose, D., "Data-Parallel Line Relaxation Method for the Navier-Stokes Equations," *AIAA Journal*, Vol. 36, No. 9, 1998, pp. 1603–1609.

[39] Baldwin, B. S. and Lomax, H., "Thin Layer Approximation and Algebraic Model for Separated Turbulent Flows," AIAA Paper 78-257, 1978.

[40] Gnoffo, P. A., "An Upwind-Biased, Point-Implicit Relaxation Algorithm for Viscous Compressible Perfect Gas Flows," NASA TP 2953, 1990.

[41] Cheatwood, F. M. and Gnoffo, P. A., "User's Manual for the Langley Aerothermodynamic Upwind Relaxation Algorithm (LAURA)," NASA TM 4674, 1996.

[42] Cebeci, T., Bradshaw, P., "Momentum Transfer In Boundary Layers," Hemisphere Publishing Corporation, Washington, D.C., 1997.

[43] Holis, B. R., Berger, K. T., Horvath, T. J., Coblish, J. J., Norris, J. D., Lillard, R., P., and Kirk, B. S., "Aeroheating testing and prediction for project Orion CEV at turbulent condition," AIAA Paper 2008-1226, 2008.

[44] Nagai, H. and Horagir, T., "Visualization of a Re-entry Vehicle in Hypersonic Flow using Temperature -Sensitive Paint," Proceedings of the 16th International Symposium on Flow Visualization, ISFV16-1275, 2014.

[45] 丹野 英幸, 小室 智幸, 佐藤 和雄, 伊藤 勝宏, "高温衝撃風洞 HIEST による HTV-R カプセル形状模型の空力加熱試験," 日本機会学会 2014 年度年次大会, S191024, 2014.

[46] Suzuki, Y. and Imada, T., "Concept and Technology of HTV-R, An Advanced Type of H-II Transfer Vehicle," Proceedings of the 28th ISTS, 2011-g-09, 2011.

[47] Millikan, R. C. and White, D. R., "Systematics of Vibrational Relaxation," *Journal of Chemical Physics*, Vol. 39, No. 12, 1963, pp. 3209–3213.

Chapter 2

Numerical Study of Abnormal Heat Flux Augmentation

2.1 Introduction

Abnormal heat flux augmentation has been observed in HIEST as discussed in Chapter 1. Figure 2.1 show the comparison heat flux on the heat-shield of Apollo CM test model between calculated results and measured data at AoA=0 and 30 deg. The upstream conditions are summarized in Table 2.2. One can find that the measured data is significantly larger than the computed results. In addition aeroheating measurements on a flat plate were conducted with optical filters, which can measure radiation and convective heat flux independently [1] to clarify the cause of the abnormal heat flux. Figure 2.2 shows the time history of pressure and heat flux at the stagnation point on the flat plate (shown in Fig. 7 in Tanno et al. [1]). One can find that the radiative heat flux is delayed compared to the rising time of pressure and total heat flux, which was measured by thermocouples without optical windows. It indicates that the body surface received radiation after developing the shock layer. However, the source of the radiation is yet unknown.

The objective of this study is to clarify the mechanisms of the radiative heating and the scaling effect using the HIEST data where the augmentation is remarkable in free-piston shock tunnels. In addition, we examine an engineering technique to estimate the abnormal heat flux augmentation. We focus on two radiation heatings

in the shock layer: 1) radiation heating from air species, and 2) radiation heating from impurities like soot and metal which can be included in the test gas under the high stagnation temperature condition. First, we calculate the radiative heat flux from air species in the shock layer to show whether or not it can be the source of the enhanced heat flux. Then, we show some evidence that suggests radiation from impurities involved in the test flow can explain the elevated heat flux. However, the chemical species and amount of impurities are unknown. In this study, we assume the impurities as a grey gas. In the following, numerical methods are described in Sec. 2, numerical conditions are shown in Sec. 3, and obtained results and related discussions are given in Sec. 4. The conclusions are finally stated in Sec. 5.

2.2 Numerical Methods

2.2.1 Governing equations of flowfield calculation

The governing equations for the flow field calculation are the three-dimensional Navier-Stokes equations accounting for thermochemical non-equilibrium. We employ Park ' s two-temperature thermochemical model [2].

$$\frac{\partial \boldsymbol{Q}}{\partial t} + \frac{\partial (\boldsymbol{F} - \boldsymbol{F}_{\mathrm{vis}})}{\partial x} + \frac{\partial (\boldsymbol{G} - \boldsymbol{G}_{\mathrm{vis}})}{\partial y} + \frac{\partial (\boldsymbol{H} - \boldsymbol{H}_{\mathrm{vis}})}{\partial z} = \boldsymbol{W}. \tag{2.1}$$

In this study, we assume five neutral air species (O, N, NO N_2 and O_2) for air. Instead of solving all of these species conservation equations, N_2 and O_2 are calculated by total density, the density of O, N and NO, and the conservation of element ratio [2] as follows;

$$\rho_{\mathrm{O}_2} = M_{\mathrm{O}_2}(\alpha_1 \rho + \alpha_2 \rho_{\mathrm{O}} + \alpha_3 \rho_{\mathrm{NO}}), \tag{2.2}$$

$$\rho_{\mathrm{N}_2} = M_{\mathrm{N}_2}(\alpha_4 \rho + \alpha_5 \rho_{\mathrm{N}} + \alpha_6 \rho_{\mathrm{NO}}). \tag{2.3}$$

where α_{1-6} are

$$\alpha_1 = \frac{1}{M_{\mathrm{O}_2} + \frac{M_{\mathrm{N}_2}}{fr}}, \tag{2.4}$$

$$\alpha_2 = -\alpha_1 \left(1 + \frac{1}{2}\frac{M_{\mathrm{N}_2}}{M_{\mathrm{O}}}\right), \tag{2.5}$$

$$\alpha_3 = -\alpha_1 \left(1 + \frac{1}{2fr}\left(\frac{1}{fr} - 1\right)\frac{M_{\mathrm{N}_2}}{M_{\mathrm{NO}}}\right), \tag{2.6}$$

$$\alpha_4 = \frac{1}{M_{\mathrm{N}_2} + M_{\mathrm{O}_2} fr}, \tag{2.7}$$

$$\alpha_5 = -\alpha_4 \left(1 + \frac{fr}{2}\frac{M_{\mathrm{O}_2}}{M_{\mathrm{N}}}\right), \tag{2.8}$$

$$\alpha_6 = -\alpha_4 \left(1 - \frac{1-fr}{2}\frac{M_{\mathrm{O}_2}}{M_{\mathrm{NO}}}\right), \tag{2.9}$$

$$fr = \frac{N_{\mathrm{O}} + 2N_{\mathrm{O}_2} + N_{\mathrm{NO}}}{N_{\mathrm{N}} + 2N_{\mathrm{N}_2} + N_{\mathrm{NO}}}. \tag{2.10}$$

where N_s is the molarity,

$$N_s = \frac{\rho_s}{M_s}. \tag{2.11}$$

Thus, we calculate only three density conservation equations, a total density conservation equation, three momentum conservation equations, a total energy conservation equation and a vibrational-electronic conservation energy equation. Components of the conservative variables $\boldsymbol{Q}$, the convective flux vector $\boldsymbol{F}$, $\boldsymbol{G}$ and $\boldsymbol{H}$, and the viscous vector $\boldsymbol{F}_{\mathrm{vis}}$, $\boldsymbol{G}_{\mathrm{vis}}$ and $\boldsymbol{H}_{\mathrm{vis}}$ are given by respectively as follows:

$$\boldsymbol{Q} = \begin{pmatrix} \rho \\ \rho u \\ \rho v \\ \rho w \\ E \\ \rho_s \\ E_v + E_{el} \end{pmatrix}, \tag{2.12}$$

$$\boldsymbol{F} = \begin{pmatrix} \rho u \\ \rho u^2 + p \\ \rho uv \\ \rho uw \\ (E+p)u \\ \rho_s u \\ (E_v + E_{el})u \end{pmatrix}, \boldsymbol{G} = \begin{pmatrix} \rho v \\ \rho uv \\ \rho v^2 + p \\ \rho vw \\ (E+p)v \\ \rho_s v \\ (E_v + E_{el})v \end{pmatrix}, \boldsymbol{H} = \begin{pmatrix} \rho w \\ \rho wu \\ \rho wv \\ \rho w^2 + p \\ (E+p)w \\ \rho_s w \\ (E_v + E_{el})w \end{pmatrix}, \tag{2.13}$$

$$\boldsymbol{F}_{\text{vis}} = \begin{pmatrix} 0 \\ \tau_{xx} \\ \tau_{xy} \\ \tau_{xz} \\ F_{v,5} \\ -\rho_s u_s \\ F_{v,9} \end{pmatrix}, \boldsymbol{G}_{\text{vis}} = \begin{pmatrix} 0 \\ \tau_{yx} \\ \tau_{yy} \\ \tau_{yz} \\ G_{v,5} \\ -\rho_s v_s \\ G_{v,9} \end{pmatrix}, \boldsymbol{H}_{\text{vis}} = \begin{pmatrix} 0 \\ \tau_{zx} \\ \tau_{zy} \\ \tau_{zz} \\ H_{v,5} \\ -\rho_s w_s \\ H_{v,9} \end{pmatrix}, \tag{2.14}$$

$$\boldsymbol{W} = \begin{pmatrix} 0 \\ 0 \\ 0 \\ 0 \\ 0 \\ \dot{W}_s \\ \dot{W}_v \end{pmatrix}, \tag{2.15}$$

$$F_{v,5} = u\tau_{xx} + v\tau_{xy} + w\tau_{xz} - q_{tx} - q_{vx} - \sum_s \rho_s u_s h_s, \tag{2.16}$$

$$G_{v,5} = u\tau_{yx} + v\tau_{yy} + w\tau_{yz} - q_{ty} - q_{vy} - \sum_s \rho_s v_s h_s, \tag{2.17}$$

$$H_{v,5} = u\tau_{zx} + v\tau_{zy} + w\tau_{zz} - q_{tz} - q_{vz} - \sum_s \rho_s w_s h_s. \tag{2.18}$$

$$F_{v,9} = -q_{vx} - \sum_s \rho_s u_s (e_{vs} + e_{els}), \tag{2.19}$$

$$G_{v,9} = -q_{vy} - \sum_s \rho_s v_s (e_{vs} + e_{els}), \tag{2.20}$$

$$H_{v,9} = -q_{vz} - \sum_s \rho_s w_s (e_{vs} + e_{els}). \tag{2.21}$$

The shear stresses are assumed to be proportional to the first derivative of the mass averaged velocities and the Stokes assumption for the bulk viscosity is made. The

shear stress tensor τ_{ij} is written as,

$$\begin{pmatrix} \tau_{xx} & \tau_{xy} & \tau_{xz} \\ \tau_{yx} & \tau_{yy} & \tau_{yz} \\ \tau_{zx} & \tau_{zy} & \tau_{zz} \end{pmatrix} = \begin{pmatrix} \frac{2}{3}\mu(2\frac{\partial u}{\partial x} - \frac{\partial v}{\partial y} - \frac{\partial w}{\partial z}) & \mu(\frac{\partial u}{\partial y} + \frac{\partial v}{\partial x}) & \mu(\frac{\partial u}{\partial z} + \frac{\partial w}{\partial x}) \\ \mu(\frac{\partial v}{\partial x} + \frac{\partial u}{\partial y}) & \frac{2}{3}\mu(2\frac{\partial v}{\partial y} - \frac{\partial w}{\partial z} - \frac{\partial u}{\partial x}) & \mu(\frac{\partial u}{\partial y} + \frac{\partial v}{\partial x}) \\ \mu(\frac{\partial w}{\partial x} + \frac{\partial u}{\partial z}) & \mu(\frac{\partial w}{\partial y} + \frac{\partial v}{\partial z}) & \frac{2}{3}\mu(2\frac{\partial w}{\partial z} - \frac{\partial u}{\partial x} - \frac{\partial v}{\partial y}) \end{pmatrix}. \tag{2.22}$$

The heat conduction vectors are given by the Fourier heat law:

$$\begin{pmatrix} q_{tx} \\ q_{ty} \\ q_{tz} \end{pmatrix} = \begin{pmatrix} -\kappa_t \frac{\partial T}{\partial x} \\ -\kappa_t \frac{\partial T}{\partial y} \\ -\kappa_t \frac{\partial T}{\partial z} \end{pmatrix}, \tag{2.23}$$

$$\begin{pmatrix} q_{vx} \\ q_{vy} \\ q_{vz} \end{pmatrix} = \begin{pmatrix} -\kappa_v \frac{\partial T_v}{\partial x} \\ -\kappa_v \frac{\partial T_v}{\partial y} \\ -\kappa_v \frac{\partial T_v}{\partial z} \end{pmatrix}. \tag{2.24}$$

The diffusion velocity are given by the Fick's law:

$$\begin{pmatrix} \rho_s u_s \\ \rho_s v_s \\ \rho_s w_s \end{pmatrix} = \begin{pmatrix} -\rho D_s \frac{\partial c_s}{\partial x} \\ -\rho D_s \frac{\partial c_s}{\partial y} \\ -\rho D_s \frac{\partial c_s}{\partial z} \end{pmatrix}. \tag{2.25}$$

2.2.2 Transport coefficients

The species viscosity except for the electron is given by a viscosity model for reaction flow developed by Blottner et al [3].

$$\mu_s = 0.1 \exp[(A_s \ln T + B_s)\ln T + C_s], \tag{2.26}$$

where A_s, B_s and C_s are found in Table 2.3.

The conductivities of translational-rotational temperature and vibrational-electronic temperature for each species are given by Eucken's relation [4] as

$$\kappa_{ts} = \mu_s \left(\frac{5}{2} c_{vtrs} + c_{vrots}\right), \tag{2.27}$$

$$\kappa_{vs} = \mu_s c_{vvs}, \tag{2.28}$$

where C_{vtrs}, C_{vrots} and C_{vvs} are given by

$$c_{vtrs} = \frac{R}{M_s}, \tag{2.29}$$

$$c_{vrots} = \begin{cases} \frac{R}{M_s} & \text{for NO, } O_2\text{, } N_2 \\ 0 & \text{for O, N} \end{cases}, \tag{2.30}$$

$$c_{vvs} = \begin{cases} \frac{R}{M_s} & \text{for NO, } O_2\text{, } N_2 \\ 0 & \text{for O, N} \end{cases}, \tag{2.31}$$

Moreover, the total viscosity and conductivity of the gas are calculated using Wilke's semi-empirical mixing rule [5],

$$\mu = \sum_s \frac{X_s \mu_s}{\phi_s}, \tag{2.32}$$

$$\kappa_t = \sum_s \frac{X_s \kappa_{ts}}{\phi_s}, \tag{2.33}$$

$$\kappa_v = \sum_s \frac{X_s \kappa_{vs}}{\phi_s}. \tag{2.34}$$

where

$$X_s = \frac{\frac{\rho_s}{M_s}}{\sum_r \frac{\rho_r}{M_r}}, \tag{2.35}$$

$$\phi_s = \sum_r X_r \left[1 + \sqrt{\frac{\mu_s}{\mu_r}} \left(\frac{M_r}{M_s}\right)^{\frac{1}{4}}\right]^2 \left[\sqrt{8\left(1 + \frac{M_s}{M_r}\right)}\right]^{-1}. \tag{2.36}$$

if we neglect the thermal diffusion effect and the pressure diffusion effect, the diffusion velocity of each component of the gas mixture is proportional to the gradient of mass concentration. Therefore, the diffusive fluxes are written as

$$\rho_s u_s = \rho D_s \frac{\partial c_s}{\partial x}, \tag{2.37}$$

$$\rho_s v_s = \rho D_s \frac{\partial c_s}{\partial y}, \tag{2.38}$$

$$\rho_s w_s = \rho D_s \frac{\partial c_s}{\partial z}. \tag{2.39}$$

Because we assume the diffusion coefficients to be constant for all species with constant Schmidt number of 0.5, the diffusion coefficients can be written as

$$D_s = \frac{\mu}{Sc\rho}. \tag{2.40}$$

2.2.3 Thermochemical model

Equation of state

The total energy E is made up of the separate components of energy which can be written as

$$E = \sum_s \rho_s c_{vs} T + E_v + E_{el} + \sum_s \rho_s h_s^0 + \frac{1}{2}\rho(u^2 + v^2 + w^2). \tag{2.41}$$

The translational-rotational temperature T can be calculated by solving the above equation. The specific heat at constant volume for species s for translational-rotational energy is given by

$$c_{vs} = c_{vtrs} + c_{vrots}. \tag{2.42}$$

The formation enthalpy h_s^0 for species s is shown in Table 2.4.

The vibrational energy for species s contained in a harmonic oscillator at the vibrational temperature T_v is expressed as

$$E_v = \sum_s \rho_s e_{vs}. \tag{2.43}$$

$$e_{vs} = \frac{R}{M_s} \frac{\Theta_{vs}}{\exp\left(\frac{\Theta_{vs}}{T_v}\right) - 1}, \tag{2.44}$$

where θ_{vs} is the characteristic temperature of vibration given in Table2.5. The expression for the energy contained in the excited electronic states comes from the assumption that they are populated according to a Boltzmann distribution governed by the electronic temperature given by T_v in the present two-temperature model. The electronic energy considered up to the first excitation state can be written as

$$E_{el} = \sum_s \rho_s e_{els}. \tag{2.45}$$

$$e_{els} = \frac{R}{M_s} \frac{g_{1s}\Theta_{els} \exp\left(\frac{-\Theta_{els}}{T_v}\right)}{g_{0s} + g_{1s} \exp\left(\frac{-\Theta_{els}}{T_v}\right)} \quad (s = \mathrm{O}, \mathrm{N}, \mathrm{O_2}), \tag{2.46}$$

where g_{0s} and g_{1s} are the degeneracies of the ground state and the first excitation state, respectively, and θ_{els} is the characteristic temperature of the first excitation state. These constants are found in Table 2.6

The static pressure p is given by a sum of the partial pressures,

$$p = \sum_s \rho_s \frac{R}{M_s} T. \tag{2.47}$$

The enthalpy per unit mass h_s is defined to be

$$h_s = c_{vs} T + \frac{R}{M_s} T + e_{vs} + e_{els} + h_s^0. \tag{2.48}$$

The vibrational temperature is obtained by solving the following relation for vibrational and electronic energies using the Newton iteration method.

$$E_v + E_{el} = function(\rho_s, T_v). \tag{2.49}$$

Chemical reaction model

Following 17 chemical reactions are considered.

$$\mathrm{O_2 + M \rightleftharpoons O + O + M}, \tag{2.50}$$
$$\mathrm{N_2 + M \rightleftharpoons N + N + M}, \tag{2.51}$$
$$\mathrm{NO + M \rightleftharpoons N + O + M}, \tag{2.52}$$
$$\mathrm{N_2 + O \rightleftharpoons NO + N}, \tag{2.53}$$
$$\mathrm{NO + O \rightleftharpoons O_2 + N}, \tag{2.54}$$

where M is the third body (O, N, NO, O_2, N_2). The forward and backward reaction rate coefficients are obtained by

$$k_{fi} = C_{fi} T_a^{\eta_i} \exp\left(\frac{-\Theta_i}{T_a}\right), \tag{2.55}$$

$$k_{bi} = \frac{k_{fi}}{K_{eqi}}, \tag{2.56}$$

where the Arrhenius parameters C_{fi}, η_i and Θ_i are summarized in Table 2.7. These values refer to Ref. [6]. We use the Bose and Candler's rate coefficients for the NO

exchange reaction [7, 8]. The equilibrium constants K_{eq} are curve-fitted in the form that fits to experimental data as

$$K_{eqi} = \exp\left(A_{i1}Z + A_{i2} + A_{i3}\ln\frac{1}{z} + A_{i4}\frac{1}{z} + A_{i5}\frac{1}{z^2}\right), \tag{2.57}$$

where

$$Z = T_a/10000. \tag{2.58}$$

The constants $A_{i1}\sim A_{i5}$ are given in Table 2.8, which are summarized in Ref. [2]. The forward rate coefficients for the dissociation reactions (reaction 1-15 in Table 2.7) are assumed to be a function of the geometric-averaged temperature between translational and vibrational temperatures, while the ones for the NO exchange reaction (reaction 16 and 17 in Table 2.7) depend only on the translational temperature.

$$k_f = k_f(T_a), T_a = \sqrt{TT_v} \quad \text{or} \quad T_a = \sqrt{T}. \tag{2.59}$$

The total reaction rates of each reaction can be written as

$$R_1 = \sum_s \left[k_{f1,s}\frac{\rho_{\mathrm{O}_2}}{M_{\mathrm{O}_2}}\frac{\rho_s}{M_s} - k_{b1,s}\left(\frac{\rho_{\mathrm{O}}}{M_O}\right)^2\frac{\rho_s}{M_s}\right], \tag{2.60}$$

$$R_2 = \sum_s \left[k_{f2,s}\frac{\rho_{\mathrm{N}_2}}{M_{\mathrm{N}_2}}\frac{\rho_s}{M_s} - k_{b2,s}\left(\frac{\rho_{\mathrm{N}}}{M_N}\right)^2\frac{\rho_s}{M_s}\right], \tag{2.61}$$

$$R_3 = \sum_s \left[k_{f3,s}\frac{\rho_{\mathrm{NO}}}{M_{\mathrm{NO}}}\frac{\rho_s}{M_s} - k_{b3,s}\frac{\rho_{\mathrm{N}}}{M_{\mathrm{N}}}\frac{\rho_{\mathrm{O}}}{M_{\mathrm{O}}}\frac{\rho_s}{M_s}\right], \tag{2.62}$$

$$R_4 = k_{f4}\frac{\rho_{\mathrm{N}_2}}{M_{\mathrm{N}_2}}\frac{\rho_{\mathrm{O}}}{M_{\mathrm{O}}} - k_{b4}\frac{\rho_{\mathrm{NO}}}{M_{\mathrm{NO}}}\frac{\rho_{\mathrm{N}}}{M_{\mathrm{N}}}, \tag{2.63}$$

$$R_5 = k_{f5}\frac{\rho_{\mathrm{NO}}}{M_{\mathrm{NO}}}\frac{\rho_{\mathrm{O}}}{M_{\mathrm{O}}} - k_{b5}\frac{\rho_{\mathrm{O}_2}}{M_{\mathrm{O}_2}}\frac{\rho_{\mathrm{N}}}{M_{\mathrm{N}}}. \tag{2.64}$$

The chemical source terms $\dot{W}_s$ are given by

$$\dot{W}_{\mathrm{O}} = M_{\mathrm{O}}(2R_1 + R_3 - R_4 - R_5), \tag{2.65}$$

$$\dot{W}_{\mathrm{N}} = M_{\mathrm{N}}(2R_2 + R_3 + R_4 + R_5), \tag{2.66}$$

$$\dot{W}_{\mathrm{NO}} = M_{\mathrm{NO}}(-R_3 + R_4 - R_5), \tag{2.67}$$

$$\dot{W}_{\mathrm{O}_2} = M_{\mathrm{O}_2}(-R_1 + R_5), \tag{2.68}$$

$$\dot{W}_{\mathrm{N}_2} = M_{\mathrm{N}_2}(-R_2 - R_4). \tag{2.69}$$

Energy exchanges among different modes

The vibrational source term $\dot{W}_v$ can be written as

$$\dot{W}_v = Q_{T-V} + Q_{D-V} + Q_{E-Ex}. \tag{2.70}$$

The first term of the right hand side of Eq.(2.70) Q_{T-V} is the rate of energy exchange between the translational and the vibrational modes. This is given by the Landau-Teller equation with the Park's diffusion model[2],

$$Q_{T-V} = \sum_s \rho_s \frac{e^*_{vs}(T) - e_{vs}}{\tau_{sLT} + \tau_{cs}} \left| \frac{T_{\text{shock}} - T_v}{T_{\text{shock}} - T_{v\ \text{shock}}} \right|^{s-1}, \tag{2.71}$$

$$s = 3.5 \exp\left(-\frac{5000}{T_{\text{shock}}}\right), \tag{2.72}$$

where τ_{sLT} and τ_{cs} are Landau-Teller relaxation time and Park's collisional limit time, respectively. e_{vs} is vibrational energy per unit mass at T_v. $e^*_{vs}(T_t)$ is one at T. A preferential dissociation model is also included in the calculation. T_{shock} and T_{vshock} are the translational-rotational temperature and vibrational-electronic temperature behind the shock. For Landau-Teller relaxation time τ_{sLT}, the Millikan-White relaxation time [9] is employed.

$$\tau_{sLT} = \frac{\sum_s X_r}{\sum_r \left(\frac{X_r}{\tau_{srLT}}\right)}, \tag{2.73}$$

$$\tau_{srLT} = \frac{1}{p} \exp\left\{A_{sr}\left(T^{-1/3} - B_{sr}\right) - 18.42\right\} \ p \ in \ \text{atm}. \tag{2.74}$$

The constant A_{sr} and B_{sr} are found in Table 2.9. The collision limited relaxation time τ_{cs} is given by

$$\tau_{cs} = \frac{1}{\bar{c}_s \sigma_{sr} n_s}, \tag{2.75}$$

where c_s and σ_{sr} are the averaged molecular speed of s species and the limiting collision cross-section, respectively.

$$\bar{c}_s = \sqrt{\frac{8RT}{\pi M_s}}, \tag{2.76}$$

$$\sigma_{sr} = 10^{-21}(5000/T)^2. \tag{2.77}$$

The second term of the right hand side of Eq. (2.70) Q_{D-V} is the rate of energy loss due to dissociation. In the present study, the preferential dissociation model is used [2]. The averaged vibrational energy losses or gain through dissociation or recombination reactions is set to be 30 % of the corresponding dissociation energy as follows:

$$Q_{D-V} = \sum_s \hat{D}_s \dot{W}_s, \tag{2.78}$$

$$\hat{D}_s = 0.3\Theta_s, \tag{2.79}$$

where Θ_s is show in Table 2.7.

The last term of the right hand side of Eq. (2.70) Q_{E-Ex} is the rate of energy exchange in electronic excitation that is given by

$$Q_{E-Ex} = \sum_s e_{els} \dot{W}_s. \tag{2.80}$$

2.2.4 Discretization of the governing equations

Governing equations are discritized by the cell-centered finite volume method. The integrated form of Eq. (2.1) with respect to arbitrary volume Ω is

$$\iiint_\Omega \left\{ \frac{\partial \boldsymbol{Q}}{\partial t} + \frac{\partial (\boldsymbol{F} - \boldsymbol{F}_{\rm vis})}{\partial x} + \frac{\partial (\boldsymbol{G} - \boldsymbol{G}_{\rm vis})}{\partial y} + \frac{\partial (\boldsymbol{H} - \boldsymbol{H}_{\rm vis})}{\partial z} \right\} dV = \iiint_\Omega \boldsymbol{W} dV. \tag{2.81}$$

We use the divergence theorem of Gauss for convective and viscous flux vectors,

$$\frac{\partial}{\partial t} \iiint_\Omega \boldsymbol{Q} dV + \iint_{\partial\Omega} \{ (\boldsymbol{F} - \boldsymbol{F}_{\rm vis}) n_x + (\boldsymbol{G} - \boldsymbol{G}_{\rm vis}) n_y + (\boldsymbol{H} - \boldsymbol{H}_{\rm vis}) n_z \} \, dS = \iiint_\Omega \boldsymbol{W} dV, \tag{2.82}$$

where (n_x, n_y, n_z) is the component of the normal vector to the cell interface. The normal vector of convective and viscous flux vector to the cell interface are defined as follows:

$$\boldsymbol{P} = n_x \boldsymbol{F} + n_y \boldsymbol{G} + n_z \boldsymbol{H}, \tag{2.83}$$

$$\boldsymbol{P}_{\rm vis} = n_x \boldsymbol{F}_{\rm vis} + n_y \boldsymbol{G}_{\rm vis} + n_z \boldsymbol{H}_{\rm vis}. \tag{2.84}$$

The cell averaged values, volume of cell, area of cell and interval of time are defined as follows:

$$\widetilde{\boldsymbol{Q}} \equiv \frac{\iiint_\Omega \boldsymbol{Q} dV}{\iiint_\Omega dV}, \quad \widetilde{\boldsymbol{W}} \equiv \frac{\iiint_\Omega \boldsymbol{W} dV}{\iiint_\Omega dV}, \quad \Delta V \equiv \iiint_\Omega dV, \quad \Delta S \equiv \iint_{\partial\Omega} dS, \quad \Delta t \equiv \partial t \tag{2.85}$$

Eq. (2.82) becomes

$$\Delta\widetilde{\boldsymbol{Q}} + \frac{\Delta t}{\Delta V}\sum_{\partial\Omega}\left\{(\boldsymbol{P} - \boldsymbol{P}_{\mathrm{vis}})\right\}\Delta S = \Delta t\widetilde{\boldsymbol{W}}, \tag{2.86}$$

Eq.(2.86) in Euler implicit scheme is written as

$$\Delta\widetilde{\boldsymbol{Q}} + \frac{\Delta t}{\Delta V}\sum_{\partial\Omega}\left\{\boldsymbol{P}^n - \boldsymbol{P}^n_{\mathrm{vis}} + \left(\frac{\partial \boldsymbol{P}}{\partial\widetilde{\boldsymbol{Q}}} - \frac{\partial \boldsymbol{P}_{\mathrm{vis}}}{\partial\widetilde{\boldsymbol{Q}}}\right)\Delta\widetilde{\boldsymbol{Q}}\right\}\Delta S = \left\{\widetilde{\boldsymbol{W}}^n + \frac{\partial\widetilde{\boldsymbol{W}}}{\partial\widetilde{\boldsymbol{Q}}}\right\}\Delta t, \tag{2.87}$$

where the Jacobian matrix of the source term $\dot{W}$ are given by

$$\frac{\partial\dot{\boldsymbol{W}}}{\partial\widetilde{\boldsymbol{Q}}} = \begin{pmatrix} 0 & 0 & 0 & 0 & 0 & 0 & 0 & 0 & 0 \\ \vdots & \vdots & \vdots & \vdots & \vdots & \vdots & \vdots & \vdots & \vdots \\ 0 & 0 & 0 & 0 & 0 & 0 & 0 & 0 & 0 \\ \frac{\partial\dot{W}_{\mathrm{O}}}{\partial\rho} & \frac{\partial\dot{W}_{\mathrm{O}}}{\partial\rho u} & \frac{\partial\dot{W}_{\mathrm{O}}}{\partial\rho v} & \frac{\partial\dot{W}_{\mathrm{O}}}{\partial\rho w} & \frac{\partial\dot{W}_{\mathrm{O}}}{\partial E} & \frac{\partial\dot{W}_{\mathrm{O}}}{\partial\rho_{\mathrm{O}}} & \frac{\partial\dot{W}_{\mathrm{O}}}{\partial\rho_{\mathrm{N}}} & \frac{\partial\dot{W}_{\mathrm{O}}}{\partial\rho_{\mathrm{NO}}} & \frac{\partial\dot{W}_{\mathrm{O}}}{\partial(E_v+E_{el})} \\ \frac{\partial\dot{W}_{\mathrm{N}}}{\partial\rho} & \frac{\partial\dot{W}_{\mathrm{N}}}{\partial\rho u} & \frac{\partial\dot{W}_{\mathrm{N}}}{\partial\rho v} & \frac{\partial\dot{W}_{\mathrm{N}}}{\partial\rho w} & \frac{\partial\dot{W}_{\mathrm{N}}}{\partial E} & \frac{\partial\dot{W}_{\mathrm{N}}}{\partial\rho_{\mathrm{O}}} & \frac{\partial\dot{W}_{\mathrm{N}}}{\partial\rho_{\mathrm{N}}} & \frac{\partial\dot{W}_{\mathrm{N}}}{\partial\rho_{\mathrm{NO}}} & \frac{\partial\dot{W}_{\mathrm{N}}}{\partial(E_v+E_{el})} \\ \frac{\partial\dot{W}_{\mathrm{NO}}}{\partial\rho} & \frac{\partial\dot{W}_{\mathrm{NO}}}{\partial\rho u} & \frac{\partial\dot{W}_{\mathrm{NO}}}{\partial\rho v} & \frac{\partial\dot{W}_{\mathrm{NO}}}{\partial\rho w} & \frac{\partial\dot{W}_{\mathrm{NO}}}{\partial E} & \frac{\partial\dot{W}_{\mathrm{NO}}}{\partial\rho_{\mathrm{O}}} & \frac{\partial\dot{W}_{\mathrm{NO}}}{\partial\rho_{\mathrm{N}}} & \frac{\partial\dot{W}_{\mathrm{NO}}}{\partial\rho_{\mathrm{NO}}} & \frac{\partial\dot{W}_{\mathrm{NO}}}{\partial(E_v+E_{el})} \\ \frac{\partial\dot{W}_{\mathrm{v}}}{\partial\rho} & \frac{\partial\dot{W}_{\mathrm{v}}}{\partial\rho u} & \frac{\partial\dot{W}_{\mathrm{v}}}{\partial\rho v} & \frac{\partial\dot{W}_{\mathrm{v}}}{\partial\rho w} & \frac{\partial\dot{W}_{\mathrm{v}}}{\partial E} & \frac{\partial\dot{W}_{\mathrm{v}}}{\partial\rho_{\mathrm{O}}} & \frac{\partial\dot{W}_{\mathrm{v}}}{\partial\rho_{\mathrm{N}}} & \frac{\partial\dot{W}_{\mathrm{v}}}{\partial\rho_{\mathrm{NO}}} & \frac{\partial\dot{W}_{\mathrm{v}}}{\partial(E_v+E_{el})} \end{pmatrix}. \tag{2.88}$$

The convective numerical flux is calculated using the SLAU scheme [10, 11]. The viscous flux is evaluated by a central difference scheme. We employ the MUSCL approach [12] to attain second-order spatial accuracy. For time integration, we use the LU-SGS method [13], and the diagonal point implicit method [14] is utilized in order to improve stability in the integration of the source terms.

$$\frac{\partial\dot{\boldsymbol{W}}}{\partial\widetilde{\boldsymbol{Q}}} \approx \mathrm{diag}\left(0 \ \cdots \ 0 \ \ \frac{1}{\tau_{\mathrm{O}}} \ \ \frac{1}{\tau_{\mathrm{N}}} \ \ \frac{1}{\tau_{\mathrm{NO}}} \ \ \frac{1}{\tau_v}\right), \tag{2.89}$$

where τ_s and τ_v are the characteristic time of species s and translational-vibrational

relaxation.

$$\frac{1}{\tau_s} = \beta\sqrt{\sum_r \left(\frac{\partial \dot{W}_s}{\partial \rho_r}\right)^2}, \quad \frac{1}{\tau_v} = \left|\frac{\partial \dot{W}_v}{\partial \left(E_v + E_{el}\right)}\right|, \tag{2.90}$$

where β is the relaxation coefficient which is set to be the larger than unit.

2.2.5 Radiation Calculation

The radiative transfer equation is solved by tangent-slab approximation [15]. In a one-dimensional local-thermodynamic-equilibrium medium, the radiative transfer equation is given by

$$l\frac{\partial I_\lambda}{\partial n} = \kappa_\lambda \left(B_\lambda - I_\lambda\right), \tag{2.91}$$

where $l = \cos\phi$. The coordinate system is shown in Fig. 2.3. Radiation intensities at each cell interface are obtained by solving Eq. (2.91) along only the cells that are normal to the wall surface in the tangent-slab approximation. The Planck function B_λ is a function of the vibrational temperature T_v and is given by

$$B_\lambda = \frac{2hc^2}{\lambda^5}\frac{\exp\left(-hck/\lambda T_v\right)}{1-\exp\left(-hck/\lambda T_v\right)}, \tag{2.92}$$

where h and k indicate the Planck constant and the Boltzman constant, respectively. The formal solution of Eq. (2.91) is given by

$$\begin{aligned} I_\lambda\left(s,l\right) = I_\lambda\left(s_b,l\right)\exp\left[-\frac{\tau_\lambda(s)-\tau_\lambda(s_b)}{l}\right] \\ + \int_{s_b}^{s}\frac{\kappa_\lambda B_\lambda}{l}\exp\left[-\frac{\tau_\lambda(s)-\tau_\lambda(\hat{s})}{l}\right]d\hat{s}. \end{aligned} \tag{2.93}$$

where the subscripts b means the cell interface. $\tau_\lambda(s)$ is the optical thickness from the cell interface which is given by

$$\tau_\lambda(s) = \int_{s_b}^{s}\kappa_\lambda d\hat{s}. \tag{2.94}$$

The spectral radiation heat flux is given by integrating $I_\lambda \times \cos\phi$ over the solid angle $d\Omega = \sin\phi d\phi d\theta$,

$$\begin{aligned} q_\lambda &= \int_{4\pi} I_\lambda l d\Omega, \\ &= \int_0^{2\pi}\int_0^{\pi} I_\lambda l \sin\phi d\phi d\theta, \\ &= 2\pi \int_0^{\pi} I_\lambda l \sin\phi d\phi, \\ &= 2\pi \int_{-1}^{1} I_\lambda l dl, \\ &= q_\lambda^+ - q_\lambda^-. \end{aligned} \tag{2.95}$$

The total radiation heat flux q_{rad} is then given by

$$q_{rad} = \int_\lambda q_\lambda \lambda. \tag{2.96}$$

The flowfield calculation and radiative transport calculation are uncoupled. The radiative heat flux is calculated from the solution of steady-state flowfield.

The absorption coefficients are calculated using the multiband radiation model [16]. O, N, NO, O_2 and N_2 are considered as contributors to radiation. The absorption coefficients are evaluated at 10,000 wavelength range from 750 to 15,000 $\mathring{A}$. The absorption coefficients of the gas mixture are expressed as a sum of those for individual species in the form of

$$\kappa_\lambda = \sum_s n_s \sigma_\lambda^s, \tag{2.97}$$

where n_s is the number density and σ_λ^s is the cross section of species s. The cross section values σ_λ^s are curve-fitted using five parameters in the form of

$$\sigma_\lambda^s = \exp\left(A_{1\lambda}^s/Z + A_{2\lambda}^s + A_{3\lambda}^s \ln(Z) + A_{4\lambda}^s Z + A_{1\lambda}^s Z^2\right), \tag{2.98}$$

where $Z = 10000/T$.

Radiation form impurities

In these calculations, radiative heat flux is computed by utilizing tangent slab approximation employed in the evaluation of radiation from impurities in the shock

layer. However, the chemical species of impurities in test flow and the amount of impurities are unknown, and therefore, we cannot determine the radiation intensity from impurities. In this study, we assume the impurities as a grey body at the average shock layer temperature. The average temperature is determined along the wall-normal direction in between the end of the relaxation region behind the shock wave and the edge of the boundary layer. The Planck function B_λ multiplied by the emissivity ϵ is set as a boundary condition of Eq. (3). The emissivity ϵ is determined at the stagnation point in order to reproduce the experimental heat flux.

2.3 Numerical Conditions

2.3.1 Upstream and wall boundary conditions

Table 2.1 and 2.2 summarize the upstream parameters and test models for the aero-heating measurement campaign. [1, 17] These values were determined using a JAXA in-house code [18]. The upstream conditions for flowfield calculation are set same values as the values Table 2.1 and 2.2. We set same values for the flowfield calculation For the wall boundary conditions, an isothermal and fully-catalytic wall are assumed for all cases. Figure 2.4 shows the dependence of the surface catalysis on the convective heat flux at Shot No. 1783 where the stagnation enthalpy is highest, and the surface catalysis is likely to affect the convective heat flux in all cases in Table 2.1. One can find that the difference is ignorable. The dependence of the wall temperature on convective heat flux is also investigated. Figure 2.5 shows the heat flux at the wall temperatures of 300, 500 and 700 K. The differences are negligibly small. Since the wall temperature becomes about 500 K in the experiment, the wall temperature is set to be 500 K.

2.3.2 Test models and computational grids

Three different test models, namely the Apollo CM model and two probe models of different size, referred to as $R100$ and $R10$, are employed in the heat flux measure-

ments conducted in HIEST [17, 19]. Figure 2.6 (a) shows the Apollo CM 6.4 % scaled test model, which has a nose radius of 300 mm, and is the largest among the models. On the other hand, small radius probe $R100$ shown in Fig. 2.6 (b) has a nose radius of 100 mm. Though not shown, small radius probe $R10$ has a similar shape. A typical example of the computational grid for the Apollo CM model at an angle of attack (AoA) of 30 deg is shown in Fig. 2.7. It is a structured mesh having 51 points in the normal direction from the surface toward the outer boundary, 51 points along the surface, and 65 points in the circumferential direction. The minimum grid spacing at the wall surface satisfies the cell Reynolds number of Re_{cell}=1. Several mesh surfaces are clustered and aligned parallel to the shock wave using the solution adaptive technique which is critically important particularly when a structured mesh is employed in the evaluation of heat flux profiles [20]. Figure 2.8 shows the computed convective heat flux using solution adaptive mesh and no adaptive mesh at Shot No. 1791. For the no adaptive mesh, the grids are not clustered or aligned parallel to the shock wave. One can find that the heat flux distribution by the no adaptive mesh oscillates near the stagnation region. However, numerical errors appeared at $x = y = z = 0$ m. This is due to the singularity of the grid. Since this error does not effect heat flux in the other region, treatment for this error is out of the scope of this study.

2.4 Results and Discussions

2.4.1 Radiation from air species in shock layer

Figure 2.9 shows the radiation heat flux profiles from air species in the shock layer for Shot No. 1781 and 1783, with associated convective heat flux profiles. Although radiation heat flux becomes larger in the higher enthalpy condition, it is negligibly small compared to the corresponding convective heat flux. It should be noted that tangent slab approximation generally gives a higher radiation heat flux incident on the surface of blunt bodies. Nevertheless, the computed radiation heat flux is far smaller than that of convective heat flux. This concludes that radiation from air species in

the shock layer cannot explain the augmented heat flux observed in HIEST.

2.4.2 Abnormal heat flux augmentation and radiation from impurities in shock layer

The augmentations of heat flux at various stagnation enthalpy conditions and test models are plotted in Fig. 2.10 (a) and (b) in terms of the average vibrational temperature and maximum vibrational temperature, respectively. Figure 2.11 shows the translational temperature and vibrational temperature profiles along the stagnation stream line at Shot No. 1781 and 1783. To define the average temperature, we take into account the vibrational temperature in the shock layer except the low-temperature region near the wall surface. The location of the maximum vibrational temperature is immediately behind the shock wave. The augmentations of heat flux, and the average temperature and maximum vibrational temperature are summarized in Table 2.10. For the lower enthalpy conditions such as Shot No. 1781 shown in Fig. 2.11 (a), the maximum vibrational temperature is higher than the average temperature. On the other hand, for higher enthalpy conditions such as Shot No. 1783 shown in Fig. 2.11 (b), the maximum vibrational temperature is comparable to the average temperature. The impurities that are heated due to the high temperature in the shock layer can emit radiation at the temperature of the heated impurities. We assume that the temperature of impurities equilibrates with the average vibrational temperature or the maximum vibrational temperature. The relation between the augmentation of heat flux and these temperatures is investigated. Using the average temperature $T_{v\mathrm{ave}}$, augmentation is fairly well fitted by $\epsilon\sigma T_{v\mathrm{ave}}^4$ where σ denotes the Stefan-Boltzmann constant. In Fig. 2.10 (a), the emissivity is determined as $\epsilon = 0.132$.

Using this fitted emissivity, the sum of the convective and radiation heat fluxes, referred to as the total heat flux, is compared with the measured heat flux profiles obtained in HIEST. In Fig. 2.12, the computed convective and total heat fluxes are plotted for the Apollo CM model with an AoA of 0 deg using the corresponding

experimental data. One can find that the computed total heat flux profiles agree fairly well with the experimental data over the entire surface. Similarly, in Fig. 2.13, the convective, total and the corresponding experimental data are plotted for an AoA of 30 deg. Reasonable agreements are also obtained with the same emissivity. Therefore, this indicates that the augmentation of heat flux can be estimated using $0.132\sigma T_{v\mathrm{ave}}^4$.

The ratio of the abnormal heat flux to total heat flux at lower enthalpy conditions and higher enthalpy conditions is shown in Fig. 2.14. One can find that the abnormal heat flux augmentation was not significant for small radius probes. The detailed heat flux data at various enthalpy conditions and test models are summarized in the Table 2.10. When heat flux augmentation is defined as $\Delta q \equiv q_{\mathrm{exp.}} - q_{\mathrm{calc.}}$ at the stagnation point, it is nearly identical as the stagnation enthalpies are close. For example, the surplus heat fluxes in Shot No. 1891 for the Apollo CM model and $R100$ probe model are 2.79 MW/m^2 and 2.97 MW/m^2, respectively, even though the computed shock stand-off distance for the Apollo CM model (=26 mm) is significantly larger than that for $R100$ probe model (=7 mm). Furthermore, the surplus heat flux in Shot No. 1889 for the $R10$ probe model is 3.26 MW/m^2, which is close to that in Shot No. 1891 for the Apollo CM model and $R100$, while the stagnation enthalpy in both Shots is also close. The shock stand-off distance in Shot No. 1891 for the Apollo CM test model (=26 mm) is 26 times larger than that in Shot No. 1889 for $R10$ (=1 mm). A similar trend can be observed for the Apollo CM model in Shot No. 1783, the Apollo CM model in Shot No. 1893 and $R100$ probe model in Shot No. 1893, where the surplus heat fluxes are 16.46 MW/m^2 18.89 MW/m^2 and 13.92 MW/m^2, respectively. The surplus heat fluxes for the Apollo CM model are only 1.18-1.36 times larger than those for the $R100$ probe model. The above results suggest that the augmentation depends only on stagnation enthalpy. Because the convective heat flux becomes substantially higher for small nose radii, the resulting ratio of $q_{\mathrm{exp.}}/q_{\mathrm{calc.}}$ becomes almost unity for small radius probes. These results also indicate the reason why the abnormal heat flux augmentation becomes significant in HIEST. In HIEST,

a larger test model can be used and the q/q_{cal} ratio becomes smaller.

2.5 Conclusions

The abnormal heat flux augmentation observed in HIEST was numerically analyzed. The analysis revealed the followings. (1) Radiation from air species was too small to contribute to heat flux augmentation. (2) The engineering technique to estimate the abnormal heat flux augmentation was obtained, though the test campaign for spectroscopy in the shock layer was required to clearly determine the source of the radiation. The abnormal heat flux augmentation could be estimated using $0.132\sigma T_{\mathrm{ave}}^4$ and the computed total heat flux profiles agreed fairly well with the experimental data. (3) The reason why the abnormal heat flux augmentation became significant in HIEST that the $q_{\mathrm{abnormal}}/q_{\mathrm{cal}}$ ratio becomes larger at large test model.

Table. 2.1 Test models and upstream conditions computed by JAXA in-house code[18].

Shot No.	Test Model	H_0 [MJ/kg]	$T_{t\infty}$ [K]	$T_{v\infty}$ [K]	ρ_∞ [kg/m^3]	M_∞
1781	Apollo	6.849	662.4	679.2	0.01978	6.721
1782	Apollo	17.275	1861.1	1864.9	0.01686	5.945
1783	Apollo	21.537	2158.9	2163.1	0.01216	5.890
1784	Apollo	19.554	2035.2	2038.2	0.01457	5.909
1785	Apollo	21.059	2143.0	2146.8	0.01315	5.885
1787	Apollo	8.094	841.7	849.5	0.02643	6.496
1791	Apollo	6.759	649.7	668.1	0.01919	6.739
1886	$R10$	13.471	1455.9	1461.8	0.01633	6.108
1889	$R10$	8.596	908.7	915.8	0.02717	6.440
1891	$R100$/Apollo	8.318	869.9	877.3	0.02702	6.479
1893	$R100$/Apollo	20.048	1946.4	1952.3	0.01050	6.013

Table. 2.2 Upstream mass fractions computed by JAXA in-house code[18].

Shot No.	$C_{\mathrm{O}\infty}$	$C_{\mathrm{N}\infty}$	$C_{\mathrm{NO}\infty}$	$C_{\mathrm{O_2}\infty}$	$C_{\mathrm{N_2}\infty}$
1781	2.451×10^{-3}	4.333×10^{-12}	5.938×10^{-2}	2.008×10^{-1}	7.374×10^{-1}
1782	7.769×10^{-2}	5.311×10^{-7}	4.781×10^{-2}	1.308×10^{-1}	7.537×10^{-1}
1783	1.405×10^{-1}	5.612×10^{-7}	3.391×10^{-2}	7.461×10^{-2}	7.510×10^{-1}
1784	1.092×10^{-11}	2.035×10^{-6}	4.102×10^{-2}	1.022×10^{-1}	7.476×10^{-1}
1785	1.308×10^{-1}	4.514×10^{-6}	3.600×10^{-2}	8.326×10^{-2}	7.500×10^{-1}
1787	3.822×10^{-3}	4.483×10^{-12}	6.031×10^{-2}	1.991×10^{-1}	7.368×10^{-1}
1791	2.397×10^{-3}	4.399×10^{-12}	5.931×10^{-2}	2.009×10^{-1}	7.373×10^{-1}
1886	4.137×10^{-2}	4.204×10^{-8}	5.572×10^{-2}	1.633×10^{-1}	7.396×10^{-1}
1889	4.785×10^{-3}	5.819×10^{-12}	6.054×10^{-2}	1.979×10^{-1}	7.368×10^{-1}
1891	4.139×10^{-3}	4.738×10^{-12}	6.038×10^{-2}	1.986×10^{-1}	7.368×10^{-1}
1893	1.304×10^{-1}	3.300×10^{-6}	3.653×10^{-2}	8.320×10^{-2}	7.499×10^{-1}

Table. 2.3 Viscosity coefficients for the Blottner model

Species	A_s	B_s	C_s
O	0.0203144	0.4294404	-11.6031403
N	0.0115572	0.6031679	-12.4327495
NO	0.0436378	-0.0335511	-9.5767430
O_2	0.0449290	-0.0826158	-9.2019475
N_2	0.0268142	0.3177838	-11.3155513

Table. 2.4 Formation enthalpies

species	h_s^0 [MJ/kg]
O	15.588
N	33.755
NO	3.0077
O_2	0
N_2	0

Table. 2.5 Harmonic oscillator vibrational constants

Species	Θ_{vs} [K]
NO	2712
O_2	2260
N_2	3390

Table. 2.6 Characteristic temperatures and degeneracies of electronic levels

Species	Θ_{vs} [K]	g_{0s}	g_{1s}
O	22713	9	5
N	26498.5	4	10
O_2	11356.5	3	2

Table. 2.7 Forward chemical reaction rate coefficients

Reaction No. i	Reaction	Third body	C_{fi} [m^3/(mol·sec)]	η_i	Θ_i [K]	T_a [K]
1	$O_2 + M \rightleftharpoons O + O + M$	O	1.0×10^{16}	-1.5	59360	$\sqrt{T_t T_v}$
2		N	1.0×10^{16}			
3		NO	2.0×10^{15}			
4		O_2	2.0×10^{15}			
5		N_2	2.0×10^{15}			
6	$N_2 + M \rightleftharpoons N + N + M$	O	3.0×10^{16}	-1.6	113200	$\sqrt{T_t T_v}$
7		N	3.0×10^{16}			
8		NO	7.0×10^{15}			
9		O_2	7.0×10^{15}			
10		N_2	7.0×10^{15}			
11	$NO + M \rightleftharpoons N + O + M$	O	1.1×10^{11}	0.0	75500	$\sqrt{T_t T_v}$
12		N	1.1×10^{11}			
13		NO	1.1×10^{11}			
14		O_2	5.0×10^{9}			
15		N_2	5.0×10^{9}			
16	$N_2 + O \rightleftharpoons NO + N$	–	5.7×10^{6}	0.42	42938	T_t
17	$NO + O \rightleftharpoons O_2 + N$	–	8.4×10^{6}	0.0	19400	T_t

Table. 2.8 Fitting parameters for equilibrium constant

Reaction	i	A_{i1}	A_{i2}	A_{i3}	A_{i4}	A_{i5}
$O_2 + M \rightleftharpoons O + O + M$	1	0.553880	16.275511	1.776300	-6.75200	0.031445
$N_2 + M \rightleftharpoons N + N + M$	2	1.535100	15.421600	1.299300	-11.49400	-0.006980
$NO + M \rightleftharpoons N + O + M$	3	0.558890	14.531080	0.553960	-7.53040	-0.014089
$N_2 + O \rightleftharpoons NO + N$	4	0.976460	0.890430	0.745720	-3.96420	0.007123
$NO + O \rightleftharpoons O_2 + N$	5	0.004815	-1.744300	-1.222700	-0.95824	-0.045545

Table. 2.9 Coefficients for Millikan-White relaxation time

Collision partner	A_{sr}	B_{sr}
NO-O	49.5	0.042
NO-N	49.5	0.042
NO-NO	49.5	0.042
NO-O_2	49.5	0.042
NO-N_2	49.5	0.042
O_2-O	47.7	0.059
O_2-N	72.4	0.015
O_2-NO	136	0.0298
O_2-O_2	138	0.0300
O_2-N_2	134	0.0295
N_2-O	72.4	0.0150
N_2-N	180	0.0262
N_2-NO	225	0.0293
N_2-O_2	229	0 0295
N_2-N_2	221	0.0290

Table. 2.10 Abnormal heat flux augmentation at various enthalpy conditions and test models[18]

Shot No.	Test Model	H_0 [MJ/kg]	$q_{\text{exp.}}$ [MW/m^2]	$q_{calc.}$ [MW/m^2]	$q_{\text{exp.}}/q_{\text{calc.}}$	$q_{\text{exp.}} - q_{\text{calc.}}$ [MW/m^2]	$T_{v\text{ave}}$ [K]	$T_{v\text{max}}$ [K]
1781	Apollo	6.849	3.74	2.17	1.72	1.57	3958.6	4688.1
1782	Apollo	17.275	22.47	8.98	2.50	13.49	6654.1	6678.0
1783	Apollo	21.537	27.32	10.86	2.52	16.46	7057.4	7090.1
1784	Apollo	19.554	37.45	15.79	2.37	21.66	7133.9	7164.4
1785	Apollo	21.059	36.63	14.79	2.48	21.85	7273.0	7321.0
1787	Apollo	8.094	8.40	5.12	1.64	3.28	4466.8	5102.6
1791	Apollo	6.759	4.67	2.92	1.60	1.75	4024.4	4590.5
1886	Apollo	13.471	14.23	5.97	2.55	9.26	6001.8	6206.1
1891	Apollo	8.318	28.33	3.54	1.79	2.79	4428.4	5228.0
1893	Apollo	20.048	23.62	9.33	3.02	18.89	6844.6	6870.0
1889	$R10$	8.596	9.92	20.36	1.16	3.26	4804.5	5397.1
1891	$R100$	8.318	28.33	6.95	1.43	2.97	4558.7	5300.4
1893	$R100$	20.048	31.22	17.30	1.80	13.92	6821.5	6870.0

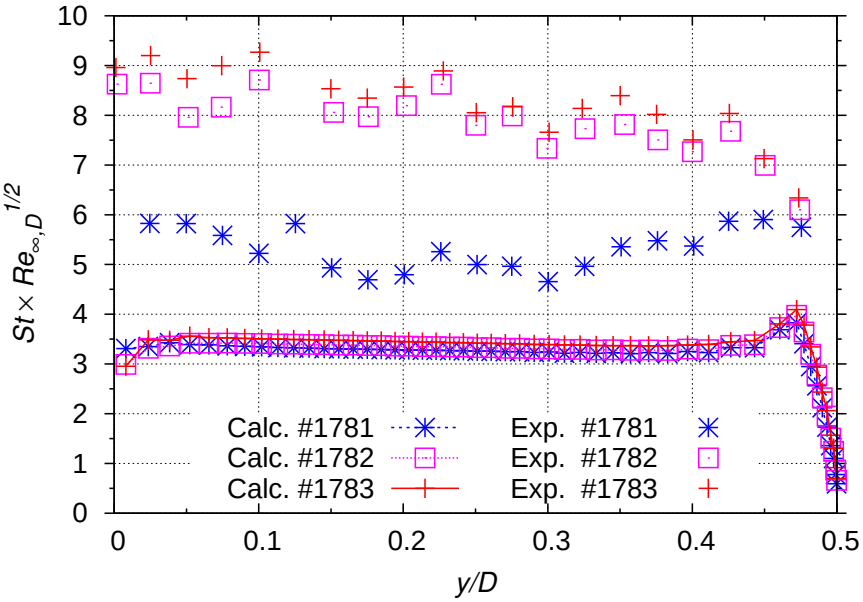

(a) AoA=0 deg

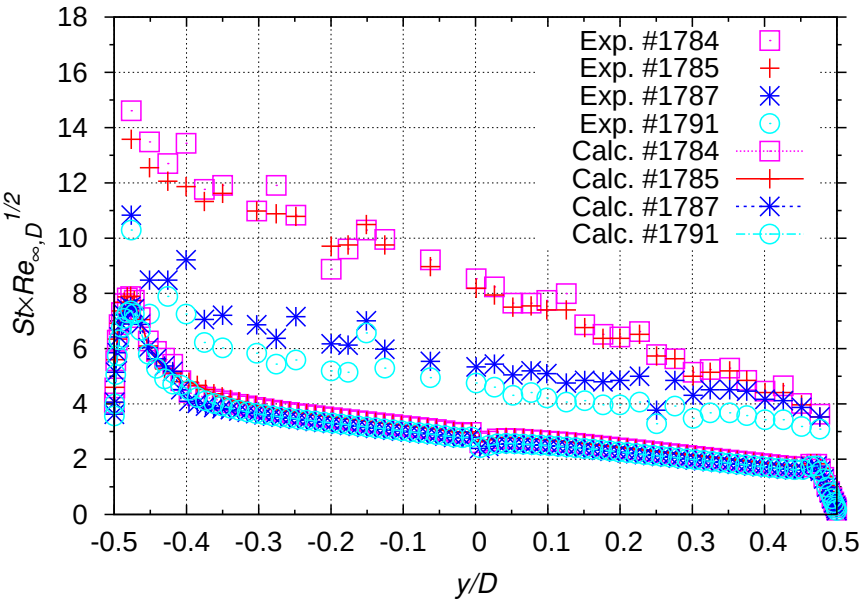

(b) AoA=30 deg

Fig. 2.1 Comparison of the calculated convective heat fluxes with the measured data on the heat-shield of Apollo CM test model.

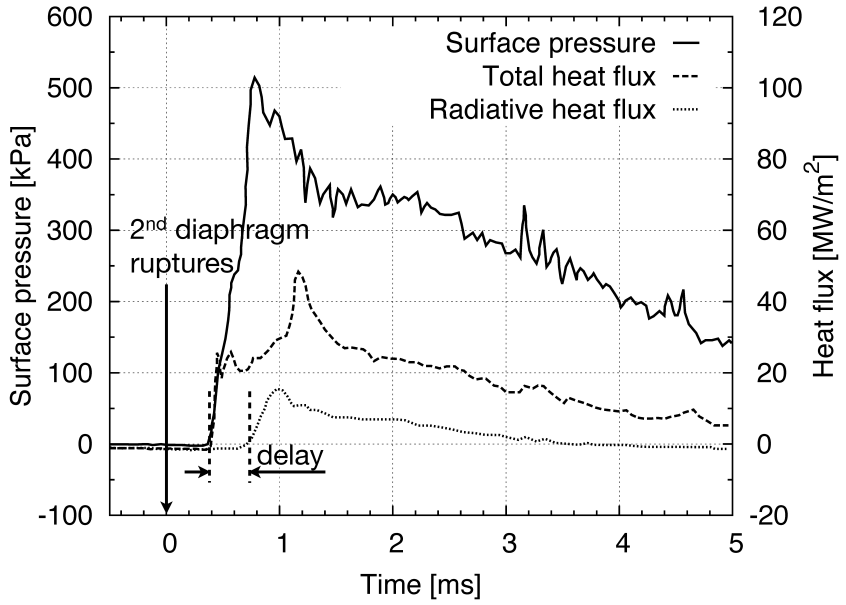

Fig. 2.2 Time history of surface pressure, total and radiative heat flux at stagnation point on the flat plate.

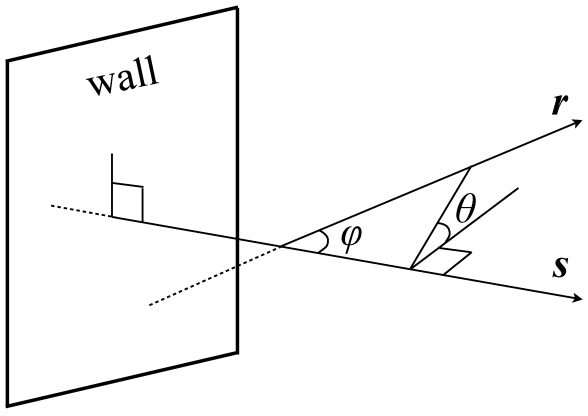

Fig. 2.3 Coordinate system for tangent-slab approximation.

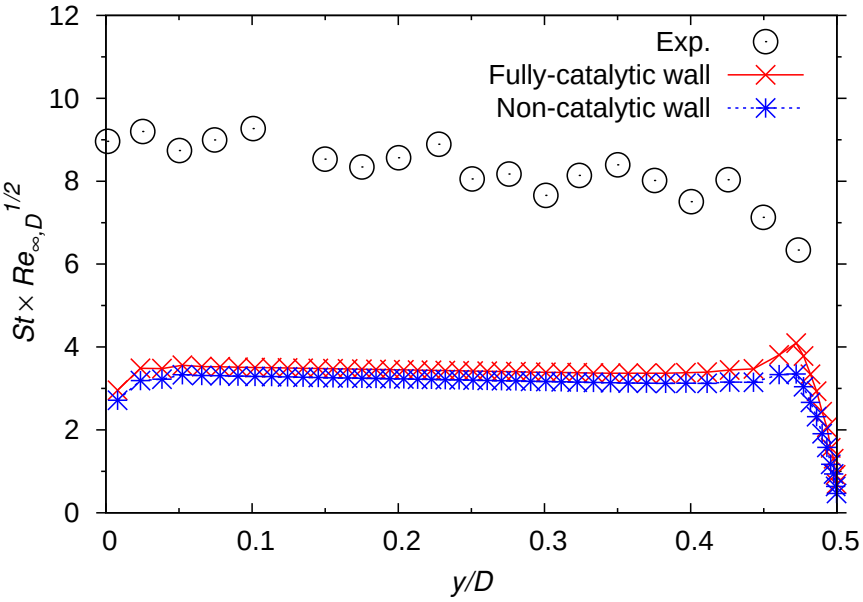

Fig. 2.4 Dependence of surface catalysis on convective heat flux.

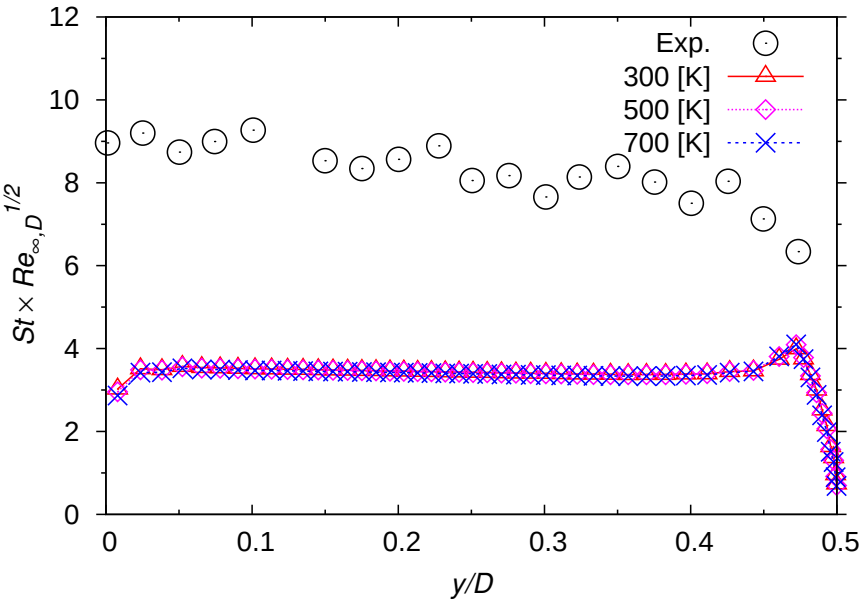

Fig. 2.5 Dependence of wall temperature on convective heat flux.

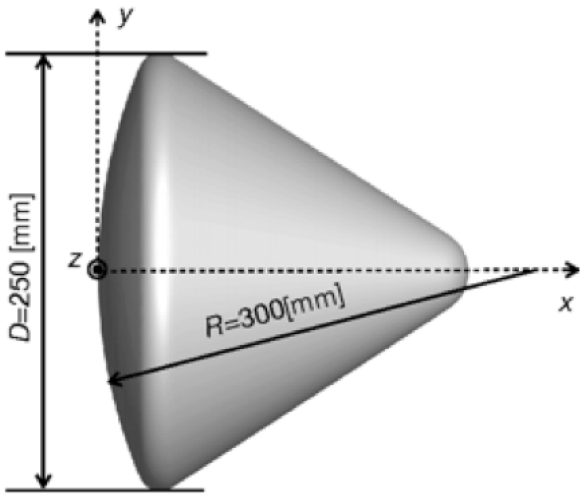

(a) Apollo CM 6.4% scaled model

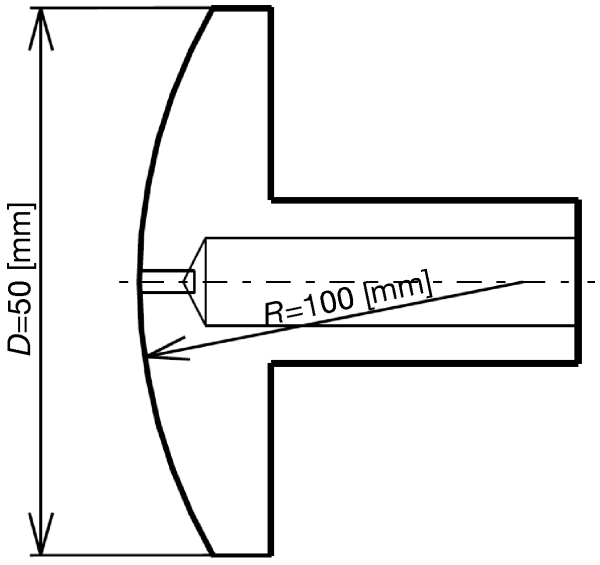

(b) D50R100 probe model

Fig. 2.6 Test models employed in the HIEST experiments.

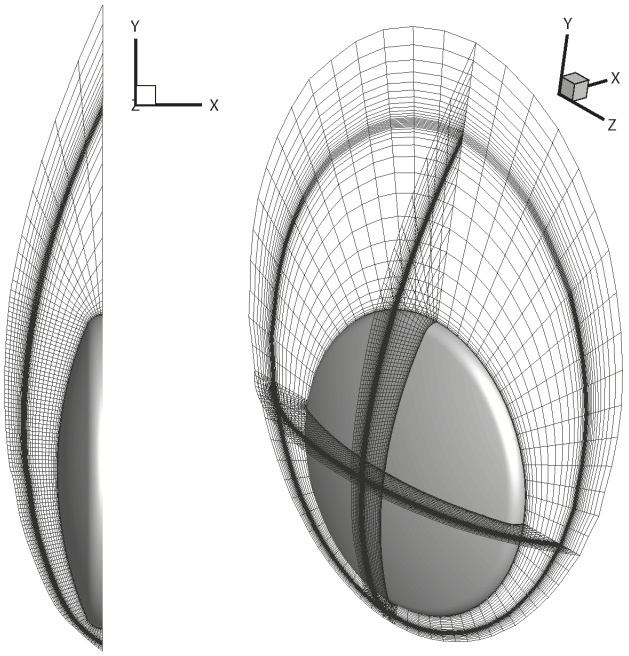

Fig. 2.7 Solution adaptive mesh for the Apollo CM test model at an AoA 30 deg.

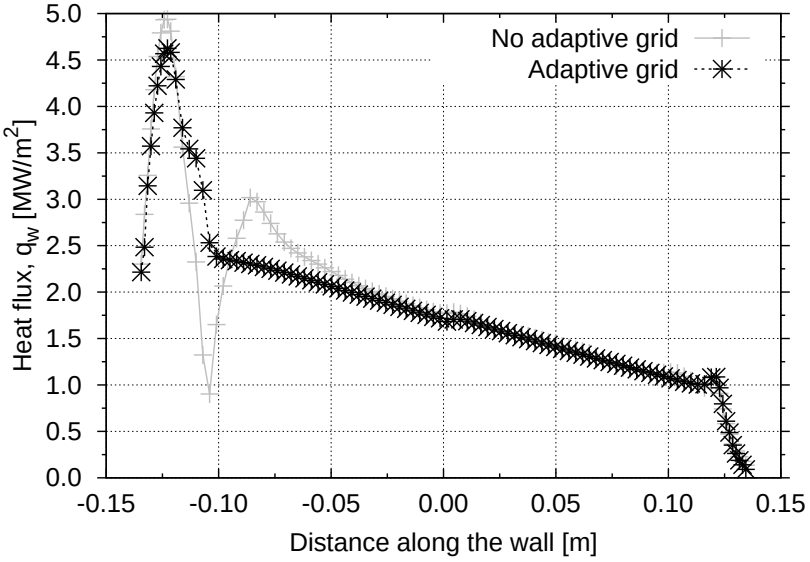

Fig. 2.8 Heat flux distribution using solution adaptive grid and no adaptive grid.

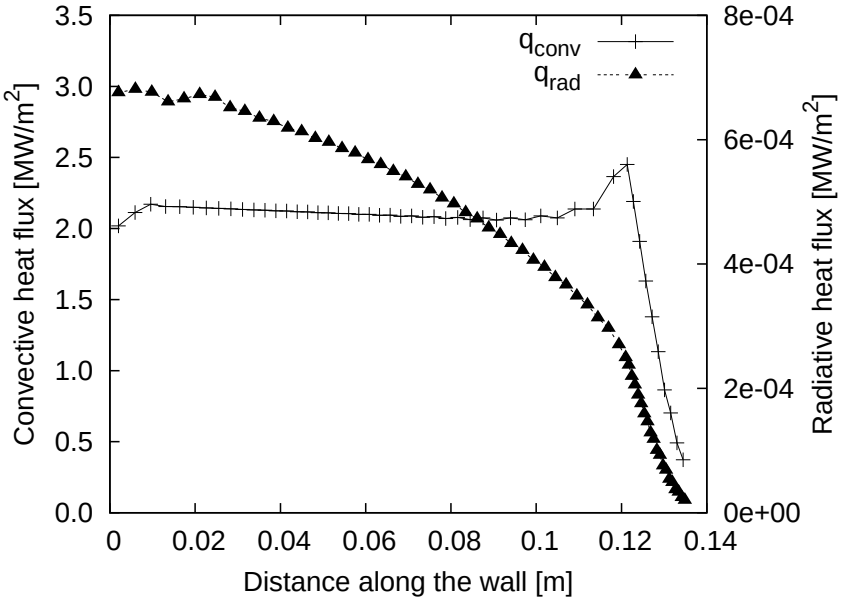

(a) Shot No. 1781 (H_0=6.849 MJ/kg)

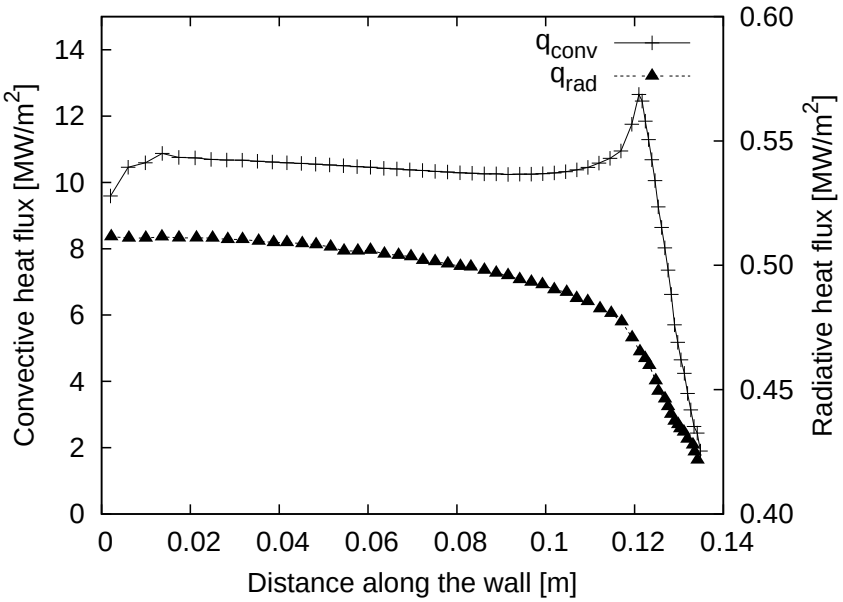

(b) Shot No. 1783 (H_0=21.537 MJ/kg)

Fig. 2.9 Radiation heat flux from air species with computed convective heat flux.

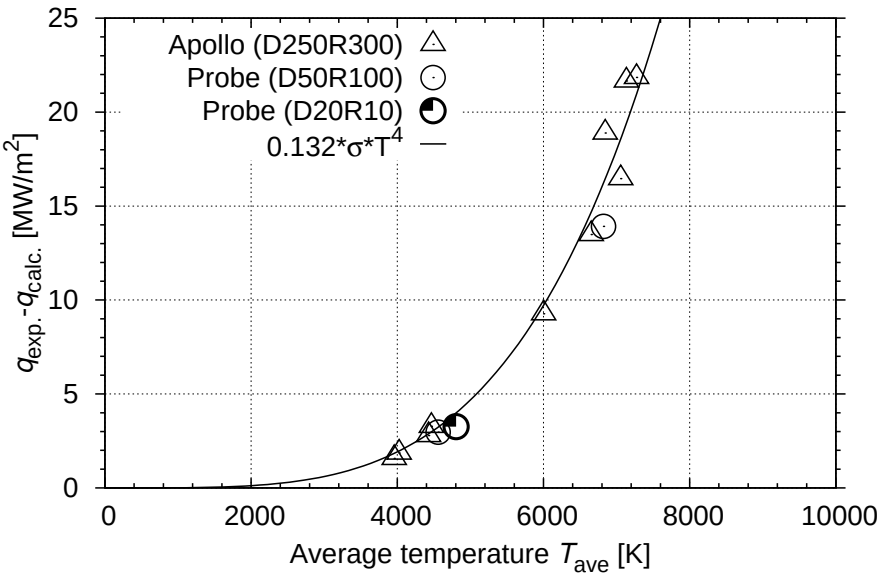

(a) ϵ is 0.132 when the data is reduced by the average temperature $T_{v\mathrm{ave}}$

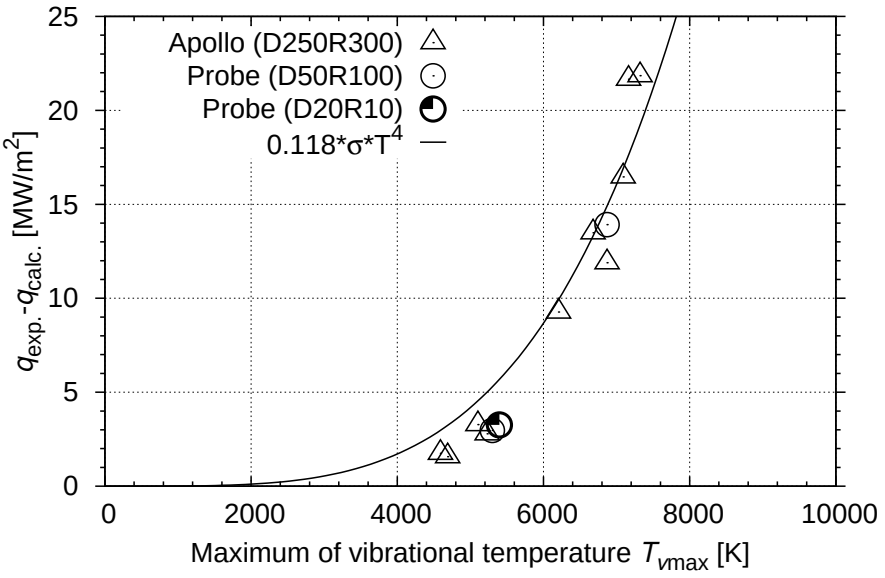

(b) ϵ is 0.118 when the data is reduced by the maximum vibrational temperature $T_{v\mathrm{max}}$

Fig. 2.10 Abnormal heat flux augmentations at the stagnation point of several blunt bodies with a fitted curve of the Stefan-Boltzmann law.

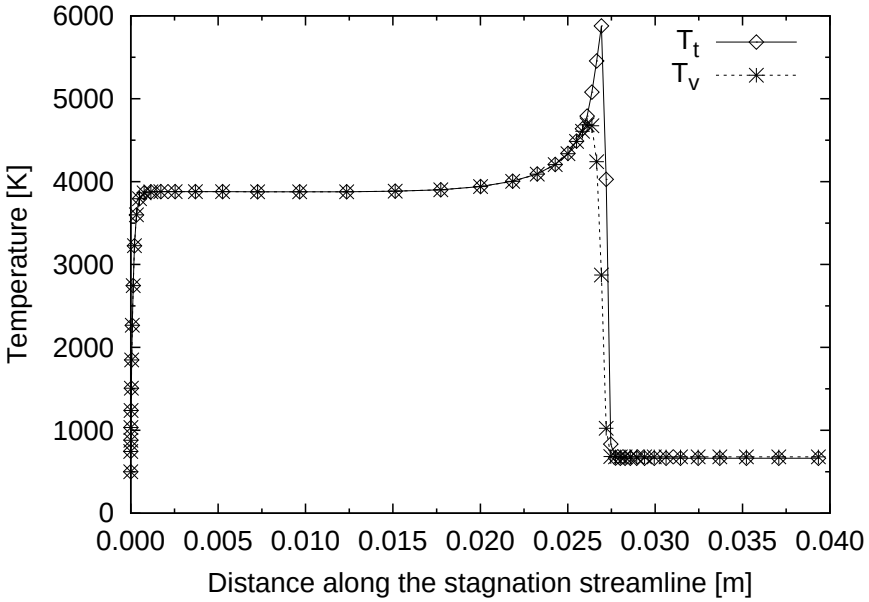

(a) Shot No. 1781 (H_0=6.849 MJ/kg)

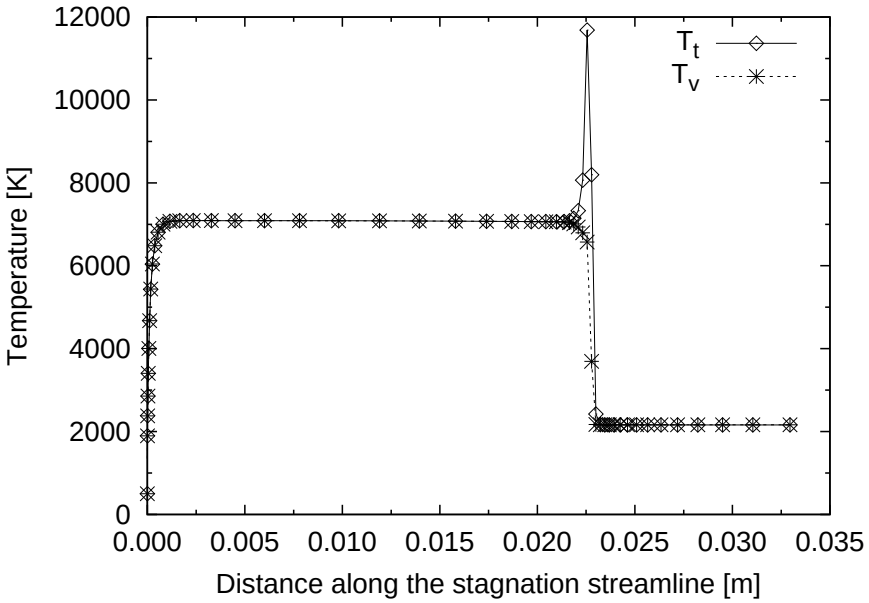

(b) Shot No. 1783 (H_0=21.537 MJ/kg)

Fig. 2.11 Translational temperature and vibrational temperature profiles along the stagnation streamline.

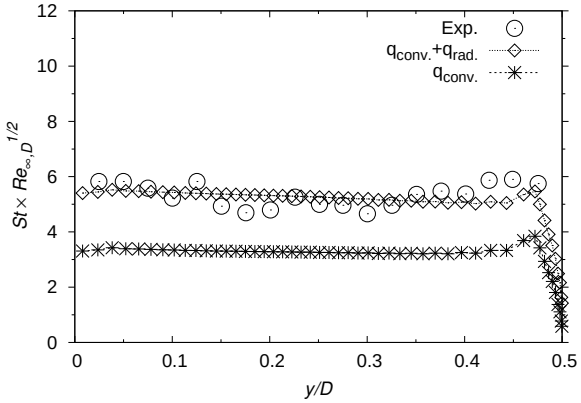

(a) Shot No. 1781 (H_0=6.849 MJ/kg)

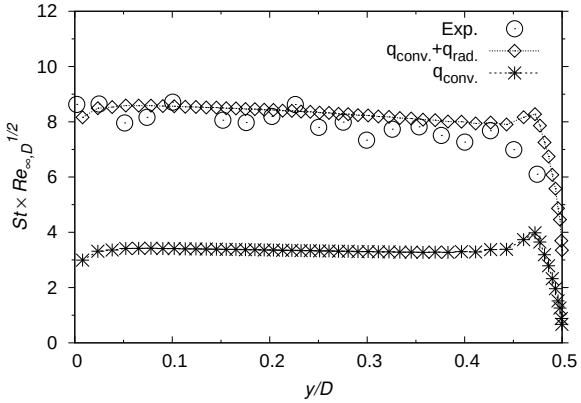

(b) Shot No. 1782 (H_0=17.275 MJ/kg)

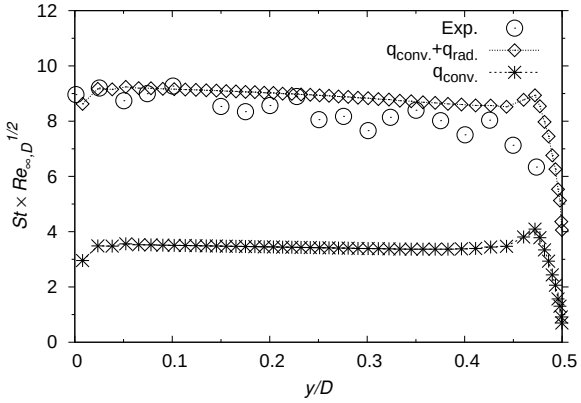

(c) Shot No. 1783 (H_0=21.537 MJ/kg)

Fig. 2.12 Convective heat flux profiles, total heat flux profiles and corresponding measured data are plotted for the Apollo CM test model at an AoA of 0 deg., where emissivity is $\epsilon = 0.132$.

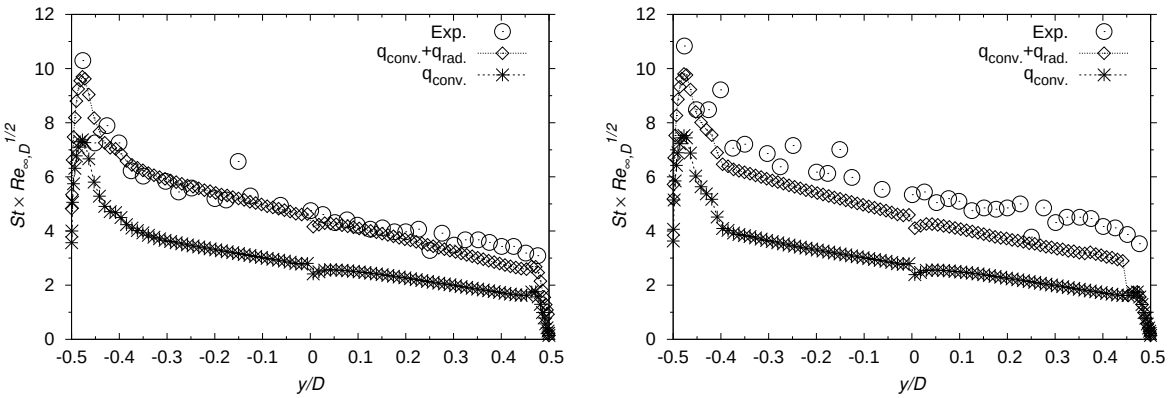

(a) Shot No. 1791 (H_0=6.759 MJ/kg)

(b) Shot No. 1787 (H_0=8.094 MJ/kg)

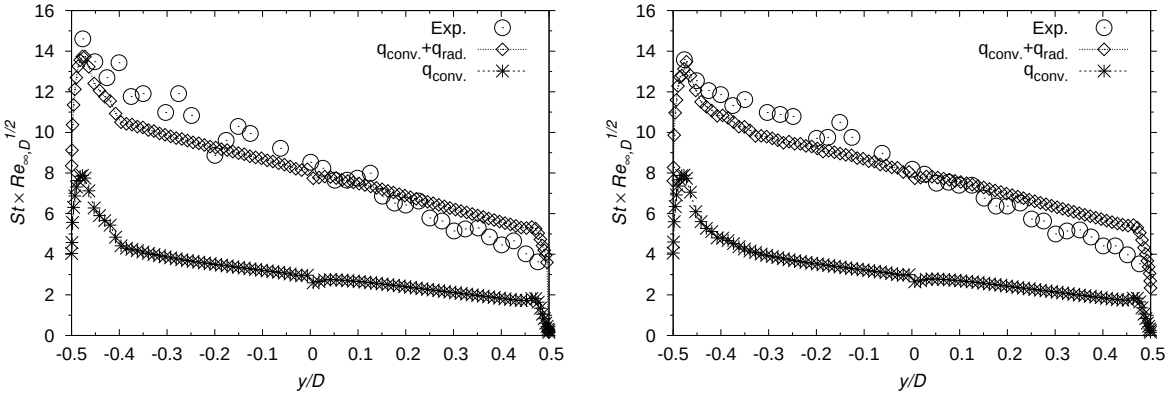

(c) Shot No. 1784 (H_0=19.554 MJ/kg)

(d) Shot No. 1785 (H_0=21.059 MJ/kg)

Fig. 2.13 Convective heat flux profiles, total heat flux profiles and corresponding experimental heat flux data are plotted for the Apollo CM test model at an AoA of 0 deg. The emissivity is $\epsilon = 0.132$.

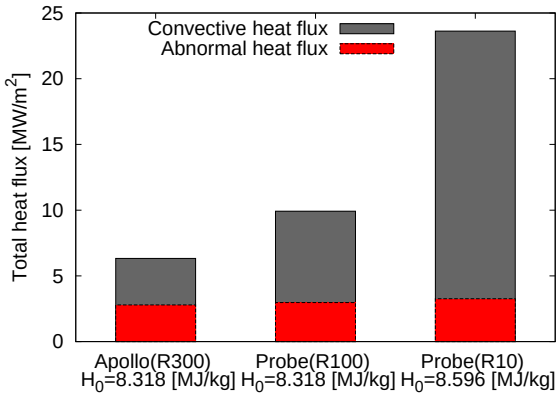

(a) Lower enthalpy conditions

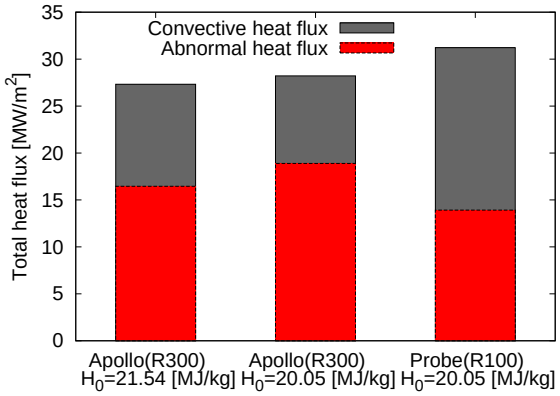

(b) Higher enthalpy conditions

Fig. 2.14 Ratio of the measured heat flux in HIEST experiment and the convective heat flux obtained by CFD at the stagnation point for various models.

Bibliography

[1] Tanno, H., Komuro, T., Sato, K., Itoh, K., Takahashi, M., Ishihara, T., Ogino, Y., and Sawada K., "Experimental Study on Heat Flux Augmentation in High Enthalpy Shock Tunnels," AIAA Paper 2014-2548, 2014.

[2] Park, C., *Nonequilibrium Hypersonic Aerothermodynaics*, John Wiley and Sons, Inc., 1989.

[3] Blottner, F. G., Johnson M., and Elis, M., "Chemically Reacting Viscous Flow Program for Multi-Component Gas Mixture," Sandia Laboratories, SC-RR-70-754, 1971.

[4] Vincenti, W. G. and Kruger, C. H., *Introduction to Physical Gas Dynamics*, John Wiley and Sons, Inc., 1967.

[5] Wilke, C. R., "A Viscosity Equation for Gas Mixtures," *Journal of Chemical Physics*, Vol. 18, No. 4, 1950, pp. 517–519.

[6] Park, C., "Review of Chemical-Kinetic Problems of Future NASA Mission, I:Earth Entries," *Journal of Thermophysics and Heat Transfer*, Vol. 7, No. 3, 1993, pp. 385–298.

[7] Bose, D., and Candler, G. V., "Thermal Rate Constants of the $O_2 \leftrightarrow N+NO+O$ Reaction Using ab initio ^2A" and ^4A' Potential Energy Surfaces," *Journal of Chemical Physics*, Vol. 107, No. 16, 1997, pp. 6136–6145.

[8] Park, C., Jaff, L., R., and Partridge, H., "Thermal Rate Constants of the $O_2 \leftrightarrow N+NO+O$ Reaction Using ab initio ^2A" and ^4A' Potential Energy Surfaces," AIAA 2000-0210, 2000.

[9] Millikan, R. C. and White, D. R., "Systematics of Vibrational Relaxation," *Journal of Chemical Physics*, Vol. 39, No. 12, 1963, pp. 3209–3213.

[10] Shima, E. and Kitamura, K., "Parameter-Free Simple Low-Dissipation AUSM-Family Scheme for All Speeds," *AIAA Journal*, Vol. 49, No. 8, 2011, pp. 1639–1709.

[11] Kitamura, K., Shima, E., Nakamura, Y., and Roe. P. L., "Evalution of Euler Fluxes for Hypersonic Heating Computations AUSM-Family Schemes for Hypersonic Heating Computations," *AIAA Journal*, Vol. 48, No. 4, 2010, pp. 763–776.

[12] Van Leer, B., "Towards the Ultimate Conservation Difference Scheme V. A Second-Order Sequel to Godunov's Method," *Journal of Computational Physics*, Vol. 23, No. 3, 1979, pp. 101–136.

[13] Yoon, S. and Jameson. A., "An Lu-ssor Scheme for the Euler and Navier-Stokes Equations," AIAA Paper 87-600, 1987.

[14] Eberhart, S. and Imalay, S., "Diagonal Implicit Scheme for Computing Flows with Finite Rate Chemistry," *Journal of Thermophysics and Heat Transfer*, Vol. 6, No. 3, 1992, pp. 208–216.

[15] Vincenti, W. G. and Kruger, C. H., *Introduction of Physical Gas Dynamics*, John Wiley and Sons, Inc., 1967.

[16] Park, C. and Milos, F. S., "Computational Equations for Radiating and Ablating Shock Layers," AIAA Paper 90-0356, 1990.

[17] Tanno, H., Kodera, M., Komuro, T., Sato, K., Takahashi, M., and Itoh, K., "Aeroheating Measurements on a Reentry Capsule Model in Free-Piston Shock Tunnel HIEST," AIAA paper 2010-1181, 2010.

[18] Takahashi, M., Kodera, M., Itoh, K., Komuro, T., Sato, K., and Tanno, H., "Influence of Thermal Non-equilibrium on Nozzle Flow Condition of High Enthalpy Shock Tunnel HIEST," AIAA Paper 2009-7267, 2009.

[19] Tanno, H., Komuro, T., Sato, K., Itoh, K., Yamada, T., Sato, N., and Nakano, E., "Heat Flux Anomaly in High-enthalpy and High Reynolds Number Flow," AIAA Paper 2012-3104, 2012.

[20] Candler, G. V. and Nompelis, I., "Computational Fluid Dynamics for Atomospheric Entry," *Von Karman Institute for Fluid Dynamics Lecture Series*, Vol. 6, No. RTO-EN-AVT-162, 1992, pp. 15/1–15/56.

Chapter 3

Numerical Study on Wall Pressure over Cone Region of Blunt-nosed Body

3.1 Introduction

Figure 3.1 shows the measured pressure distributions in the conical region of the test model with the results computed by the thermochemical non-equilibrium CFD code. The test model is a 15-deg sphere-cone model with a nose radius of 50 mm as shown in Fig. 3.2. In the measurements, four different stagnation enthalpies ($H_0 = 3.8, 8.0, 10.1$ and 15.6 MJ/kg) were chosen. The upstream conditions summarized in Table 3.1 are determined by JAXA in-house axi-symmetric nozzle code[1] which computes the thermochemical nonequilibrium flowfield in between the downstream side of the second diaphragm and exit plane of the nozzle as indicated in Fig. 3.3. At low enthalpy conditions such as $H_0 = 3.8$ and 8.0 MJ/kg, good agreements are obtained. On the other hand, at high enthalpy conditions such as $H_0 = 10.1$ and 15.6 MJ/kg, the calculated pressure values are higher than those experimental results.

As the cause of the discrepancy, we first focus on the upstream conditions. Characterization of flow variables at the nozzle exit of HIEST is carried out by the JAXA in-house nozzle code which solves the flowfield inside the nozzle region. This in-house code employs the stagnation condition at the second diaphragm as the upstream boundary condition. The stagnation condition is determined by the thermochemical equilibrium calculation using the measured stagnation pressure and the speed of in-

cident shock wave at the second diaphragm. This nozzle code has been used for wide range of operating conditions and been believed to yield reliable upstream conditions. However, validation of the nozzle code for all the operating conditions is difficult to be accomplished because of the lack of experimental data. In this study, therefore, we attempt to vary the upstream flow conditions to find which flow variable has a high sensitivity on the computed surface pressure distribution over the blunt test model. Then we determine the amount of change required to reproduce the surface pressure distribution and examine whether such change is really likely to occur or not.

Second, we focus on thermochemical model in the supersonic expansion. We examine the relaxation time between translational and vibrational modes, and also the chemical reaction rates in the supersonic expanding region employed in the CFD code. In the present CFD calculation, we choose the Park's two-temperature nonequilibrium thermochemical model.[2, 3] This model employs the Arrhenius form to describe forward chemical reaction rates and the Millikan-White translational-vibrational relaxation time.[4] The parameters of these models were calibrated using the experimental data obtained behind normal shocks in shock tube where strong compression occurs. In the calculation of pressure distribution over a space capsule at lifting entry, thermochemical nonequilibrium models need to work well also in the expanding region. In the present study, we attempt to clarify the possible influence of these parameters on the surface pressure in expanding region.

Our objective of this study, therefore, is to clarify the cause of the observed discrepancy in the wall pressure distribution between the experimental data and the calculated results at high enthalpy conditions. We first check the sensitivity of upstream flow variables at the nozzle exit. In particular, we focus on to examine the upstream translational temperature and also on the composition of chemical species at the nozzle exit. In the sensitivity check of the upstream chemical composition we employ the methods of uncertainty quantification (UQ)[5, 6]. We then evaluate the amount of change of the upstream variable which is required to reproduce the surface pressure distribution and investigate what physical process is responsible for the

change and confirm whether such change is really likely to occur. A consistency check is carried out by computing the flowfield in the nozzle region including the identified physical process to obtain the flow variables at the nozzle exit. Those modified flow variables are the employed as the freestream boundary condition for computing the flowfield in the test section. The consistency is finally confirmed when the computed surface pressure distribution agrees with that given in the experimental data. Next, as to the parameters in the physical model such as the translational-vibrational relaxation time and chemical reaction rates, we also employ UQ to examine the sensitivity of these model parameters to see which parameter has high sensitivity and examine whether change of the parameter would have significant influence over the computed surface pressure distribution.

In section 2, numerical methods are described including the method of UQ employed in this study. Then in section 3, flow conditions are given. In section 4, the computed results are shown and the related discussions are given. Finally in section 5, the conclusions of the present study are stated.

3.2 Numerical Methods

3.2.1 Flowfield calculation

Governing equations

The governing equations for the flow field calculation are the Reynolds averaged axisymmetric Navier-Stokes equations accounting for thermochemical non-equilibrium. The Spalart-Allmaras (SA) turbulence model[7] is employed.

$$\frac{\partial \boldsymbol{Q}}{\partial t} + \frac{\partial (\boldsymbol{F} - \boldsymbol{F}_{\mathrm{vis}})}{\partial x} + \frac{\partial (\boldsymbol{G} - \boldsymbol{G}_{\mathrm{vis}})}{\partial y} + \frac{1}{y}(\boldsymbol{H} - \boldsymbol{H}_{\mathrm{vis}}) = \boldsymbol{W}. \tag{3.1}$$

Components of the conservative variables $\boldsymbol{Q}$, the convective flux vector $\boldsymbol{F}$, $\boldsymbol{G}$, the viscous vector $\boldsymbol{F}_{\mathrm{vis}}$, $\boldsymbol{G}_{\mathrm{vis}}$, axisymmetirc term $\boldsymbol{H}$ and $\boldsymbol{H}_{\mathrm{vis}}$ are given by:

$$\boldsymbol{Q} = \begin{pmatrix} \rho \\ \rho u \\ \rho v \\ E \\ \rho_s \\ E_v + E_e \\ \rho\tilde{\nu} \end{pmatrix}, \tag{3.2}$$

$$\boldsymbol{F} = \begin{pmatrix} \rho u \\ \rho u^2 + p \\ \rho uv \\ (E+p)u \\ \rho_s u \\ (E_v + E_e)u \\ \rho u\tilde{\nu} \end{pmatrix}, \boldsymbol{G} = \begin{pmatrix} \rho v \\ \rho uv \\ \rho v^2 + p \\ (E+p)v \\ \rho_s v \\ (E_v + E_e)v \\ \rho v\tilde{\nu} \end{pmatrix}, \tag{3.3}$$

$$\boldsymbol{F}_v = \begin{pmatrix} 0 \\ \tau_{xx} \\ \tau_{xy} \\ F_{v,4} \\ -\rho_s u_s \\ F_{v,8} \\ 0 \end{pmatrix}, \boldsymbol{G}_v = \begin{pmatrix} 0 \\ \tau_{yx} \\ \tau_{yy} \\ G_{v,4} \\ -\rho_s v_s \\ G_{v,8} \\ 0 \end{pmatrix}, \tag{3.4}$$

$$\boldsymbol{H} = \begin{pmatrix} \rho v \\ \rho uv \\ \rho v^2 \\ (E+p)v \\ \rho_s v \\ (E_v + E_e)v \\ \rho v\tilde{n}u \end{pmatrix}, \boldsymbol{H}_v = \begin{pmatrix} -\rho_s v_s \\ \tau_{xy} \\ \tau_{yy} - \tau_{\theta\theta} \\ H_{v,4} \\ -\rho_s v_s \\ H_{v,8} \\ 0 \end{pmatrix}, \tag{3.5}$$

$$\boldsymbol{W} = \begin{pmatrix} 0 \\ 0 \\ 0 \\ 0 \\ \dot{W}_s \\ \dot{W}_v \\ \dot{W}_{SA} \end{pmatrix}, \tag{3.6}$$

where the component of viscous flux vector of total energy, $F_{v,4}$, $G_{v,4}$ and $H_{v,4}$, and the components of viscous flux vector of vibrational energy, $F_{v,8}$, $G_{v,8}$ and $H_{v,8}$ are given by

$$F_{v,4} = u\tau_{xx} + v\tau_{xy} - q_{tx} - q_{vx} - \sum_s \rho_s u_s h_s, \tag{3.7}$$

$$G_{v,4} = u\tau_{yx} + v\tau_{yy} - q_{ty} - q_{vy} - \sum_s \rho_s v_s h_s, \tag{3.8}$$

$$H_{v,4} = u\tau_{xy} + v\tau_{yy} - q_{ty} - q_{vy} - \sum_s \rho_s v_s h_s, \tag{3.9}$$

$$F_{v,8} = -q_{vx} - \sum_s \rho_s u_s ev_s, \tag{3.10}$$

$$G_{v,8} = -q_{vy} - \sum_s \rho_s v_s ev_s, \tag{3.11}$$

$$H_{v,8} = -q_{vy} - \sum_s \rho_s v_s ev_s. \tag{3.12}$$

The shear stress τ is given by

$$\tau_{xx} = \frac{2}{3}\mu(2\frac{\partial u}{\partial x} - \frac{\partial v}{\partial y} - \frac{v}{y}), \tag{3.13}$$

$$\tau_{xy} = \mu(\frac{\partial u}{\partial y} + \frac{\partial v}{\partial x}), \tag{3.14}$$

$$\tau_{yy} = \frac{2}{3}\mu(2\frac{\partial v}{\partial y} - \frac{\partial u}{\partial x} - 2\frac{v}{y}), \tag{3.15}$$

$$\tau_{\theta\theta} = \frac{2}{3}\mu(\frac{\partial v}{\partial y} - \frac{\partial u}{\partial x} + 2\frac{v}{y}). \tag{3.16}$$

The source term of chemical reaction and vibrational energy, $\dot{W}_s$ and $\dot{W}_v$ are given by the section 2.2.2. The source term of SA is given by

$$\begin{aligned}\dot{W}_{SA} =& \rho C_{b1}\left(1 - f_{t2}\right)\tilde{S}\tilde{\nu} + \frac{\rho}{\sigma}\left[\nabla\cdot\left\{\left(\nu+\tilde{\nu}\right)\nabla\tilde{\nu}\right\} + c_{b2}\left(\nabla\tilde{\nu}\right)^2 + \frac{1}{y}\left(\nu+\tilde{\nu}\right)\frac{\partial\tilde{\nu}}{\partial y}\right] \\ &+\rho\left(c_{w1}f_w - \frac{C_{b1}}{\kappa^2}f_{t2}\right)\left(\frac{\tilde{\nu}}{d}\right).\end{aligned} \tag{3.17}$$

The turbulent eddy viscosity is computed from

$$\mu_t = \rho\tilde{\nu} f_{v1}, \tag{3.18}$$

$$f_{v1} = \frac{\chi^3}{\chi^3 + c_{v1}^3}, \tag{3.19}$$

$$\chi = \frac{\tilde{\nu}}{\nu}, \tag{3.20}$$

where $\nu = \mu/\rho$ is the molecular kinematic viscosity, and μ is the molecular dynamic viscosity. Additional definitions are given as follows:

$$\tilde{S} = \Omega + \frac{\tilde{\nu}}{\kappa^2 d^2} f_{v2}, \tag{3.21}$$

$$\Omega = \left| \frac{\partial v}{\partial x} - \frac{\partial u}{\partial y} \right|, \tag{3.22}$$

$$f_{v2} = 1 - \frac{\chi}{1 + \chi f_{v1}}, \tag{3.23}$$

$$f_w = g\left(\frac{1 + c_{w3}^6}{g^6 + c_{w3}^6} \right), \tag{3.24}$$

$$g = r + c_{w2}(r^6 - r) \tag{3.25}$$

$$r = \min\left(\frac{\nu}{\tilde{S}\kappa^2 d^2}, 10 \right), \tag{3.26}$$

$$f_{t2} = c_{t3} \exp(-c_{t4}\chi^2), \tag{3.27}$$

where constants are

$$c_{b1} = 0.1355, \quad \sigma = 2/3, \quad c_{b2} = 0.622, \quad \kappa = 0.41, \quad c_{w2} = 0.3, \quad c_{w3} = 2 \tag{3.28}$$
$$c_{v1} = 7.1, \quad c_{t3} = 1.2, \quad c_{t4} = 0.5, \quad c_{w1} = \frac{c_{b1}}{\kappa^2} + \frac{1 + c_{b2}}{\sigma}.$$

Thermochemical model and transport coefficients

We employ the Park's two-temperature thermochemical model which is same as the section 2. Five neutral air species (O, N, NO N_2 and O_2) and 17 chemical reactions for air are considered. For the transport coefficients, the collision integrals are used to determine all transport properties: viscosity, thermal conductivity, and diffusion. For the (1,1) and (2,2) integrals, the Gupta curve fit relation[8] is used. The numerical method is based on the cell-centered finite volume scheme. The convective numerical

flux is calculated by SLAU scheme[9, 10]. The viscous flux is evaluated by a central difference scheme. We employ the MUSCL approach[11] to attain the second order spatial accuracy. In the time integration, the Euler explicit method is employed. The diagonal point implicit method is utilized in order to improve the stability in the integration of the source terms[12].

3.2.2 Uncertainty quantification and analysis of variance

For the uncertainty quantification, we use Point-collocation non-intrusive polynomial chaos method (PC)[6, 13]. In this method, uncertain variables (x, ξ) such as aerodynamic characteristics, heat flux and etc. are decomposed into separable deterministic and stochastic components based on spectral representations as follows:

$$R(\boldsymbol{x}, \boldsymbol{\xi}) \equiv \Sigma_{j=0}^{P} \alpha_j(\boldsymbol{x}) \Psi_j(\boldsymbol{\xi}), \tag{3.29}$$

where $\alpha_j(\boldsymbol{x})$ is the deterministic component and $\Psi_j(\boldsymbol{\xi})$ is the random basis function corresponding to the j-th mode. We assume $R(\boldsymbol{x}, \boldsymbol{\xi})$ to be a function of deterministic independent variable vector $\boldsymbol{x}$ and the $n-$dimensional random variable vector $\boldsymbol{\xi} = (\xi_1, ..., \xi_n)$. In Eq. 3.29, the total number of terms $P + 1$ is given by

$$P + 1 = \frac{(n + p)!}{n!p!}, \tag{3.30}$$

where p is the highest order of random basic function Ψ and n is the number of element for input random variable vector $\boldsymbol{\xi}$. The basis function Ψ depends on the distribution of the input random variables. We use multi-dimensional Legendre which is optimal basis functions for uniform. The detailed process of the way that derives the multi-dimensional basis function is described by Eldred et al[5].

In this study, non-intrusive polynomial chaos (NIPC) approach is used, because this approach can treat a deterministic code as "black box", and we do not need to rewrite a flowfield solver. The point collocation NIPC method evaluates their polynomial expansions given by Eq. 3.29 with $P + 1$ random vectors. The $P + 1$ random vectors $\boldsymbol{\xi}_j = (\xi_1, ..., \xi_n)_j (j = 0, 1, ..., P)$ are chosen for a given PC expansion with $P + 1$

modes, and the deterministic code is calculated at each random vector. Then we can obtain the left hand side of Eq. 3.29, and a linear system of the uncertainty equations to be solved can be represented by

$$\begin{bmatrix} R(x,\xi_0) \\ R(x,\xi_1) \\ \vdots \\ R(x,\xi_P) \end{bmatrix} = \begin{bmatrix} \Psi_0(\xi_0) & \Psi_1(\xi_0) & \cdots & \Psi_P(\xi_0) \\ \Psi_0(\xi_1) & \Psi_1(\xi_1) & \cdots & \Psi_P(\xi_1) \\ \vdots & \vdots & \ddots & \vdots \\ \Psi_0(\xi_P) & \Psi_1(\xi_P) & \cdots & \Psi_P(\xi_P) \end{bmatrix} = \begin{bmatrix} \alpha_0(x) \\ \alpha_1(x) \\ \vdots \\ \alpha_P(x) \end{bmatrix}. \tag{3.31}$$

The PC coefficients α_j are obtained by solving the linear system given by Eq. (3.31). The solution of the linear system of Eq. (3.31) requires evaluations for $P+1$ deterministic functions. If the number of samples is greater than $P+1$, we can solve the over-determined system of the equations using the least squares method. After we obtain α_j, the mean value μ_R and the standard deviation σ_R^2 are given by

$$\mu_R = \alpha_0, \tag{3.32}$$

$$\sigma_R^2 = \Sigma_{j=1}^{P} \alpha_j^2 < \Psi_j^2(\boldsymbol{\xi}) >, \tag{3.33}$$

where $< \Psi_j^2(\boldsymbol{\xi}) >$ can be calculated analytically[13].

In sensitivity check, we use Sobol's indices[14] which is defined by the ratio of the partial variance and the standard deviation as

$$S_i = \frac{D_i}{\sigma_R^2}. \tag{3.34}$$

The larger S_i means the higher sensitivity of ξ_i. The partial variance D_i is given by

$$D_i = \Sigma_k \alpha_k^2 < \Psi_k^2(\xi_i) >, \tag{3.35}$$

where k indicates the set in which Ψ is a function of only ξ_i.

Figure 3.4 shows the computational procedure in this study. First, we set input random number $\boldsymbol{\xi} = (\xi_1, ..., \xi_n)$ such as the chemical reaction rates and the chemical compositions in the upstream. Second, flowfield calculation in each $\boldsymbol{\xi} = (\xi_1, ..., \xi_n)$ is conducted until the steady solution is obtained. Since the flowfield calculations are needed as many as the number of element for ξ, we use the Open MPI parallelization. Third, the wall pressure in each ξ given by the flowfield calculation is set

as the uncertainty variables $R(\boldsymbol{x}, \boldsymbol{\xi})$, and $\alpha_j(\boldsymbol{x})$ is determined by Eq. (3.31). Then we can obtain the mean value and the standard deviation by Eq. (3.32) and (3.33), respectively. Finally, we can get Sobol's indices by Eq. (3.34) and (3.35).

3.3 Numerical Conditions

3.3.1 Flowfield calculation

The upstream flow conditions for the baseline calculations are taken from those shown in Table 3.1 for the upstream enthalpies of $H_0 = 15.6$ and 10.1 MJ/kg. An isothermal and fully-catalytic wall is assumed for the wall boundary conditions. The wall temperature is set to be 300 K. A typical example of computational grid is shown in Fig. 3.5. It is a structured mesh having 71 points in the normal direction from the surface toward the outer boundary and 101 points along the surface. The minimum grid spacing is determined by the grid convergence study. One can find that several mesh lines are clustered using the solution adaptive technique to represent shock wave sharply, which is critically important to obtain a smooth flowfield in the shock layer[15].

3.3.2 Uncertainty quantification and analysis of variance

For UQ of the translational-vibrational relaxation time, we vary the relaxation time from 0.01 to 100 times of the original Millikan-White relaxation time. We note that the Park's collision limiting time is negligibly short compared to the Millikan-White relaxation time because the translational-rotational temperature is at most 10,000 K even for the highest enthalpy condition of $H_0 = 15.6$ MJ/kg. For UQ of the chemical reaction rates, we vary the forward reaction rates of all 17 chemical reactions from 0.01 to 100 times of the original forward reaction rates shown in Table 2.7 in the region enclosed by a bold line in Fig. 3.5 where supersonic expanding flow appears. Then the backward reaction rates are determined by using Eq. 2.56.

For UQ of freestream chemical compositions, we vary the mole numbers of O, NO,

O_2, N_2 shown in Table 3.1 within the range of ±3% while the upstream velocity and temperature are kept unchanged. Note that the mole number of N in the upstream is kept constant because it is negligibly small even at $H_0 = 15.6$ MJ/kg. On the other hand, influence of the freestream values such as the translational temperature and vibrational temperature on the surface pressure distribution are separately examined without relying on UQ.

3.4 Results and Discussion

3.4.1 Influence of freestream conditions

In Fig. 3.6, the computed wall pressure distributions are plotted for the stagnation enthalpy of $H_0 = 15.6$ MJ/kg when the freestream translational temperature and vibrational temperature are varied. One can find that the vibrational temperature has a minor effect on the surface pressure distribution, while the translational temperature has significant effect. Reasonable agreements are obtained when the freestream translational temperature is reduced by 100 to 300 K. The computed pressure distributions for the stagnation enthalpy of $H_0 = 10.1$ MJ/kg also indicate the similar trends as shown in Fig. 3.7. In Fig. 3.8, the difference in pressure distributions is plotted for the case of the stagnation enthalpy of $H_0 = 15.6$ MJ/kg, when the freestream translational temperature is reduced by 300 K. It can be seen that the pressure decreases more in the conical region than that near the stagnation region.

Figure 3.9 shows the computed sensitivity on the wall pressure when the mass fractions of freestream chemical species are varied within 3%. Obviously, O_2 and O have high sensitivities in the conical region, while NO and N have little sensitivities there. Based on this observation, we then vary the mass fractions of O_2 and O in the freestream conditions computed by JAXA in-house code for the stagnation enthalpies of 15.6 MJ/kg and 10.1 MJ/kg, and see how the pressure distribution along the surface of test model changes. Table 3.2 summarizes the mass fractions for the five cases (Case A, B, C, D and baseline) for the stagnation enthalpy of $H_0 = 15.6$ MJ/kg,

and Table 3.3 for the three cases (Case E, F and baseline) for the stagnation enthalpy of $H_0 = 15.6$ MJ/kg, and Table 3.3 for the three cases (Case E, F and baseline) for the stagnation enthalpy of $H_0 = 10.1$ MJ/kg. These baseline conditions are listed in Table 3.1. The computed surface pressure distributions for $H_0 = 15.6$ MJ/kg are plotted in Fig. 3.10. When the mass fraction of O_2 is gradually increased from that of the baseline case, the surface pressure becomes lower than that of the baseline case. A good agreement is obtained in Case B. On the other hand, the computed surface pressure distributions for $H_0 = 10.1$ MJ/kg plotted in Fig. 3.11 do not give good agreements with the experimental data, though the surface pressure decreases at the mass fraction of O_2 is increased. Therefore, it seems difficult to fully explain the observed discrepancy in surface pressure distributions solely by the uncertainties in the freestream chemical composition.

3.4.2 Influence of translational-vibrational relaxation time and chemical reaction rates in supersonic expansion region

Figure 3.12 shows the mean values of the computed pressure distribution along the model surface with the standard deviations when the translational-vibrational relaxation times are varied from 0.01 to 100 times of the original values for the stagnation enthalpy of $H_0 = 15.6$ MJ/kg. One can find that the standard deviations are so small that the relaxation time has less effect on the wall pressure. Therefore, the measured discrepancies seem not likely to be explained by uncertainties in the relaxation time.

Figure 3.13 shows the mean value and the standard deviation when 0.1-10 times forward reaction rates. The standard deviation is large in $x = 0 - 0.05$ m and $x = 0.12 - 0.18$ m. The sensitivity of reaction 1 ($O_2 + O \rightleftharpoons O + O + O$), reaction 5 ($O_2 + N_2 \rightleftharpoons O + O + N_2$) and reaction 11 ($NO + O \rightleftharpoons N + O + O$) on the surface pressure distributions are shown in Fig. 3.14 for the stagnation enthalpy of $H_0 = 15.6$ MJ/kg. Though not shown, the sensitivities of other reaction rates are negligible. One can find that the sensitivity of reaction 1 and 5 are high in x=0-0.05 m and x=0.12-0.18 m where the standard deviation is large. Figure 3.15 shows the obtained surface

pressure distribution for the stagnation enthalpy of $H_0 = 15.6$ MJ/kg in which the forward reaction rates for reactions 1 and 5 are varied from 0.01 to 100 times of the original values. One can find that the forward reaction rates to be 0.01 times of the original reaction rates give minor influence on the pressure distributions. On the other hand, when 100 times larger forward reaction rates are employed, the surface pressure in the down stream region increases to further depart from the experimental data. Therefore, the observed discrepancy in the surface pressure distribution seems not likely to be explained by uncertainties in the chemical reaction rates employed in the thermochemical model.

3.4.3 Nozzle flow calculation with radiative cooling effect

In subsection 3.4.1, we observed that a slight reduction of the freestream translational temperature gives a better agreement of the computed surface pressure distribution with that of the corresponding experimental data. In this subsection, we consider radiative cooling effect as a clue to reduce the freestream translational temperature and examine whether such reduction is likely to occur. We note that radiative cooling effect is not accounted for in computing the freestream conditions in the JAXA in-house code. In order to quantify radiative cooling effect, an axi-symmetric RANS simulation of the flowfield indicated in Fig. 3.1 is conducted using the same code described in subsection 3.2. The Spalart-Allmaras (SA) turbulence mode[7] is employed where a fully turbulent flowfield in the nozzle is assumed.

As mentioned earlier, the initial stagnation conditions are determined by using the measured total pressure and velocity of incident shock. The chemical compositions are determined by NASA CEA[16] where the thermochemical equilibrium assumption is employed. The inflow boundary conditions are given by these stagnation conditions while the supersonic outflow condition is applied to the exit boundary. The non-slip boundary condition is enforced on the wall which is assumed as a non-catalytic and isothermal wall. The wall temperature is assumed as 300 K. As the initial condition in the nozzle region behind the second diaphragm, the static pressure $p = 5$ Pa, the

temperature are $T_t = T_v = 300$ K, the velocity is $u = 0$ m/s, and fractions of chemical species are 76.7% N_2 and 23.3% O_2 by mass. We employ a structured mesh having 289 points in the axial direction and 128 points in the radial direction.

The radiative energy loss is determined by the following equation

$$E_{\text{loss}} = \int \int \epsilon_\lambda d\lambda d\Omega = 4\pi \int \kappa_\lambda B_\lambda d\lambda, \tag{3.36}$$

where ϵ_λ and κ_λ are the emission coefficient and absorption coefficient at a given wave length λ, respectively. The Planck function is given by B_λ. The absorption coefficient κ_λ is calculated by SPRADIAN2[17]. The radiative energy loss E_{loss} multiplied by the interval of time dt is subtracted from the total and vibrational energies at each time step until the steady flowfield is obtained. Then, the absorption coefficients are reevaluated using the updated flowfields, and the new steady flowfield is computed. These iterative calculations are continued until a fully converged and consistent flowfield is obtained.

The computed translational and vibrational with/without radiative cooling effect are compared in Fig. 3.16. Both the translational and vibrational temperatures decrease substantially near the nozzle exit due to radiative cooling effect. The translational temperature on the axis at the nozzle exit is decreased by 247 K. Although the stagnation enthalpy is slightly higher, there is an experimental data for the Pitot pressure profile at the nozzle exit, which can be used in the validation of the computed results. In Fig. 3.17, the Pitot pressure profile for the stagnation enthalpy of $H_0 = 19.0$ MJ/kg and the stagnation pressure of $P_0 = 49.8$ MPa is compared with those given by the present calculations with or without radiative cooling effect and with that given in Ref. 5. Because the computed profile shown in Ref. 5 does not include the radiative cooling effect, the present calculation without the effect agrees quite well. However, the obtained Pitot pressure in the core region is obviously higher than that obtained in the experiment. On the other hand, when the radiative cooling effect is accounted for in the calculation, the overall agreement with the experimental data becomes fine. This strongly suggests the importance of radiative cooling effect in

obtaining the upstream condition particularly when the stagnation enthalpy is high.

The obtained flow variables at the nozzle exit are then employed as the upstream conditions in the calculation of pressure distribution over the model surface. In Fig. 3.18, the computed surface pressure distributions are compared for the stagnation enthalpy of $H_0 = 15.6$ MJ/kg. As expected, an excellent agreement is obtained for the surface pressure distribution with that of the experimental data when the radiative cooling effect in the nozzle region is taken into account. The nozzle flowfield calculation with the radiative cooling effect is also conducted at the lower enthalpy condition of $H_0 = 8.0$ MJ/kg. The translational temperature in the nozzle is shown in Fig. 3.19. One can find that the effect of radiative cooling on the translational temperature is small. Figure 3.20 shows the surface pressure with or without the radiative cooling. An excellent agreement with the measured data is obtained. One can find that the measure surface pressure can be consistently explained by the radiative cooling.

3.5 Conclusions

The cause of the observed overestimation of the computed wall pressure along the surface of a blunt-nosed test model under high enthalpy conditions of HIEST was explored. The present study revealed the followings: (1) When radiative cooling effect was included in the calculation of the flowfield in the nozzle region, the temperature at the nozzle exit was substantially decreased. The Pitot pressure profile at the nozzle exit agreed well with the experimental data if radiative cooling effect was accounted for. (2) The computed surface pressure distribution along the blunt test model agreed well with the measured in the experiment when the upstream boundary condition was given by the computed result in the nozzle region in which radiative cooling effect was taken into account. (3) Neither the uncertainty in translational-vibrational relaxation time nor that in chemical reaction rates could explain the observed discrepancy in the surface pressure distribution. (4) The uncertainty in the chemical composition of

the upstream boundary condition was not likely to be the cause of the discrepancy in the surface pressure distribution.

Table. 3.1 Upstream conditions computed by the JAXA in-house code[1]

H_0 MJ/kg	ρ_∞ kg/m^3	V_∞ m/s	$T_{t\infty}$ K	$T_{v\infty}$ K	Re_∞ $\times 10^6$[1/m]	$C_{O\infty}$	$C_{N\infty}$	$C_{NO\infty}$	$C_{O_2\infty}$	$C_{N_2\infty}$
3.8	0.0123	2600	292	516	1.65	0.0006	0.0000	0.0413	0.2104	0.7477
8.0	0.0101	3667	787	809	1.05	0.0163	0.0000	0.0540	0.1879	0.7418
10.1	0.0075	4059	998	1014	0.74	0.0421	0.0000	0.0513	0.1635	0.7431
15.6	0.0049	4886	1327	1344	0.47	0.1310	0.0000	0.0372	0.0821	0.7497

Table. 3.2 Assumed upstream chemical compositions at $H_0 = 15.6$ MJ/kg

Case	$C_{O\infty}$	$C_{N\infty}$	$C_{NO\infty}$	$C_{O_2\infty}$	$C_{N_2\infty}$
Case A	0.00000	0.0000	0.0372	0.08210	0.7497
Case B	0.04890	0.0000	0.0372	0.21310	0.7497
Case C	0.08995	0.0000	0.0372	0.16420	0.7497
Baseline	0.13100	0.0000	0.0372	0.12315	0.7497
Case D	0.21310	0.0000	0.0372	0.00000	0.7497

Table. 3.3 Assumed upstream chemical compositions at $H_0 = 10.1$ MJ/kg

Case	$C_{O\infty}$	$C_{N\infty}$	$C_{NO\infty}$	$C_{O_2\infty}$	$C_{N_2\infty}$
Case E	0.0421	0.0000	0.0513	0.1635	0.7431
Baseline	0.0000	0.0000	0.0513	0.2056	0.7431
Case F	0.2056	0.0000	0.0513	0.0000	0.7431

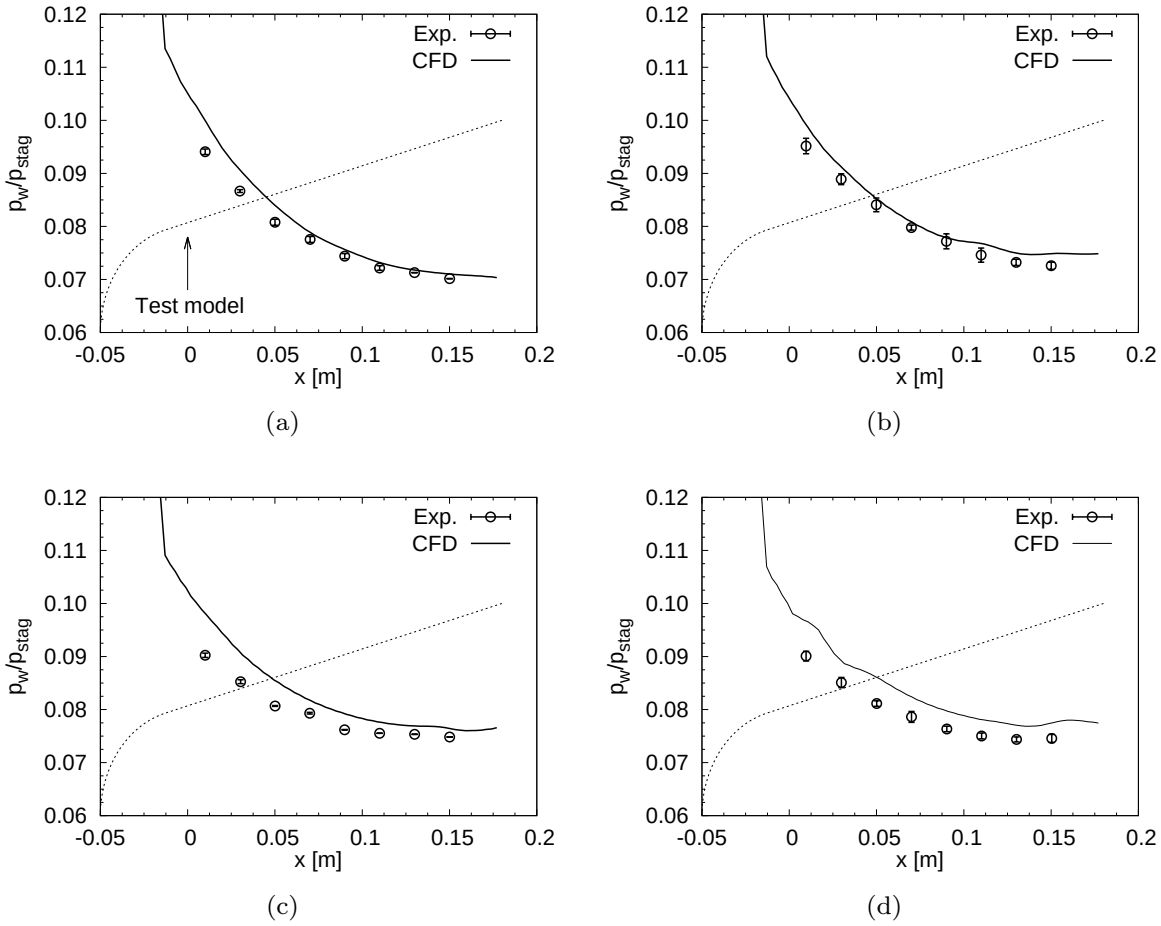

Fig. 3.1 Comparison of normalized wall pressure with HIEST data; (a) H_0=3.8 MJ/kg, (b) 8.0 MJ/kg, (c) 10.1 MJ/kg, and (d) 15.6 MJ/kg. The dotted line indicates the outline of the test model.

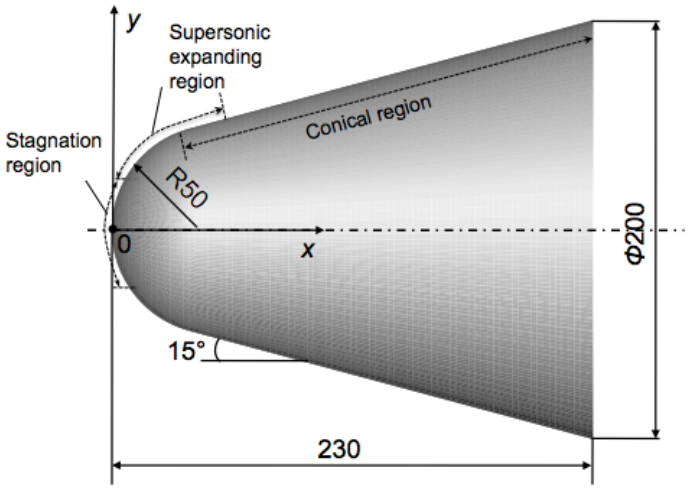

Fig. 3.2 Schematic of the blunt-nosed test model used in the measurement of aerodynamics characteristics in HIEST.

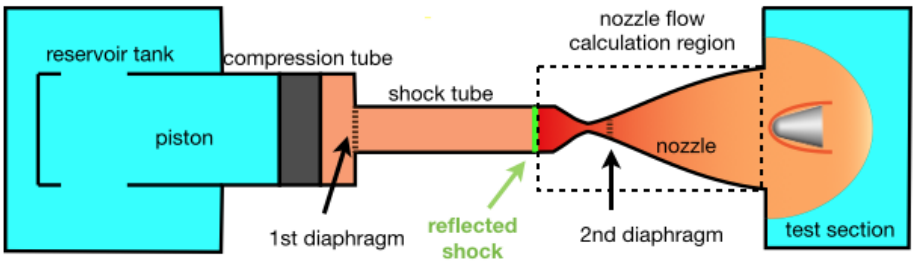

Fig. 3.3 Nozzle flowfield calculation region.

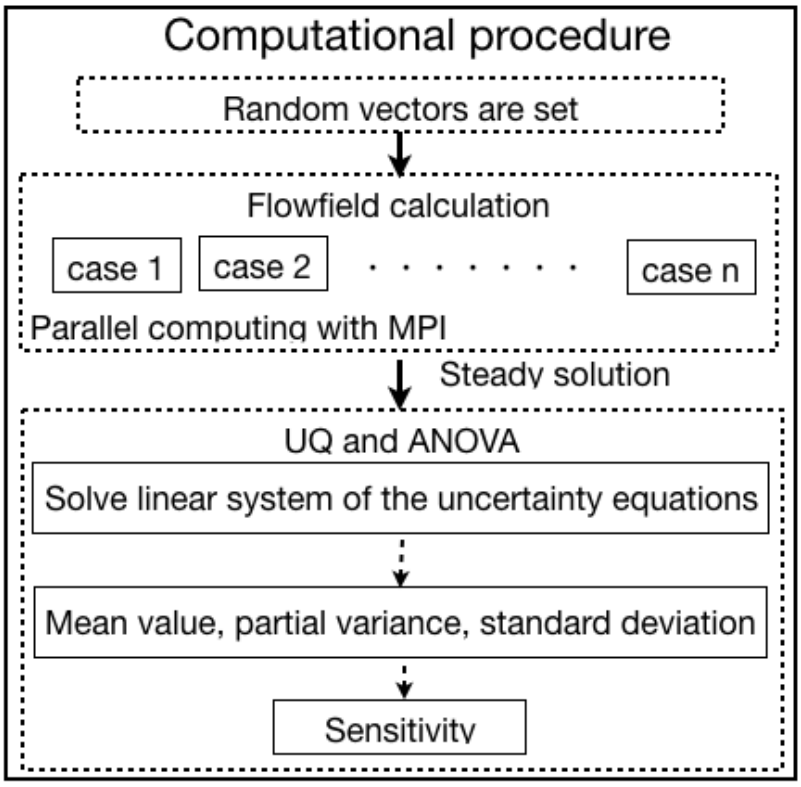

Fig. 3.4 Computational procedure.

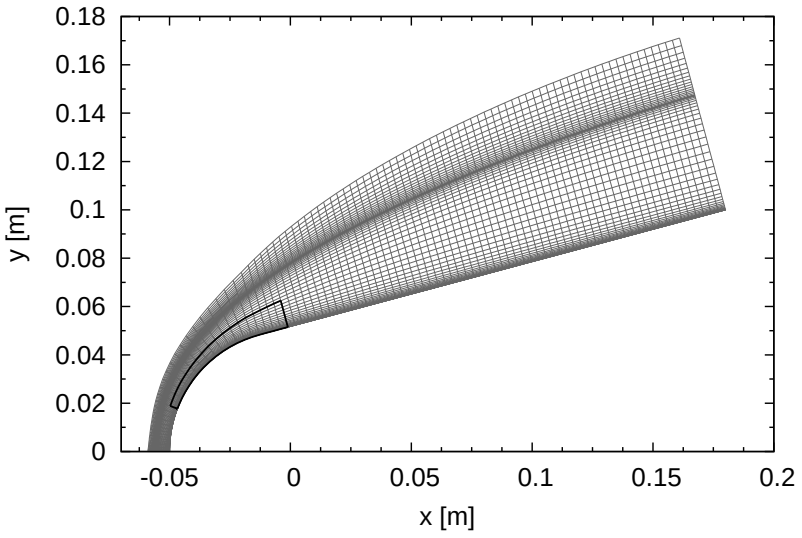

Fig. 3.5 Solution-adaptive grid employed in the present calculations. The chemical reaction rates are changed in the enclosed region by a bold line.

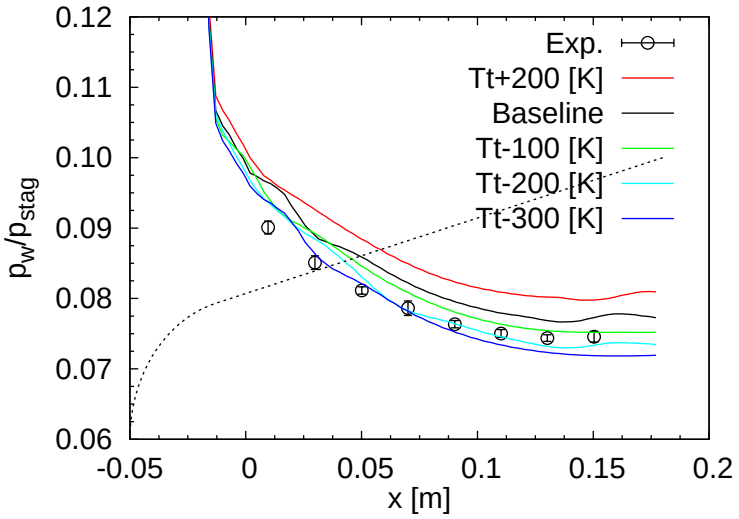

(a) Translational temperature

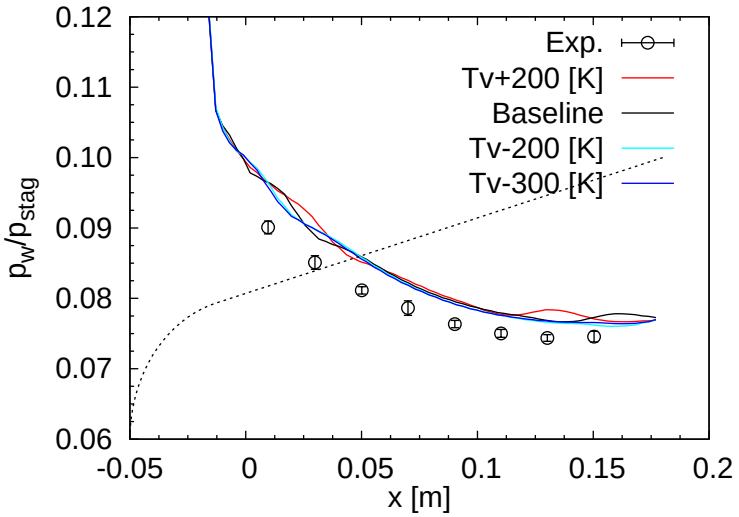

(b) Vibrational temperature

Fig. 3.6 Comparison of the surface pressure distributions when the translational temperature and vibrational temperature are changed for the stagnation enthalpy of $H_0 = 15.6$ MJ/kg.

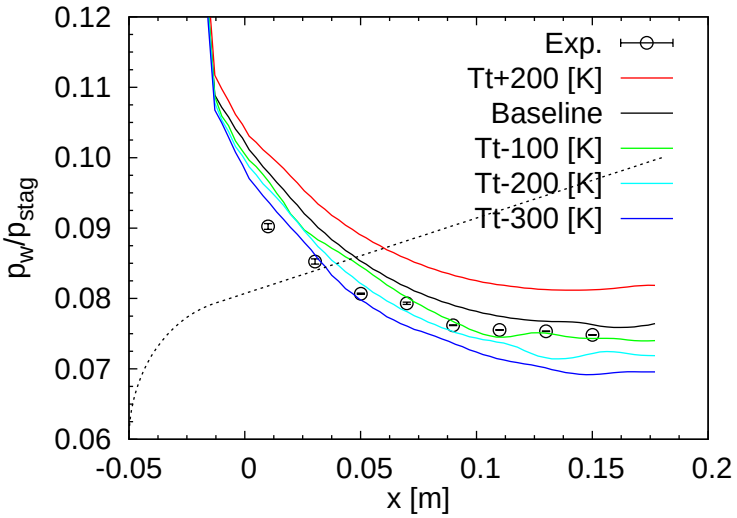

(a) Translational temperature

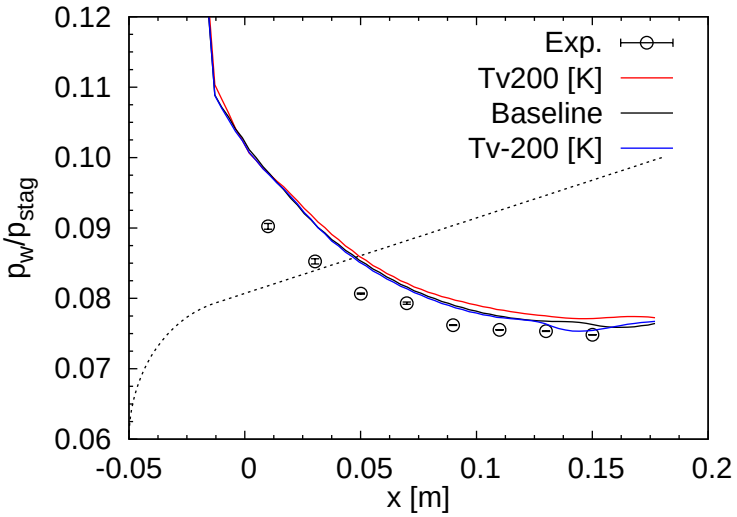

(b) Vibrational temperature

Fig. 3.7 Comparison of the surface pressure distributions when the translational temperature and vibrational temperature are changed for the stagnation enthalpy of $H_0 = 10.1$ MJ/kg.

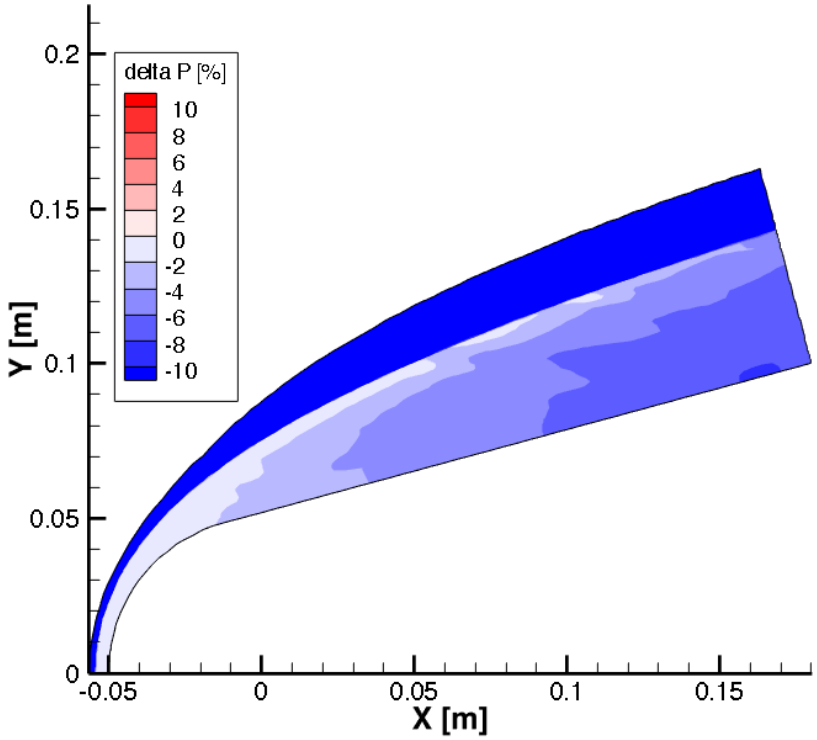

Fig. 3.8 Variation in pressure distribution defined by $(p_{tt-300K} - p_{\text{baseline}}/p_{\text{baseline}}) \times 100$ % for the stagnation enthalpy of $H_0 = 15.6$ MJ/kg, where $p_{tt-300K}$ denotes the pressure when the freestream translational temperature is decreased by 300 K.

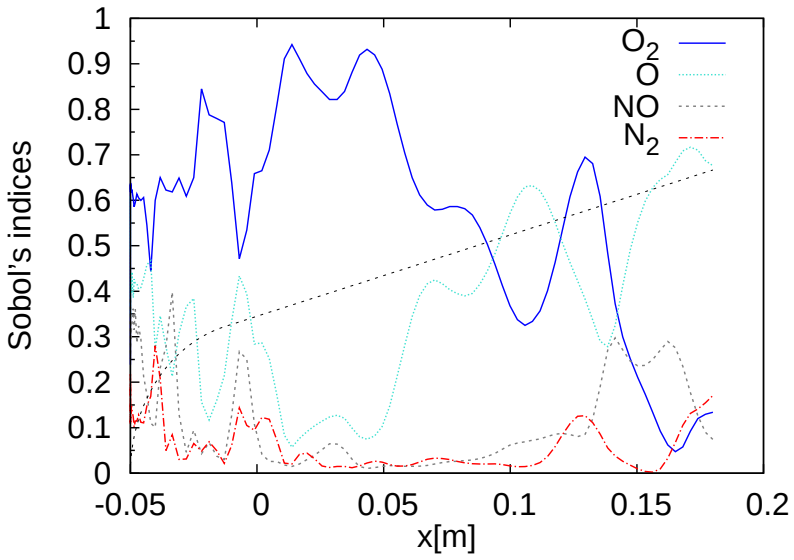

Fig. 3.9 Computed sensitivity of the upstream chemical compositions on the surface pressure for the stagnation enthalpy of $H_0 = 15.6$ MJ/kg.

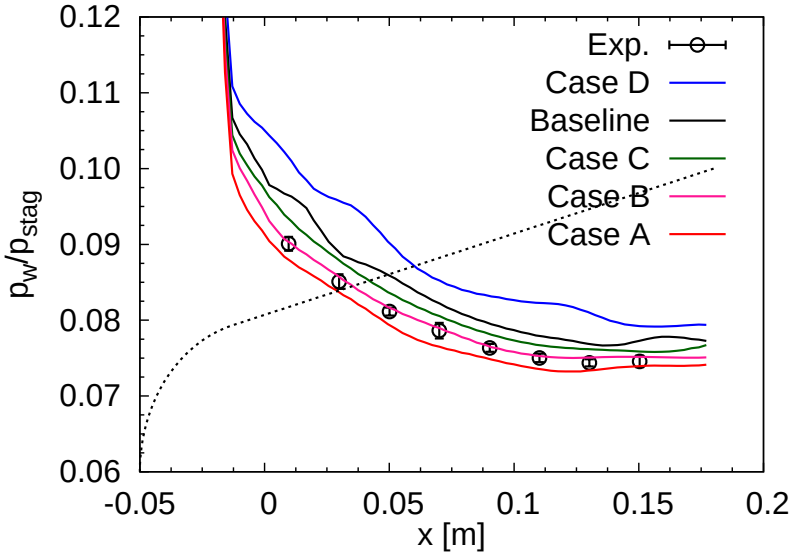

Fig. 3.10 Computed surface pressure distributions for different upstream chemical compositions for the stagnation enthalpy of $H_0 = 15.6$ MJ/kg.

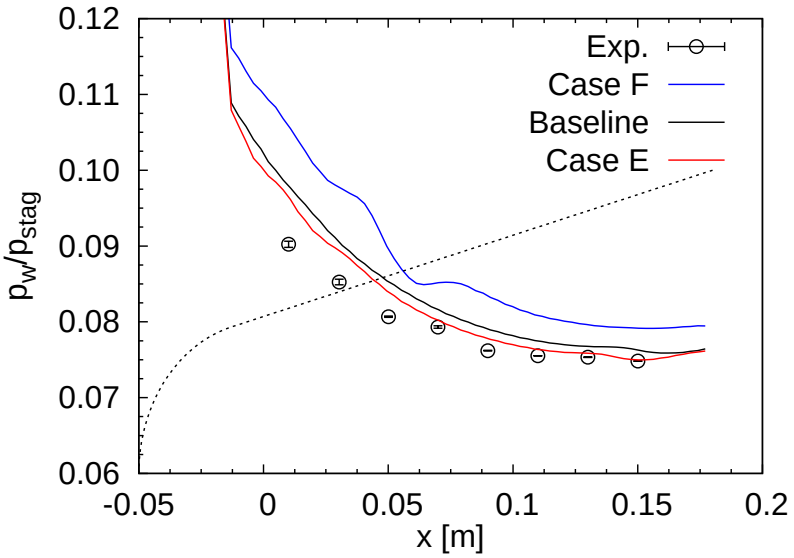

Fig. 3.11 Computed surface pressure distributions for different upstream chemical compositions for the stagnation enthalpy of $H_0 = 10.1$ MJ/kg.

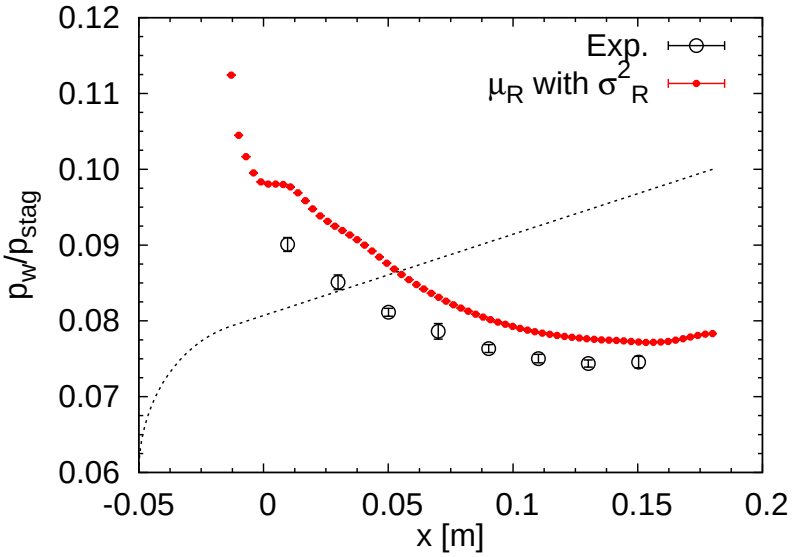

Fig. 3.12 Mean values with the standard deviations of the surface pressure distribution when the translational-vibrational relaxation time are varied for the stagnation enthalpy of $H_0 = 15.6$ MJ/kg.

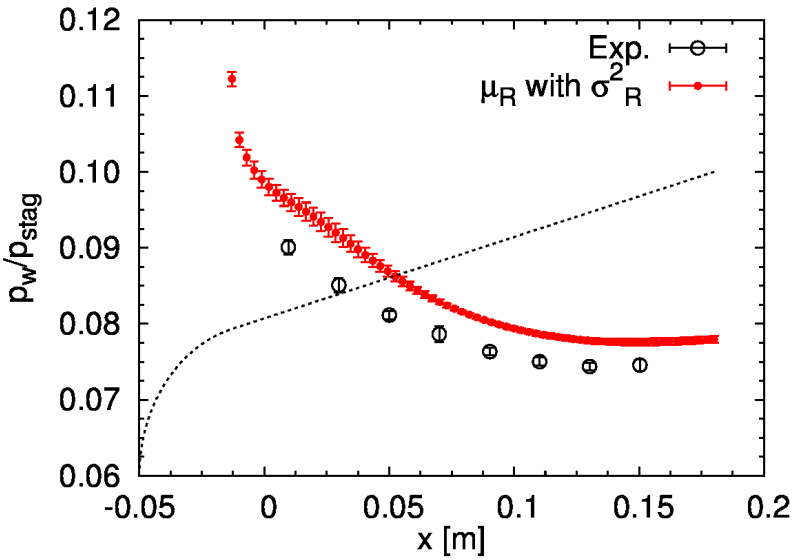

Fig. 3.13 Mean value with the standard deviation of the surface pressure distribution when the forward rates are changed for the stagnation enthalpy of H_0=15.6 MJ/kg.

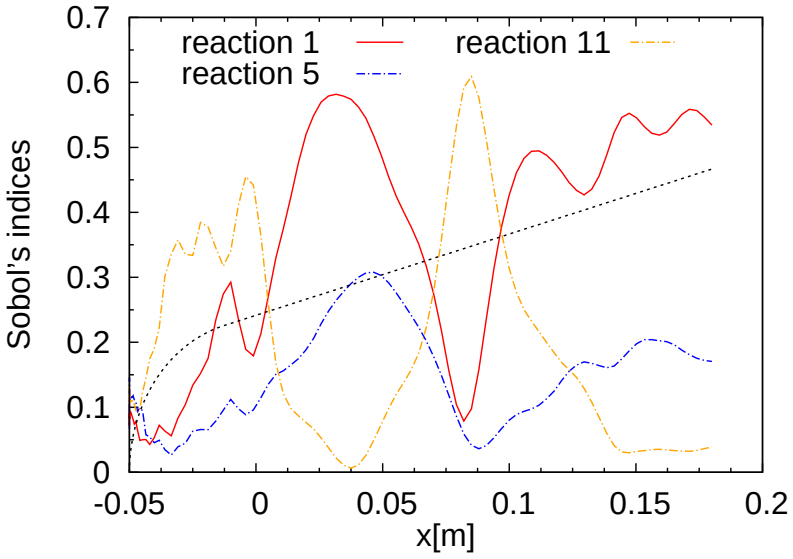

Fig. 3.14 Sensitivity of chemical reaction rates indicated by Sobol's indices for the reaction 1 ($O_2 + O \rightleftharpoons O + O + O$), reaction 5 ($O_2 + O \rightleftharpoons N_2 + O + N_2$) and reaction 11 ($NO + O \rightleftharpoons N + O + O$). The stagnation enthalpy is $H_0 = 15.6$ MJ/kg.

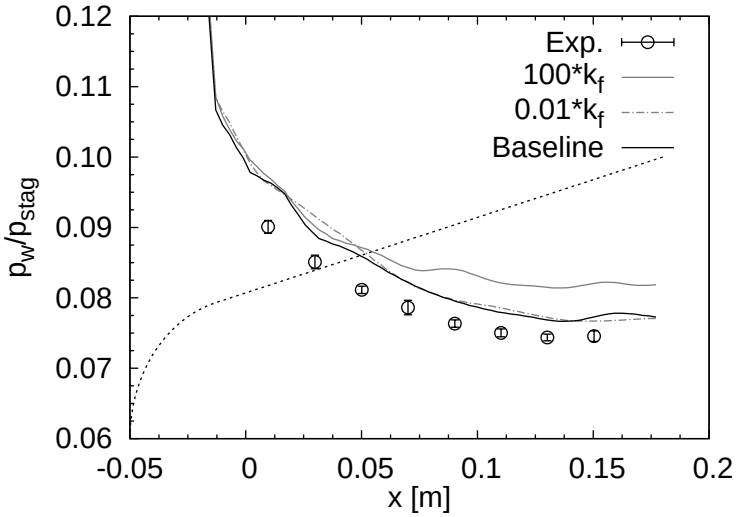

(a) Reaction 1

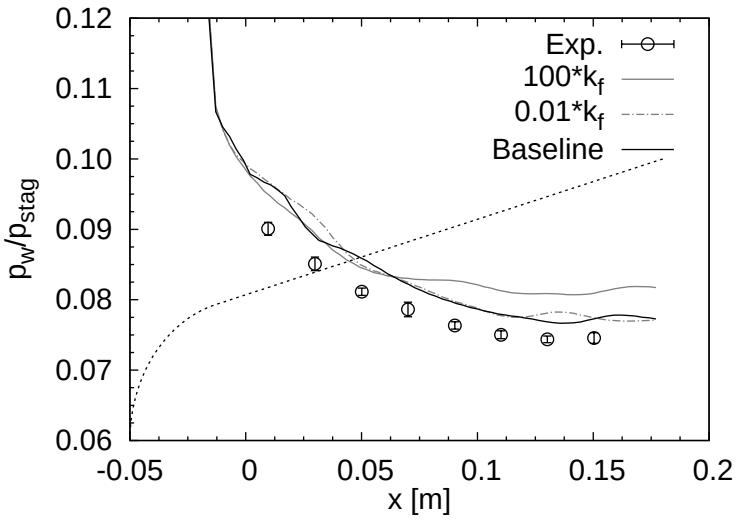

(b) Reaction 5

Fig. 3.15 Computed surface pressure distributions when the forward reaction rates for reactions 1 and 5 are varied form 0.01 to 100 times of the original values for the stagnation enthalpy of $H_0 = 15.6$ MJ/kg. Those curves labeled as Baseline show the computed pressure distributions using the original forward reaction rates; (a) reaction 1 ($O_2+O \rightleftharpoons O+O+O$), and (b) reaction 5 ($O_2+O \rightleftharpoons N_2+O+N_2$).

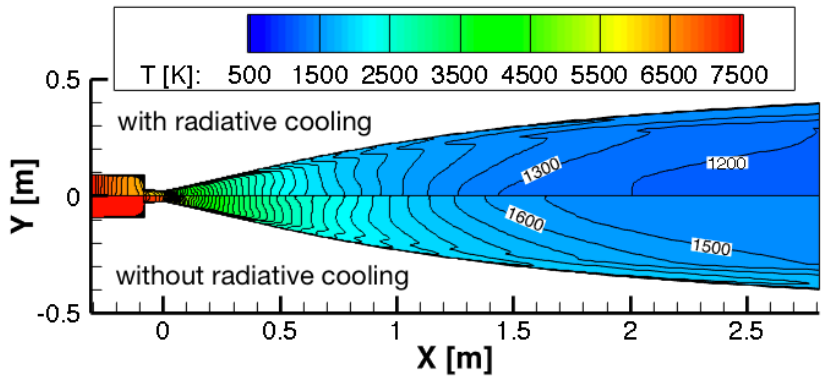

(a) Translational temperature

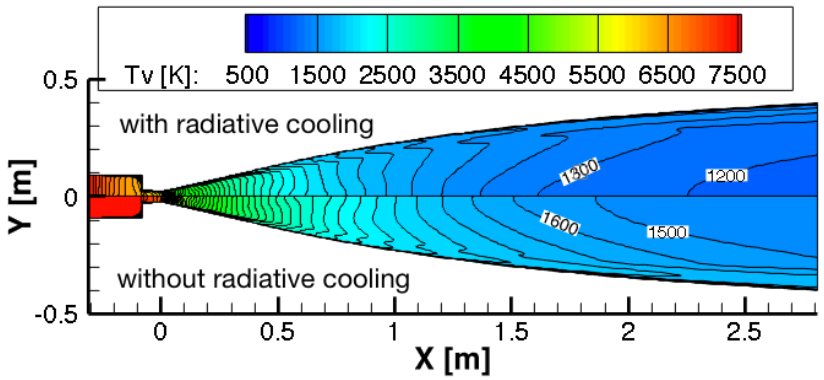

(b) Vibrational temperature

Fig. 3.16 Temperature contours given by the present nozzle flow calculation with/without radiative cooling effect for the stagnation enthalpy of H_0 = 15.6 MJ/kg.; (a) translational temperature, and (b) vibrational temperature

.

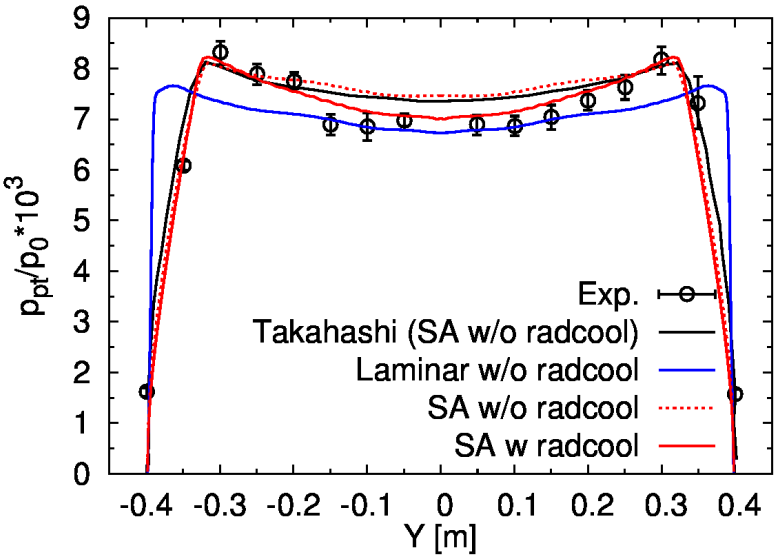

Fig. 3.17 Pitot pressure profiles at the nozzle exit for the stagnation enthalpy of $H_0 = 19.0$ MJ/kg.

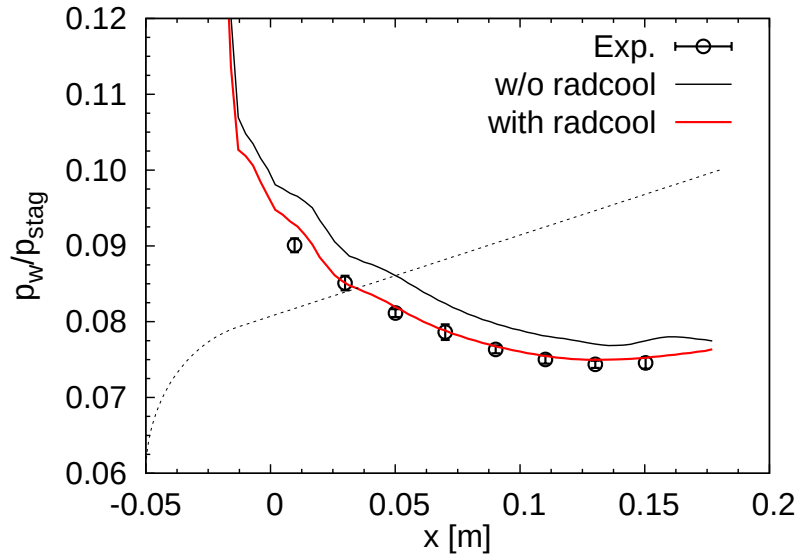

Fig. 3.18 Computed surface pressure distribution using the upstream boundary condition with/without radiative cooling effect for the stagnation enthalpy of $H_0 = 15.6$ MJ/kg.

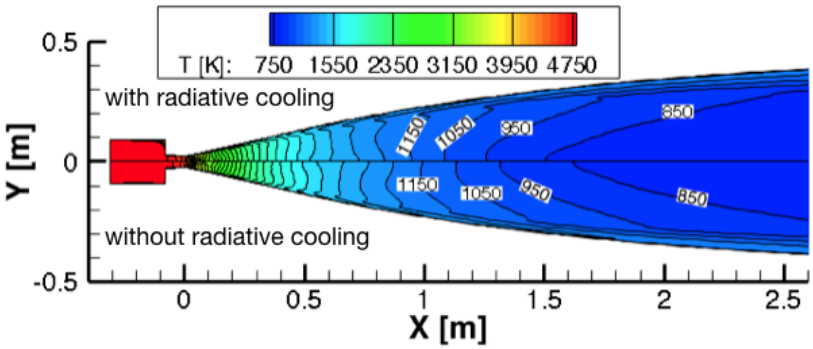

Fig. 3.19 Translational temperature contours by the present nozzle flow calculation with/without radiative for the stagnation enthalpy of $H_0 = 8.0$ MJ/kg.

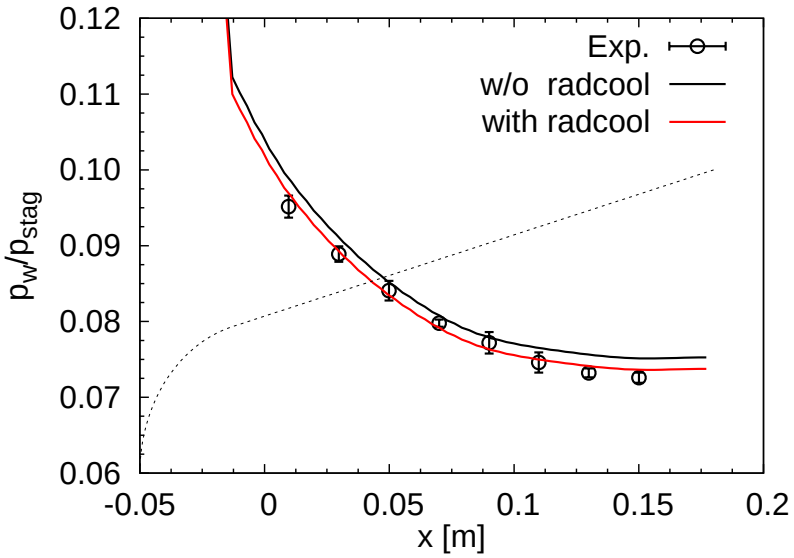

Fig. 3.20 Computed surface pressure distribution using the upstream boundary condition with/without radiative cooling effect for the stagnation enthalpy of $H_0 = 8.0$ MJ/kg.

Bibliography

[1] Takahashi, M., Kodera, M., Itoh, K., Komuro, T., Sato, K., and Tanno, H., "Influence of Thermal Non-equilibrium on Nozzle Flow Condition of High Enthalpy Shock Tunnel HIEST," AIAA Paper 2009-7267, 2009.

[2] Park, C., *Nonequilibrium Hypersonic Aerothermodynaics*, John Wiley and Sons, Inc., 1989.

[3] Park, C., "Review of Chemical-Kinetic Problems of Future NASA Mission, I:Earth Entries," *Journal of Thermophysics and Heat Transfer*, Vol. 7, No. 3, 1993, pp. 385–298.

[4] Millikan, R. C. and White, D. R., "Systematics of Vibrational Relaxation," *Journal of Chemical Physics*, Vol. 39, No. 12, 1963, pp. 3209–3213.

[5] Eldred, M. S.,, "Recent Advances in Non-Intrusive Polynomial Chaos and Stochastic Collocation Methods for Uncertainty Analysis and Design," AIAA paper 2009-2274, 2009.

[6] Hosder. S., Walters, R. W., and Balch, M., "Point-Collocation Nonintrusive Polynomial Chaos Method for Stochastic Computational Fluid Dynamics," *AIAA Journal*, Vol. 48, No. 12, 2010, pp. 2721–2730.

[7] Spalart, P. R. and Allmaras, S. R., "A One-Equation Turbulence Model for Aerodynamic Flows," AIAA paper 92-0439, 1992.

[8] Gupta, R. N., Yos, J. M., Thompson, R. A., and Lee, K., P, "A Review of Reaction Rates and Thermodynamic and Transport Properties for an 11-Species Air Model for Chemical and Thermal Nonequilibrium Calculations to 30000 K,"

Reference Publications RP-1232, NASA, 1990.

[9] Shima, E. and Kitamura, K., "Parameter-Free Simple Low-Dissipation AUSM-Family Scheme for All Speeds," *AIAA Journal*, Vol. 49, No. 8, 2011, pp. 1639–1709.

[10] Kitamura, K., Shima, E., Nakamura, Y., and Roe. P. L., "Evalution of Euler Fluxes for Hypersonic Heating Computations AUSM-Family Schemes for Hypersonic Heating Computations," *AIAA Journal*, Vol. 48, No. 4, 2010, pp. 763–776.

[11] Van Leer, B., "Towards the Ultimate Conservation Difference Scheme V. A Second-Order Sequel to Godunov's Method," *Journal of Computational Physics*, Vol. 23, No. 3, 1979, pp. 101–136.

[12] Eberhart, S. and Imalay, S., "Diagonal Implicit Scheme for Computing Flows with Finite Rate Chemistry," *Journal of Thermophysics and Heat Transfer*, Vol. 6, No. 3, 1992, pp. 208–216.

[13] Sudret, B., "Global Sensitivity Analysis Using Polynomial Chaos Expansions," *Reliability Engineering & System Safety*, Vol. 93, No. 7, 2008,, pp. 864–979.

[14] Sobol. T. M., "Global Sensitivity Indices for Non-linear Mathematical Models and Their Montecarlo Estimates," *Mathematics and Computers in Simulation*, Vol. 55, 2001, pp. 271–280.

[15] Candler, G. V. and Nompelis, I., "Computational Fluid Dynamics for Atomospheric Entry," *Von Karman Institute for Fluid Dynamics Lecture Series*, Vol. 6, No. RTO-EN-AVT-162, 1992, pp. 15/1–15/56.

[16] Gordon, S. and McBride, B. J., "Computer Program for Calculation of Complex Chemical Equilibrium Compositions and Applications," Reference Publications RP-1211, NASA, 1996.

[17] Fujita, K. and Abe, T., "SPRADIAN Structured Package for Radiation Analysis: Theory and Application," Reference Publications Rept. 96, Inst. of Space and Astronautical Science, 1997.

Chapter 4

Numerical Study of Heat Flux Augmentation due to a Diamond Roughness

4.1 Introduction

The measured heat flux data[1, 2] on the back shell with roughness are shown in Fig. 4.1. Figure 4.2 shows the back shell surface of the HTV-R test model having a diameter of 250 [mm]. The seven elements of diamond roughness are mounted on the back shell as shown in Fig. 4.3. The upstream conditions are two different total enthalpy conditions: the freestream total enthalpy of $H_0 = 3.6$ [MJ/kg] corresponding to a lower enthalpy, and the freestream total enthalpy of H_0 =8.6 [MJ/kg] corresponding to a higher enthalpy condition. Freestream Mach number, Reynolds number density, velocity, temperature and mass fractions are summarized in Table 4.1. The angle of attack is 28 [deg]. The heat flux became $2-4$ times higher behind the roughness and RANS underestimates the heat flux. However, it is well known that flow becomes fully turbulent although HIEST can generate higher Reynolds number flow at higher enthalpy conditions in shock tunnels. In order to examine the flowfield around the diamond roughness, higher order code in hypersonic flow is needed.

The objective of this study is to examine the flowfield around a roughness in the HIEST conditions using high order code. We first developed the high order code for the hypersonic flow. Then we calculate the flowfield around the diamond roughness on the back shell of HTV-R and examine the flowfield using our developed code.

4.2 Numerical Procedure

4.2.1 Governing equations and numerical methods

The governing equations are the three-dimensional Navier-Stokes equations accounting for thermochemical non-equilibrium. Park's two-temperature thermochemical model [3] is employed. We consider five neutral air species (O, N, NO N_2 and O_2). Instead of solving all of these species conservation equations, N_2 and O_2 are calculated by total density, the density of O, N and NO, and the conservation of element ratio [3]. The details are shown in Section 2.2.

4.2.2 Discretization of the governing equations

Governing equations are discritized by the cell-centered finite volume method. For time integration, we use the block LU-SGS method with inner iteration [4, 5], and the diagonal point implicit method [6] is utilized in order to improve stability in the integration of the source terms. The convective numerical flux is calculated using the SLAU scheme [7, 8]. The viscous flux is evaluated by a central difference scheme. In order to compute hypersonic turbulent flows, high order code should be robust enough to capture strong shock waves and be capable of resolving boundary layer. In this study, we employ the fifth order WENO scheme developed by Matsuyma[9]. Matsuyama used the recently developed WENO scheme for the interpolation of the values at cell interfaces based on the finite volume method. The Thornber's correction[10] is utilized for further reducing numerical dissipation. The calculated statistics in a channel flow such as the streamwise mean velocity and the root-mean-square velocity fluctuations showed good agreements with the DNS results computed by Kim et al[11].

The left-side (L) and right-side (R) values at cell interfaces are interpolated by the method proposed by Taylor[12]. In the original WENO method which was developed by Jiang and Liu[13, 14], the left side values at the cell interface $i+1/2$ are determined

by following equations,

$$q_i^R = \sum_{k=0}^{r-1} \omega_k q_k^r, \tag{4.1}$$

$$q_k^r = \sum_{l=0}^{r-1} a_{kl}^r \; q_{i-r+k+l+1}, \tag{4.2}$$

where k is the individual stencil number and ω_k is the weight assigned to the kth stencil. This weight ω_k is calculated by

$$\omega_k = \frac{\alpha_k}{\sum_{l=0}^{r-1} \alpha_l}, \tag{4.3}$$

$$\alpha_k = \frac{C_k^r}{(IS_k + \epsilon)^p}, \tag{4.4}$$

where the smooth indicator IS_k is

$$IS_k = \sum_{m=1}^{r-1} \left(\sum_{l=0}^{r-1} d_{klm}^r q_{i-r+k+l+1} \right)^2. \tag{4.5}$$

Taylor et al[12]. introduced a new limiting procedure to mitigate the over-adaptation tendencies of the WENO methods. This procedure forces the optimal weights, if the ratio between maximum and minimum smoothness indicators $R(IS)$ is smaller than a certain threshold value α. The ratio of the smooth indicator, $R(IS)$is defined by

$$R(IS) = \frac{\max_{0 \le k \le r}(IS_k)}{\min_{0 \le k \le r}(IS_k) + \epsilon}. \tag{4.6}$$

Then the candidate stencil weights are now computed as

$$\omega_k = \begin{cases} C_k^r & R(IS) < \alpha_{IS} \\ \frac{\alpha_k}{\sum_{l=0}^{r} \alpha_l} & \text{otherwise} \end{cases}. \tag{4.7}$$

This relative limiter $R(IS)$ can reduce the numerical dissipation, and the method was successfully adopted in DNS of shock wave and turbulent boundary layer interaction[15]. Although the threshold value α_{IS} is arbitrary depends on the

problem, the recommended value α_{IS} is employed in the present study. The maximum order achieved in the WENO of Jiang et al. is $2r-1$, and $r=3$ giving the fifth-order accuracy is chosen in the present study. The coefficients α_{kl}^3, C_k^3, d_{klm}^3 and can be found in the literature[13]. As interpolated variables, we choose the primitive variables ρ, u, v, w and p. The velocities are further modified by Thornber's correction. Thornber et al. proposed a simple correction to reduce the dissipation at low Mach numbers[10]. They proved that the dissipation could be significantly reduced by following corrections,

$$\boldsymbol{v}_L^{LM} = \frac{\boldsymbol{v}_L + \boldsymbol{v}_R}{2} + z\frac{\boldsymbol{v}_L - \boldsymbol{v}_R}{2}, \tag{4.8}$$

$$\boldsymbol{v}_R^{LM} = \frac{\boldsymbol{v}_L + \boldsymbol{v}_R}{2} - z\frac{\boldsymbol{v}_L - \boldsymbol{v}_R}{2}, \tag{4.9}$$

where

$$z = \min[1, \max(M_L, M_R)]. \tag{4.10}$$

$V_{L/R}$ are the left and right interpolated velocity vectors, $V_{L/R}^{LM}$ are the low Mach number adjusted interpolated velocities. In this study, in order to obtain robustness for the strong shock wave, the interpolation method is changed from the WENO to the MUSCL[16] near shock wave. Parallel computation is implemented by domain decomposition with the Message Passing Interface (MPI) library used for inter processor communication.

4.3 Results and discussions

A computational region for the flowfield calculation around a roughness is shown in Fig. 4.5. The inflow boundary conditions are interpolated by the profile of the flowfield calculation around the HTV-R test model as shown in Fig. 4.6. Figure 4.7 shows the scale of the computational region near a roughness. These grids are 513 points in the wall normal direction and in the direction along the wall, and 301 points in the spanwise direction. The distance between the first layer and the wall surface is set to 10^{-7} m. These grid points and distance are determined by the grid convergence property of the heat flux.

Figure 4.8 shows the distribution of time-averaged heat flux for 1.5 [ms] which is comparable with the test time in the experiment. Figure 4.9 shows the TSP image of temperature increase[1]. Since two streaks of high heat flux par a roughness appears, our calculated results can get qualitative agreement with the TSP data. Figure 4.10 shows the isosurface of Q-value near the roughness. A few horseshoe vortexes are formed in front of the roughness, and counterrotating vortex tubes 1 and 2 behind the roughness are generated. These counterrotating vortex tubes get close to the symmetry plane immediately behind the roughness where the pressure becomes lower and expand in the spanwise direction towards the downstream. Figure 4.11 shows the helicity density distribution in x-direction on x-constant surfaces behind a roughness. Red and blue contours indicate clockwise eddy and anticlockwise eddy, respectively. Since the counterrotating vortex tube 1 extends to the boundary layer edge, the higher temperature flow near boundary layer edge is blown down to the wall as shown in Fig. 4.12. On the other hand, the counterrotating vortex tube 2 works as upwash. Therefore, the two streaks of high heat flux appear near symmetry plane and the heat flux becomes low near the boundary in the spanwise. The comparison of calculated time-averaged heat flux with the measured data on the symmetry line is shown in Fig. 4.13. The heat flux can get a good agreement with the measured data in both the lower end higher enthalpy conditions. However, in these conditions, we can find that the high heat flux is generated by these counterrotating vortexes and the flow is expected not to be turbulent. The measured data in HIEST is not enough accurate to predict the fully turbulent heat flux.

4.4 Conclusions

The discrepancy of heat flux on back shell of the HTV-R capsule with diamond roughness between RANS and experiments was examined using our developed high order code. The time averaged heat flux by the flowfield calculation around a roughness with a high order code and fine mesh could obtain significant agreement with the

measured heat flux. It was found that the heating mechanism behind the roughness is due, not to turbulence but to the counter-rotating vortex tube.

Table. 4.1 Freestream conditions for the aeroheating measurements with roughness in HIEST[17]

H_0 [MJ/kg]	3.6	8.6
M_∞	7.61	6.42
Re_∞ [1/m]	5.11×10^{6}	2.64×10^{6}
ρ_∞ [kg/m^3]	3.486×10^{-2}	2.717×10^{-2}
v_∞ [m/s]	2529.4	3835.8
$T_{t\infty}$ [K]	274.57	908.7
$T_{v\infty}$ [K]	274.57	915.8
$C_{\mathrm{O}\infty}$	4.090×10^{-5}	4.777×10^{-3}
$C_{\mathrm{N}\infty}$	0.0	0.0
$C_{\mathrm{NO}\infty}$	4.014×10^{-2}	6.042×10^{-2}
$C_{\mathrm{O_2}\infty}$	2.103×10^{-1}	1.948×10^{-1}
$C_{\mathrm{N_2}\infty}$	7.367×10^{-1}	7.253×10^{-1}

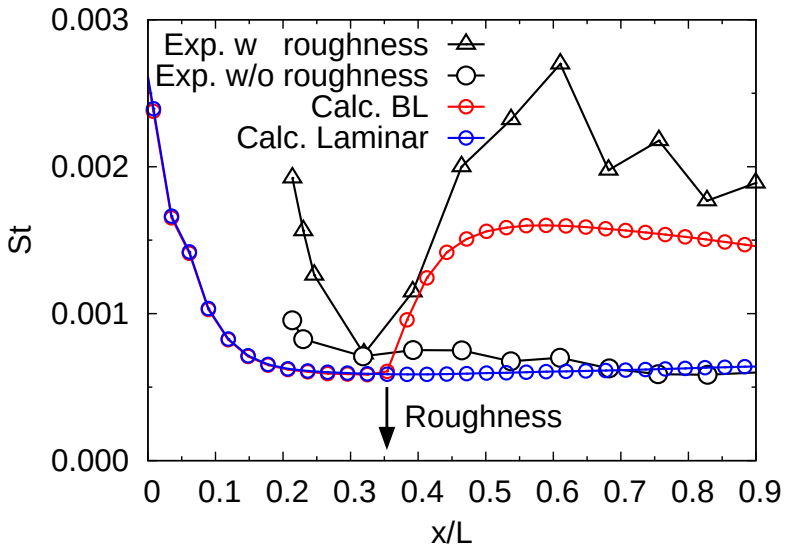

(a) $H_0 = 3.6$ [MJ/kg]

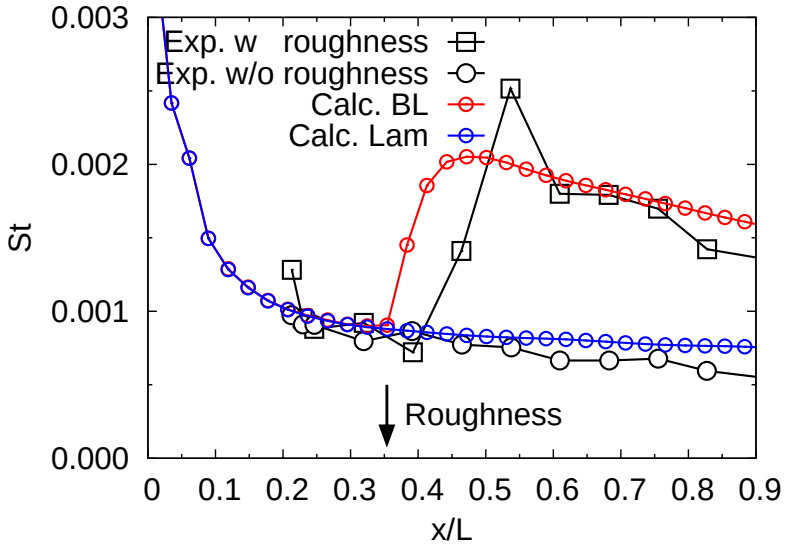

(b) $H_0 = 8.6$ [MJ/kg]

Fig. 4.1 Measured heat flux on the back shell of HTV-R test model.[1, 2]

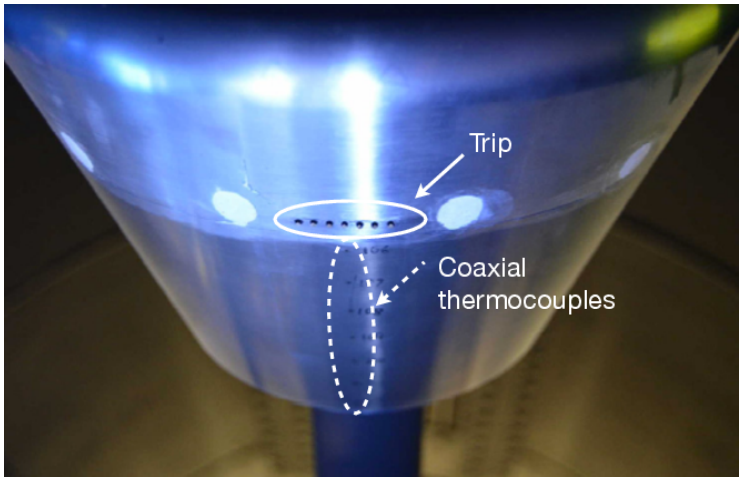

Fig. 4.2 HTV-R back shell with roughness elements.[2]

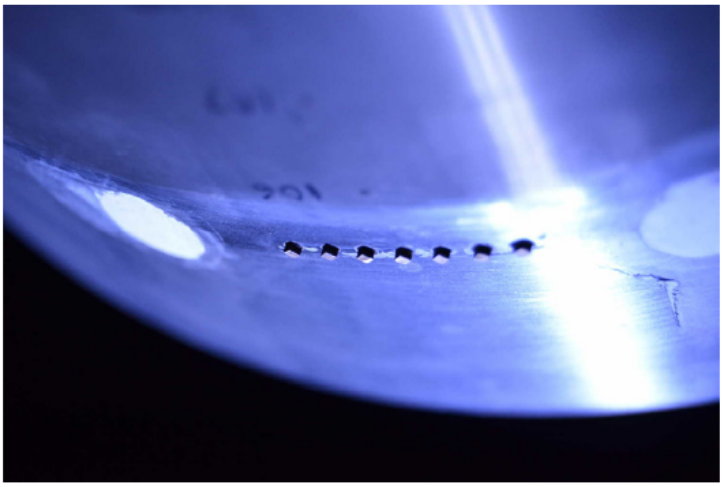

Fig. 4.3 Roughness elements on the back shell: 7 roughness elements are mounted.[2]

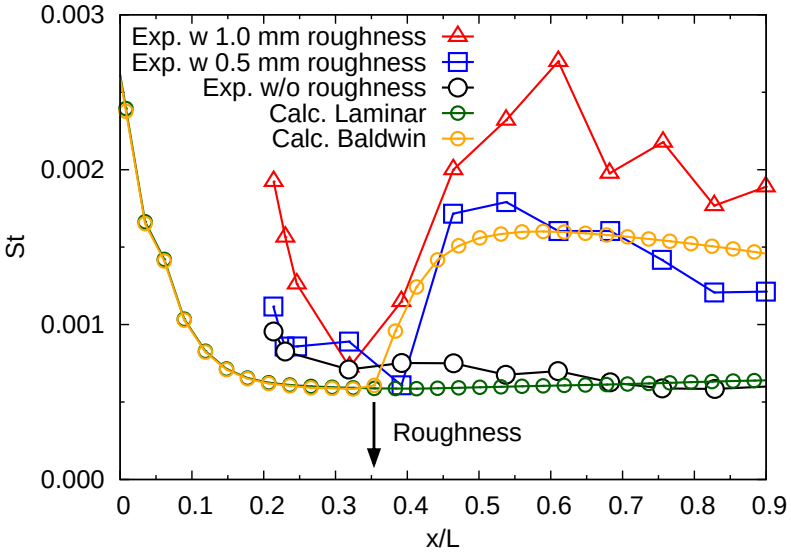

(a) $H_0 = 3.6$ [MJ/kg]

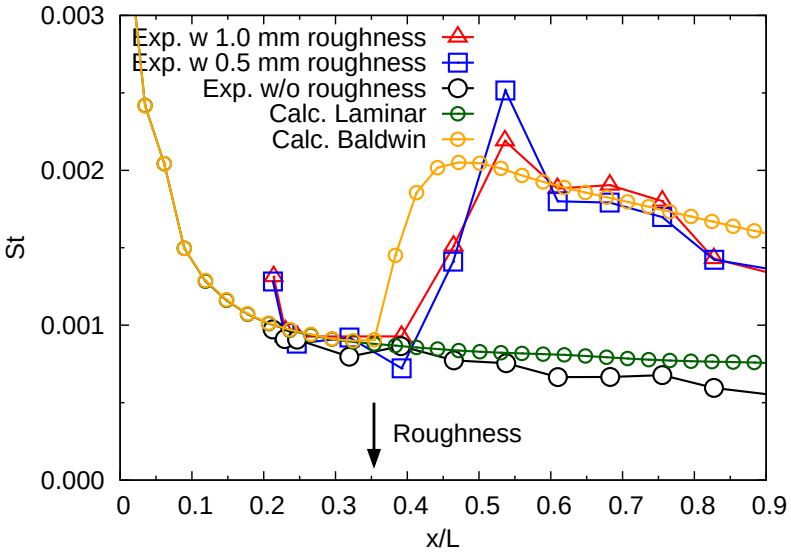

(b) $H_0 = 8.6$ [MJ/kg]

Fig. 4.4 Comparison of calculated heat flux by RANS with the measured data on the back shell of the HTV-R test model.

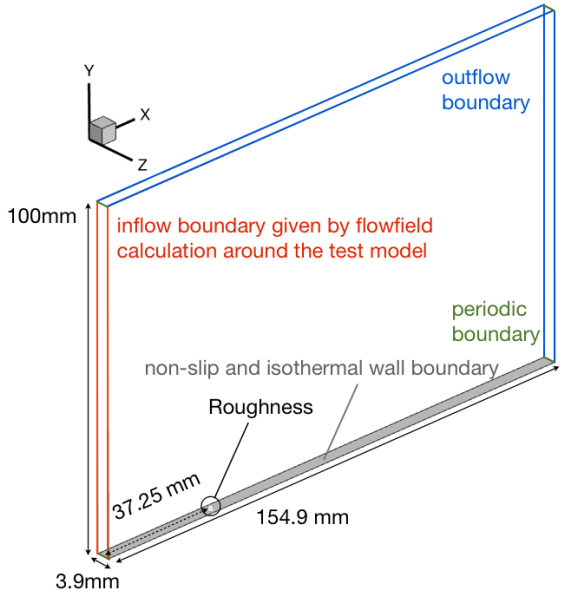

Fig. 4.5 Computational region for the flowfield calculation around the diamond roughness and boundary conditions.

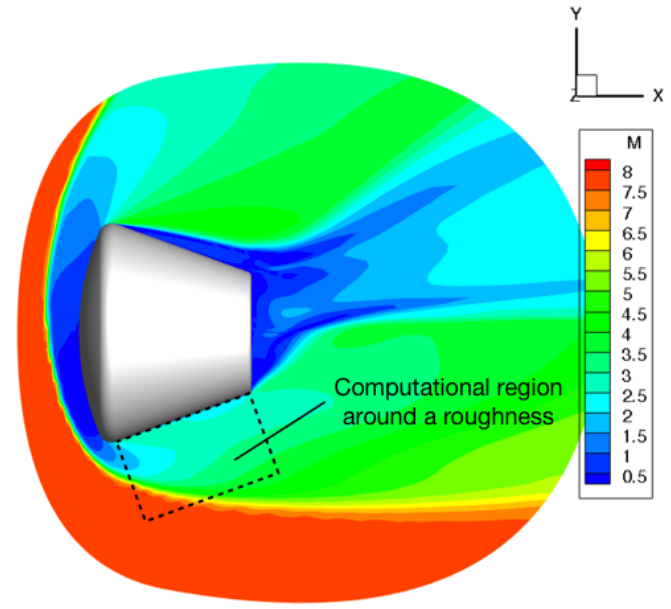

Fig. 4.6 Computational region around the test model: closed region by dashed line is the computational region for the flowfield calculation around the diamond roughness.

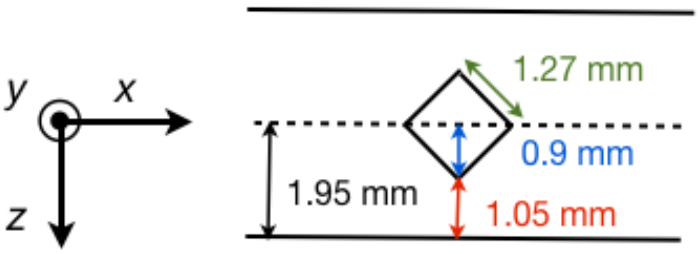

Fig. 4.7 Scale of the computational region near the diamond roughness.

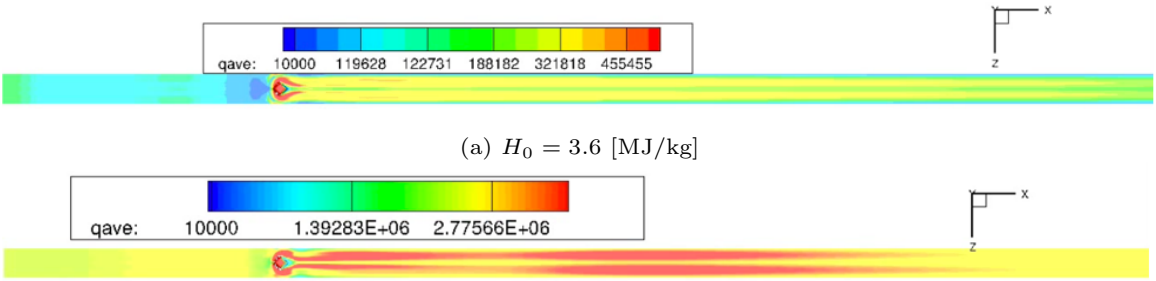

(a) $H_0 = 3.6$ [MJ/kg]

(b) $H_0 = 8.6$ [MJ/kg]

Fig. 4.8 Distribution of calculated time-averaged heat flux.

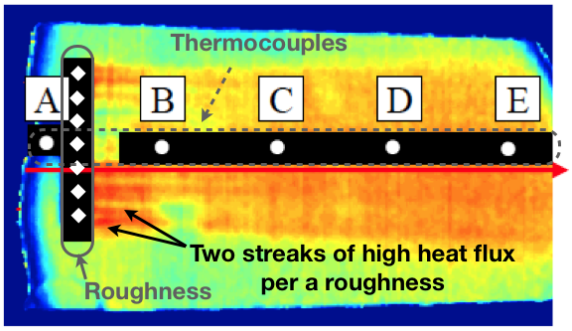

Fig. 4.9 TSP image on the back shell of HTV-R test model in the lower enthalpy condition.[1]

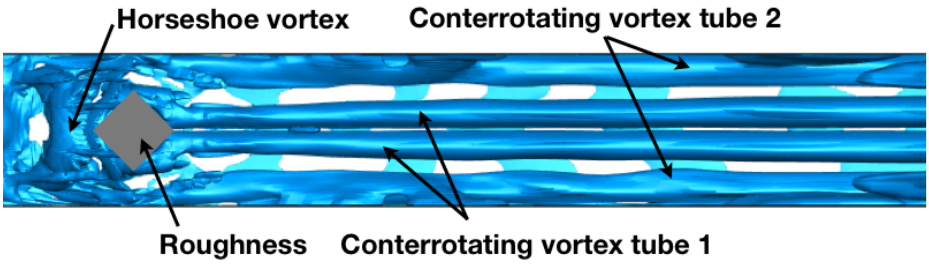

Fig. 4.10 Isosurface of Q-value in the lower enthalpy condition.

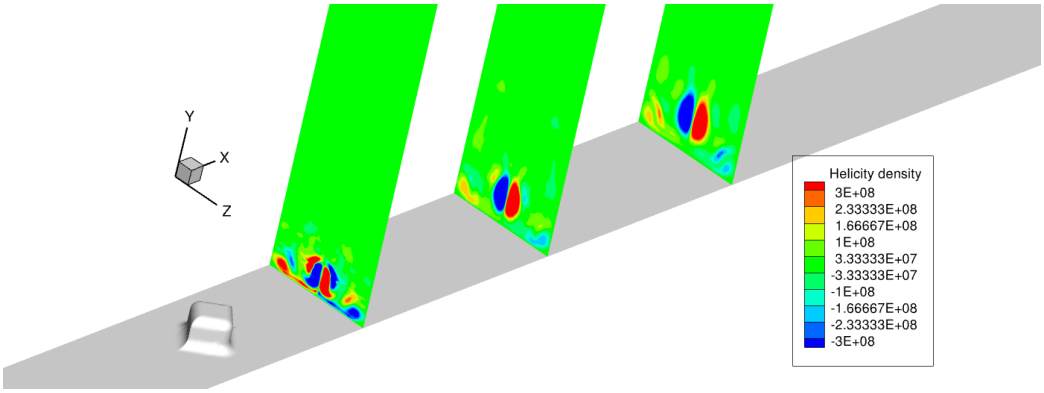

Fig. 4.11 Helicity density in x-direction on x-constant surfaces behind a roughness in the lower enthalpy condition: red and blue contours indicate clockwise eddy and anticlockwise eddy, respectively.

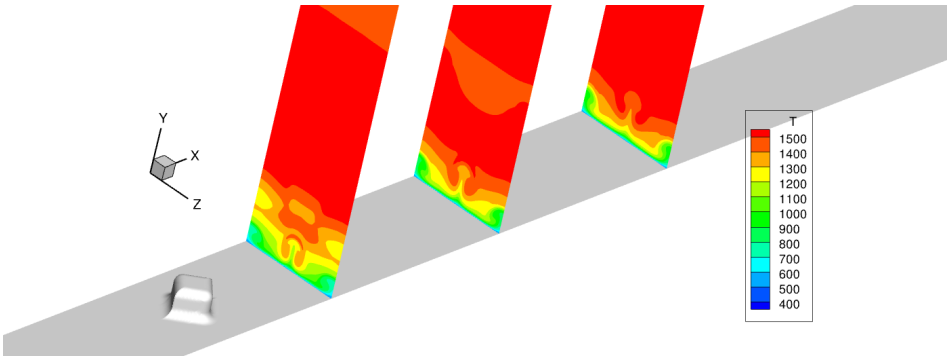

Fig. 4.12 Temperature distribution on x-constant surface behind a roughness in the lower enthalpy condition.

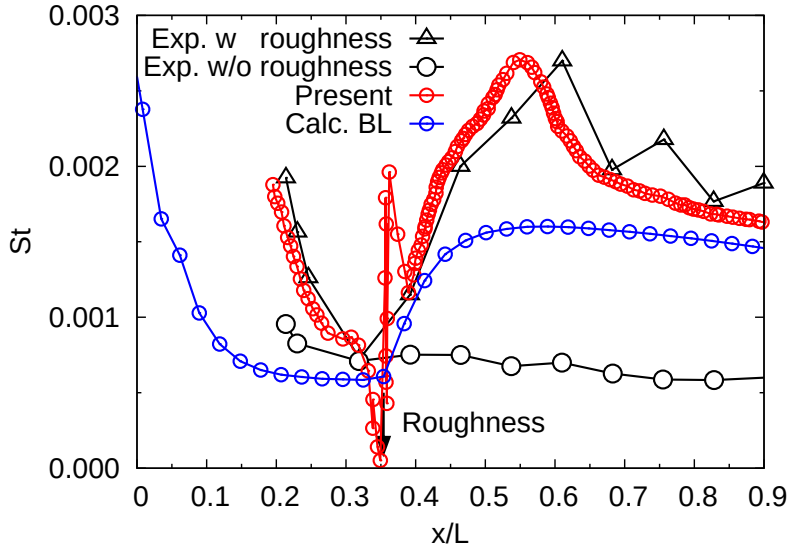

(a) $H_0 = 3.6$ [MJ/kg]

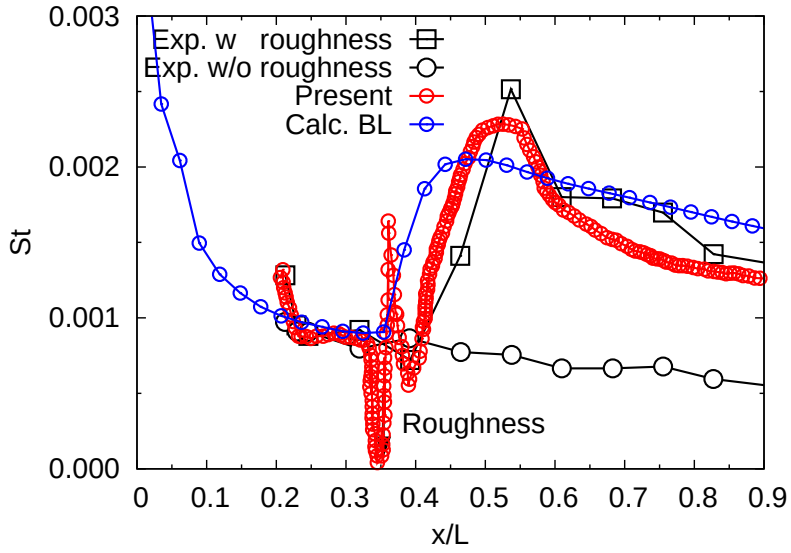

(b) $H_0 = 8.6$ [MJ/kg]

Fig. 4.13 Comparison of calculated time-averaged heat flux with measured data on the symmetry line.

Bibliography

[1] Nagai, H. and Horagir, T., "Visualization of a Re-entry Vehicle in Hypersonic Flow using Temperature -Sensitive Paint," Proceedings of the 16th International Symposium on Flow Visualization, ISFV16-1275, 2014.

[2] 丹野 英幸, 小室 智幸, 佐藤 和雄, 伊藤 勝宏, "高温衝撃風洞 HIEST による HTV-R カプセル形状模型の空力加熱試験," 日本機会学会 2014 年度年次大会, S191024, 2014.

[3] Park, C., *Nonequilibrium Hypersonic Aerothermodynaics*, John Wiley and Sons, Inc., 1989.

[4] Wang, Z. J. and Zhang, L. P., "A Block LU-SGS Implicit Dual Time-stepping Algorithm for Hybrid Dynamic Meshes," AIAA Paper 2003-3837, 2003.

[5] Jameson, A., "Time-dependent calculations using multi-grid with applications to unsteady flows past airfoils and wings," AIAA Paper 1991-1596, 1991.

[6] Eberhart, S. and Imalay, S., "Diagonal Implicit Scheme for Computing Flows with Finite Rate Chemistry," *Journal of Thermophysics and Heat Transfer*, Vol. 6, No. 3, 1992, pp. 208–216.

[7] Shima, E. and Kitamura, K., "Parameter-Free Simple Low-Dissipation AUSM-Family Scheme for All Speeds," *AIAA Journal*, Vol. 49, No. 8, 2011, pp. 1639–1709.

[8] Kitamura, K., Shima, E., Nakamura, Y., and Roe. P. L., "Evalution of Euler Fluxes for Hypersonic Heating Computations AUSM-Family Schemes for Hypersonic Heating Computations," *AIAA Journal*, Vol. 48, No. 4, 2010, pp. 763–776.

[9] Matsuyama, S.,, "Performance of all-speed AUSM-family schemes for DNS of low

Mach number turbulent channel flow," *Computers & Fluids*, Vol. 91, 2014.

[10] Thornber, B., Mosedale, A., Drikakis, D., Youngs, D., and Williamas, R. J. R., "An improved reconstruction method for compressible flows with low Mach number features," *Journal of Computational Physics*, Vol. 227, No. 10, 2008, pp. 4873–4894.

[11] Kim, J., Moin P., and Moser, R., "Turbulence statics in fully developed channel flow at low Reynolds number," *Journal of Fluid Mechanics*, Vol. 177, 1987.

[12] Taylor, E. M., Wu, M., and Martin P., "Optimization of nonlinear error for weighted essentially nonoscillatory methods in direct numerical simulations of compressible turbulence," *Journal of Computational Physics*, Vol. 223, No. 1, 2007, pp. 384–297.

[13] Kim, J., Moin P., and Moser, R., "Efficient implementation of weighted ENO schemes," *Journal of Computational Physics*, Vol. 126, No. 1, 1996, pp. 202–228.

[14] Liu, X. D., Osher, S., and Chan, T., "Weighted Essentially Non-Oscillatory Schemes," *Journal of Computational Physics*, Vol. 115, No. 1, 1994, pp. 200–212.

[15] Wu, M. and Martin P., "Direct numerical simulation of supersonic turbulent boundary layer over a compression ramp," *AIAA Journal*, Vol. 45, No. 4, 2007, pp. 879–889.

[16] Van Leer, B., "Towards the Ultimate Conservation Difference Scheme V. A Second-Order Sequel to Godunov's Method," *Journal of Computational Physics*, Vol. 23, No. 3, 1979, pp. 101–136.

[17] Takahashi, M., Kodera, M., Itoh, K., Komuro, T., Sato, K., and Tanno, H., "Influence of Thermal Non-equilibrium on Nozzle Flow Condition of High Enthalpy Shock Tunnel HIEST," AIAA Paper 2009-7267, 2009.

Chapter 5

Conclusions

In this dissertation, recently observed discrepancy of aerothermodynamic characteristics between CFD and experiments in HIEST were numerically explored toward realization of reliable aerothermodynamic prediction in high enthalpy conditions.

In Chapter 2, the abnormal heat flux augmentation observed in HIEST was numerically analyzed. The analysis revealed the following. (1) Radiation from impurities greatly contributed to heat flux augmentation. (2) The engineering technique to estimate the abnormal heat flux augmentation was obtained, though the test campaign for spectroscopy in the shock layer was required to clearly determine the source of the radiation. The abnormal heat flux augmentation could be estimated using $0.132\sigma T_{\mathrm{ave}}^4$ and the computed total heat flux profiles agreed fairly well with the experimental data. (3) The reason why the abnormal heat flux augmentation became significant in HIEST that the $q_{\mathrm{abnormal}}/q_{\mathrm{cal}}$ ratio became larger at large test model.

In Chapter 3, the cause of the observed overestimation of the computed wall pressure along the surface of the blunt-nosed test model under high enthalpy conditions of HIEST was explored. The present study revealed the followings: (1) When radiative cooling effect was included in the calculation of the flowfield in the nozzle region, the temperature at the nozzle exit was substantially decreased. The Pitot pressure profile at the nozzle exit agreed well with the experimental data if radiative cooling effect was accounted for. (2) The computed surface pressure distribution along the blunt test model agreed well with the measured in the experiment when the

upstream boundary condition was given by the computed result in the nozzle region in which radiative cooling effect was taken into account. (3) Neither the uncertainty in translational-vibrational relaxation time nor that in chemical reaction rates could explain the observed discrepancy in the surface pressure distribution. (4) The uncertainty in the chemical composition of the upstream boundary condition was not likely to be the cause of the discrepancy in the surface pressure distribution.

In Chapter 4, the discrepancy of heat flux on back shell of the HTV-R capsule with diamond roughness between RANS and experiments was examined using our developed high order code. It was shown that vortical flows of a certain scale behind the diamond shaped roughness substantially increased the surface heat flux. The time averaged heat flux behind the roughness agreed fairy well with the experimental data. It was found that the heating mechanism behind the roughness is due, not to turbulence but to the counter-rotating vortex tube.

In this study, we revealed the causes of recently observed discrepancy between CFD and experiments. Following knowledge was obtained. (1) To predict accurate heat flux on heat-shield in high enthalpy conditions of HIEST, the heat flux should be corrected by $0.132\sigma T_{v\mathrm{ave}}^4$ for large test model. (2) It is recommended to account for radiative cooling effect in computing the freestream condition of HIEST at high enthalpy conditions in order to predict the accurate aerodynamic characteristics. (3) The aerothermal measurements on back shell with the diamond roughness might be not enough accurate to predict fully turbulent heat flux. For safe design of TPS on back shell, more improved roughness which can generate more unsteady flow is needed. These knowledge can lead reliable aerothermodynamic predictions in high enthalpy conditions.

Acknowledgments

I would like to express my sincere gratitude to my adviser, Professor Keisuke Sawada. His guidance and encouragement throughout graduate course have been invaluable. He helped to improve my technical writing skills and oral presentation, which I greatly appreciate. He has also told me many things in the regular meeting in Kokubun-tyo. I have enjoyed the meeting very much.

I would like to thank Professor Keisuke Asai, Professor Shigeru Obayashi and Assosiate Professor Soshi Kawai for their suggestions and efforts as members of my dissertation reading committee. Professor Soshi Kawai gave me valuable comments in the seminar on progress report, which I greatly appreciate.

I would like to also express my sincere appreciation to Associate Professor Naofumi Ohnishi. His precious wisdom, experience and suggestion have greatly contributed to my Ph.D. work. I have enjoyed the discussion with him in the Ucyu-group seminar.

I also would like to thank Dr Hideyuki Tanno. His experience, suggestion and encouragement help me. His precious knowledge in hypersonic flow is quite helpful for my Ph.D. work.

I wish to offer my immeasurable gratitude to Assistant Professor Yousuke OGINO. He taught me not only fundamental numerical knowledge, writing and oral skills but also the altitude towards research. I have enjoyed the discussion with him in the Ucyu-grope. He always helped me during the most difficult times of my research life. I could not perform my Ph.D. work without him.

Throughout my graduate course, I have enjoyed my research life tanks to all seniors and juniors in my laboratory. I wish to say my many thanks especially to Mr.

Yoshihiro Toki, Ms. Reika Aizawa, Mr. Takumi Kino, Mr. Masaru Saijo, Mr. Yuji Matsuse, Mr. Kousuke Totani and Mr. Hiroaki Tatematsu in the Ucyu-group. The discussion with them is valuable for me.

Lastly, I would like to say thank to my family. They gave me both spiritual and financial support. I cannot find the words to express how thankful I am to them.